

A NUMERICAL ASSESSMENT OF DIRECT SHEAR BEHAVIOR IN CONCRETE

By

DAVID M. LAVENHAGEN

A THESIS PRESENTED TO THE GRADUATE SCHOOL  
OF THE UNIVERSITY OF FLORIDA IN PARTIAL FULFILLMENT  
OF THE REQUIREMENTS FOR THE DEGREE OF  
MASTER OF ENGINEERING

UNIVERSITY OF FLORIDA

2012

© 2012 David M. Lavenhagen

To my wife and parents, for, without which, this would not be possible

## ACKNOWLEDGMENTS

I would like to thank my advisor Professor Theodor Krauthammer for his guidance and encouragement throughout my research. I would also like to thank my committee member Dr. Serdar Astarlioglu for his insightful comments and suggestions for improving my work. Next I would like to thank Dr. Long Bui for his knowledge, time, and effort helping with the finite element modeling. Without the support of the sponsor, the Defense Threat Reduction Agency (DTRA), this research would not have been possible. I would also like to acknowledge my fellow colleagues at the Center for Infrastructure Protection and Physical Security (CIPPS), classmates and structures faculty at the University of Florida, and friends and family who have supported me through this process. Lastly, I would like to thank my wife who has stood by and believed in me throughout it all.

## TABLE OF CONTENTS

	<u>page</u>
ACKNOWLEDGMENTS.....	4
LIST OF TABLES.....	7
LIST OF FIGURES.....	8
ABSTRACT .....	12
CHAPTER	
1 INTRODUCTION .....	13
Problem Statement.....	13
Objective and Scope.....	14
Research Significance .....	14
2 LITERATURE REVIEW .....	15
Normal Strength Concrete .....	15
Compressive Strength and Behavior .....	15
Tensile Strength and Behavior .....	17
Ultra-High Performance Concrete.....	18
Definition of Ultra-High Performance Concrete .....	19
Ultra-High Performance Concrete Composition and Mixing Methodology .....	21
UHPC Mechanical Properties.....	23
UHPC stress-strain relationship .....	23
UHPC rate and size effect.....	25
Ultra-High Performance Concrete Manufacturers .....	25
Ductal <sup>®</sup> technology.....	26
CEMTEC <sub>multiscale</sub> .....	27
Cor-Tuf.....	27
Mild Steel Reinforcement.....	28
Modified Hsu Model for Steel Reinforcement .....	29
Park and Paulay Steel Model .....	29
Finite Element Method .....	31
Verification and Validation .....	33
Finite Element Code Abaqus.....	33
Concrete material models .....	34
CDP material model parameters.....	36
Reinforcement material models .....	37
Elements.....	37
Direct Shear Behavior.....	38
Experimental Work .....	40
Hofbeck et al. (1969) and Mattock and Hawkins (1972) .....	40

Walraven and Reinhardt (1981).....	43
Valle and Buyukozturk (1993).....	45
Numerical Models.....	48
Original and modified Hawkins shear models .....	48
Modified shear transfer model.....	50
Summary .....	55
3 RESEARCH APPROACH AND METHODS .....	83
Model Validation .....	83
Specimen Geometry and Materials .....	84
Test Setup.....	85
Results .....	85
Failure Modes.....	86
Evolution of the FE model.....	87
Defining the FE model .....	88
Material Models .....	88
Concrete material model.....	88
Steel material model .....	89
Elements .....	89
Rebar Embedment .....	90
Element Dimensions .....	90
Analysis Type .....	91
Boundary Conditions .....	91
Summary .....	91
4 RESULTS AND DISCUSSION .....	104
Loading Cases.....	104
Recording Vertical Displacement.....	104
Simulation Results .....	106
NC Results .....	106
NCS Results.....	107
Hawkins Shear Model.....	108
Summary .....	108
5 CONCLUSIONS AND RECOMMENDATIONS.....	120
Conclusions .....	120
Recommendations for Future Research .....	120
LIST OF REFERENCES .....	122
BIOGRAPHICAL SKETCH.....	126

## LIST OF TABLES

<u>Table</u>		<u>Page</u>
2-1	Quasi-static uniaxial compressive performance of UHPCC at 60 days .....	78
2-2	Compressive strength of 3 in x 6 in UHPC cylinders .....	78
2-3	Formulation of Ductal <sup>®</sup> .....	79
2-4	Formulation of CEMTEC <sub>multiscale</sub> (kg/m <sup>3</sup> ) .....	79
2-5	Cor-Tuf mixture composition.....	80
2-6	Unconfined compressive strengths for Cor-Tuf cylinders .....	80
2-7	Test specimen classification by type of concrete and shear reinforcement .....	80
2-8	Results for normal strength concrete specimens.....	81
2-9	Results for high-strength concrete specimens.....	82
2-10	Peak and ultimate strains used for different types of concrete .....	82
3-1	Concrete mix proportions by weight .....	103
3-2	Valle test results for NC and NCS push-off specimens .....	103
3-3	CDP material model parameters .....	103
4-1	Comparison of results for NC specimens .....	118
4-2	Comparison of results for NCS specimen.....	119

## LIST OF FIGURES

<u>Figure</u>	<u>Page</u>
2-1 Typical concrete stress-strain curves in compression .....	56
2-2 Modified Hognestad curve for concrete in compression .....	56
2-3 Tensile stress-strain curve of concrete .....	57
2-4 Component volume percentages in HPC, SCC, UHPC and RPC .....	57
2-5 Increasing brittleness with strength .....	58
2-6 Crack pattern in reinforced concrete and fiber reinforced concrete elements subjected to tension.....	58
2-7 Bekaert Dramix® ZP305 fibers used in Cor-Tuf .....	59
2-8 Example of optimum mix proportion of UHPC .....	59
2-9 Mechanical properties of conventional concrete and UHPFRC .....	59
2-10 Compressive stress-strain diagram of UHPC without fibers .....	60
2-11 UHPFRC stress-crack opening curve.....	60
2-12 Effect of fibers on UHPFRC descending compressive stress-strain curve .....	60
2-13 Shear specimen dimensions (in mm) .....	61
2-14 Dynamic increase factor versus peak loading rate for shear tests.....	61
2-15 Ductal® behavior in compression and bending .....	62
2-16 Bi-linear stress-strain curve for embedded reinforcement .....	62
2-17 Modified Hsu model for steel reinforcement .....	62
2-18 Uniaxial compressive stress-strain behavior for CDP material model .....	63
2-19 Park and Paulay strain-hardening model.....	63
2-21 Uniaxial compressive stress-strain behavior for CDP material model .....	64
2-22 Uniaxial tensile stress-strain-curve in CDP material model .....	65
2-23 Drucker-Prager plastic flow potential .....	65

2-24	8-node brick element .....	66
2-25	Full integration and reduced integration 8-node brick elements .....	66
2-26	2-node beam element.....	66
2-27	Direct shear failure in RC box top slab (side view) .....	67
2-28	Displacement along a cracked shear plane.....	67
2-29	Shear transfer test specimens .....	68
2-30	Push-off specimen details .....	68
2-31	Typical load-slip curves .....	69
2-32	Effect of concrete strength on shear strength of initially cracked specimens.....	69
2-33	Shear transfer in initially uncracked concrete .....	70
2-34	Structure of a crack plane.....	70
2-35	Push-off specimen geometry (in mm).....	70
2-36	Stirrups and additional reinforcement .....	71
2-37	Maximum shear stresses as a function of concrete compressive strengths, $f_{cc}$ , and mechanical reinforcement ratio, $\rho f_{sy}$ .....	71
2-38	Crack opening under a certain shear stress, $\tau$ , as a function of the reinforcement ratio, $\rho$ .....	72
2-39	Average crack opening paths .....	72
2-40	Shear stress-shear displacement at various angles of inclination, $\theta$ .....	73
2-41	Crack opening for smooth and deformed bars.....	73
2-42	Expected additional cracking for shear loading with deformed bars .....	73
2-43	Push-off specimen geometry (1 in. = 25.4 mm).....	74
2-44	Cracking patterns for push-off specimens .....	75
2-45	Shear stress versus shear strain for SHC .....	75
2-46	Original and modified shear stress-slip relationship for direct shear .....	76
2-47	Shear transfer problem.....	76

2-48	Before cracking shear stress distribution and shear strain distribution .....	77
2-49	Idealized stress-strain curve for concrete in compression .....	77
2-50	Idealized tension stress-strain curve for plain concrete and steel fiber reinforced concrete .....	78
3-1	Push-off specimen geometry .....	92
3-2	Push-off specimen reinforcement detail .....	93
3-3	LVDT placement and loading configuration .....	94
3-4	Loading configuration .....	95
3-5	Normalized shear stress vs. vertical displacement for NC .....	96
3-6	Normalized shear stress vs. horizontal displacement for NC .....	96
3-7	Normalized shear stress vs. vertical displacement for NCS .....	97
3-8	Normalized shear stress vs. horizontal displacement for NCS .....	97
3-9	Cracking patterns for push-off specimens .....	98
3-10	NC specimen after failure .....	98
3-11	NCS specimen after failure .....	99
3-12	NC compressive stress-strain relationship .....	99
3-13	NC tensile stress-strain relationship .....	100
3-14	NCS compressive stress-strain relationship .....	100
3-15	NCS tensile stress-strain relationship .....	101
3-16	Mild steel stress-strain behavior for 60 ksi deformed bars .....	101
3-17	Mesh Density .....	102
3-18	Reinforcement in the model .....	102
4-1	Boundary conditions .....	109
4-2	LVDT setup for the experimental testing .....	110
4-3	Type 1 node set .....	110
4-4	Type 2 node set .....	111

4-5	Type 3 node set.....	111
4-6	LVDT 1 node set.....	112
4-7	LVDT 2 node set.....	112
4-8	NC with load case 1.....	113
4-9	NC with load case 2.....	113
4-10	NC with load case 3.....	114
4-11	Maximum principal strains at integration points at failure .....	115
4-12	NCS with load case 1 .....	116
4-13	NCS with load case 2 .....	116
4-14	NCS with load case 3 .....	117
4-15	Normalized shear stress vs. vertical displacement.....	117
4-16	Normalized shear stress vs. vertical displacement.....	118

Abstract of Thesis Presented to the Graduate School  
of the University of Florida in Partial Fulfillment of the  
Requirements for the Degree of Master of Engineering

A NUMERICAL ASSESSMENT OF DIRECT SHEAR BEHAVIOR IN CONCRETE

By

David M. Lavenhagen

August 2012

Chair: Theodor Krauthammer  
Major: Civil Engineering

The direct shear behavior of ultra-high performance concrete, specifically Cor-Tuf, is currently unknown. Furthermore, capturing the direct shear response of conventional concrete numerically using the finite element method has not been investigated in the literature. Push-off specimens, commonly used to study direct shear, will be modeled using the explicit finite element code Abaqus. It is unknown whether the current material models for concrete in Abaqus can accurately predict the shear stress – shear slip relationship in push-off specimens. This study aims to validate the use of the finite element method to capture the shear transfer strength of push-off specimens. This will be accomplished by comparing the numerical results to experimental test data. Furthermore, the Hawkins shear transfer model will be used to investigate its appropriateness to predicating the shear stress- shear slip relationship of push-off specimens. Once, confidence in capturing this behavior is conventional concrete is accomplished, pre-test predictions for future testing can be made as well as implementing material models that describe ultra-high performance concrete.

## CHAPTER 1 INTRODUCTION

### **Problem Statement**

Direct shear failure is a sudden and catastrophic type of failure commonly observed in reinforced concrete structures under highly impulsive dynamic loads. It is classified as a sliding type failure along a well-defined plane where slip occurs at a location where either the load or the geometry is discontinuous in a direction perpendicular to the axis of the member. Direct shear failure can severely compromise the integrity of the structure and possibly cause progressive collapse.

While the direct shear response of beams, columns, and boxes constructed using normal strength concrete (NSC) has been studied both experimentally and analytically by many researchers, there is very little or no reported data on direct shear response of structural members constructed using Ultra High Performance Concrete (UHPC). Furthermore, it is not known whether direct shear in UHPC can be treated just like NSC, but with a very high compressive strength. This problem is most unique in both the structural dynamics and material aspects, and its implications of protecting critical facilities could be very important.

Furthermore, numerical assessment of direct shear behavior of push-off specimens, specific specimens used to study shear transfer and direct shear, has not been attempted thus far in the research community. It is unknown whether current finite element codes can accurately capture this type of behavior/failure. Current research includes experimental studies on push-off specimens but numerical studies are lacking.

## **Objective and Scope**

The primary objective of this research is to accurately predict the direct shear response of push-off specimens numerically through the use of the finite element method (FEM). The secondary objective is to assess the current mathematical models for predicting the shear stress-shear slip behavior of push-off type specimens. This will be accomplished by utilizing both numerical methods as well as employing the Hawkins shear model.

The scope will include a literature review of the relevant topics related to this research and a numerical study using the FE software package, ABAQUS/Explicit. This numerical study will be followed by an experimental study and an additional numerical analysis needed to thoroughly investigate the behavior of normal strength concrete and the UHPFRC, Cor-Tuf, subjected to direct shear.

## **Research Significance**

Direct shear is a sudden and brittle type of failure. The advancement of the state of knowledge in this area can possibly lead to a better design of structures that are less susceptible to direct shear failures. The study will provide a numerical assessment of the current ability of the FE code, Abaqus/Explicit, to accurately represent the shear transfer of push-off specimens. If successful, this model can be used for predicting the ultimate shear strength as well as shear slip that can be expected during a specific type of loading.

This study is crucial in determining the ability of the FEM to accurately model the behavior of push-off specimens. Once this is accomplished using conventional concrete, the model can be used to study and to give predictions on the ultimate shear strength and shear slip of push-off specimens with varied parameters.

## CHAPTER 2 LITERATURE REVIEW

The literature review provides a comprehensive background of the pertinent information related to the research. The first section will briefly describe the properties of normal strength concrete. The next section will discuss the definition, composition, products and applications of UHPC. The following section will discuss the properties of steel reinforcing bars. The finite element method will then be discussed and finally the phenomenon known as direct shear and shear transfer behavior in concrete will be reviewed.

### **Normal Strength Concrete**

Concrete is a composite material composed of aggregate (sand and gravel), portland cement, and water. The aggregate is usually graded in size from sand to gravel and in structural concrete the maximum aggregate size is most commonly  $\frac{3}{4}$  in. but can be larger or smaller depending on the application.

### **Compressive Strength and Behavior**

Concrete is mainly a compression material. While concrete is made from elastic, brittle materials, its stress-strain curve under compression is somewhat ductile. This behavior can be described by microcracking in the material that redistributes the stresses from element to element. As concrete strength increases, the slope of the descending branch of the compressive stress-strain curve increases. This behavior is illustrated in Figure 2-1. For concrete strengths up to 6,000 psi, the slope of the descending branch tends to be less than the ascending branch. Once the concrete strength reaches 10,000 psi, the slope of the descending branch is nearly vertical. This behavior can be explained by major longitudinal cracking of the concrete structure. It

can also be seen for the stress-strain relationship that the maximum concrete strain decreases with increasing strength.

A commonly used model to represent stress-strain curve for concrete in compression is the modified Hognestad curve shown in Figure 2-2. The model is valid for concrete strengths up to 6,000 psi and assumes the concrete section is unconfined and uniaxially loaded in compression. The curve consists of a second-degree parabola up to a strain of  $1.8f_c''/E_c$ , where  $f_c'' = 0.9 f_c'$ , followed by a linear descending branch with a limiting strain of 0.0038 which is the assumed concrete crushing strain.

Below is the ascending branch of the curve.

$$f_c = f_c'' \left[ \frac{2\varepsilon_c}{\varepsilon_o} - \left( \frac{\varepsilon_c}{\varepsilon_o} \right)^2 \right] \quad \text{for } \varepsilon_c \leq \varepsilon_o \quad (2-1)$$

Below is the descending branch of the curve.

$$f_c = f_c'' - E_{cd}(\varepsilon_c - \varepsilon_o) \quad \text{for } 0.0038 > \varepsilon_c > \varepsilon_o \quad (2-2)$$

where,

$f_c$  is the concrete compressive strength,

$$f_c'' = 0.9f_c' \quad (2-3)$$

$f_c'$  is the uniaxial compressive strength of a standard cylinder test and

$\varepsilon_c$  is the concrete strain

$$\varepsilon_o = \frac{1.8f_c''}{E_c} \quad \text{is the strain at the maximum concrete stress} \quad (2-4)$$

The modulus of elasticity of normal-weight concrete,  $E_c$ , is given by ACI 318-08 Code Section 8.5.1 as.

$$E_c = 57,000\sqrt{f'_c} \text{ psi} \quad (2-5)$$

.ACI Committee 363 proposed the following equation for high-strength concretes.

In particular, this relationship was developed for concretes up to 12 ksi (83 MPa).

$$E_c = 40,000\sqrt{f'_c} + 1.0 \times 10^6 \text{ psi} \quad (2-6)$$

### **Tensile Strength and Behavior**

Tensile strength is very difficult to capture experimentally. In general, tensile strength is approximated as 10% of its compressive strength though this value is dependent on the type of tensile test, the compressive strength of the concrete and the presence of compressive stress transverse to the tensile stress (Wight and MacGregor 2008). There are two commonly used tests to determine tensile strength; the split cylinder test (ASTM C496) and the modulus of rupture or flexural test (ASTM C78 or C293).

ACI 318-08 Code Section 9.5.2.3 defines the modulus of rupture for use in calculating deflections for normal-weight concrete as.

$$f_r = 7.5\sqrt{f'_c} \cdot \text{psi} \quad (2-7)$$

where  $f'_c$  is in psi. Other accepted values in the literature for tensile strength are between  $3 - 5\sqrt{f'_c} \cdot \text{psi}$ .

The stress-strain behavior of concrete in tension is linear until first cracking occurs then significantly drops and follows a concave up parabola until failure. This behavior is shown in Figure 2-3. There has been multiple stress-strain models proposed for concrete in tension in the literature. These can be found in Vecchio and Collins (1981),

Mitchell and Collins (1991) and Hsu (1993). Hsu's proposed model is described below in detail.

Below is the ascending branch of the curve.

$$\sigma_r = E_c \varepsilon_r \quad \text{for} \quad \varepsilon_r \leq \varepsilon_{cr} \quad (2-8)$$

where,

$$E_c = 47,000 \sqrt{f'_c} \cdot psi \quad (2-9)$$

$$\varepsilon_{cr} = 0.00008 \text{ in./in.}$$

Below is the descending branch of the curve.

$$\sigma_r = f_{cr} \left( \frac{\varepsilon_{cr}}{\varepsilon_r} \right)^{0.4} \quad \text{for} \quad \varepsilon_r > \varepsilon_{cr} \quad (2-10)$$

$$f_{cr} = 3.75 \sqrt{f'_c} \cdot psi \quad (2-11)$$

where,

$f'_c$  is the uniaxial concrete compressive strength in psi

$f_{cr}$  is the cracking stress of plain concrete in psi and

$\varepsilon_{cr}$  is the cracking strain

### **Ultra-High Performance Concrete**

Ultra high performance concrete (UHPC) has been the topic of much research in the last few decades. Researchers continue to study the material and generate the necessary information to maximize its usefulness in structural applications. UHPC is commonly characterized by increased strength, durability and ductility (Astarlioglu et al. 2010). In this section of the literature review, you will find a comprehensive background of the development and material characterization of UHPC followed by a brief overview of the current products developed as UHPC. Further, you will find a brief discussion on its applications in the field of protective structures.

## **Definition of Ultra-High Performance Concrete**

As stated previously, there is no global definition of UHPC but there are general properties associated with it. The Association Française de Génie Civil (AFGC) classifies UHPC as having a compressive strength greater than 150 MPa (22 ksi), internal fiber reinforcement to ensure non-brittle behavior, and a high binder content with special aggregates (Association Française de Génie Civil 2002). The US Army Engineering Research and Development Center (ERDC) classify UHPC as cementitious materials with unconfined compressive strengths ranging from 138 to 276 MPa (20 to 40 ksi) (Roth et al. 2008).

UHPC is commonly known for its relatively high unconfined compressive strength. Generally, this is achieved by densification of the concrete matrix and careful selection of its constituent materials along with reducing the water to cement ratio significantly. In comparison, typical compressive strengths of normal strength concrete are less than 41 MPa (6 ksi) and high strength concrete ranges from 41 to 138 MPa (6 ksi to 20 ksi). UHPC also displays hardening in tension due to the matrix of fibers included in the mix. This is an integral part of UHPC and one that NSC does not share. The Federal Highway Administration's definition includes eight performance characteristics. freeze-thaw durability, scaling resistance, abrasion resistance, chloride penetration, compressive strength, modulus of elasticity, shrinkage, and creep.

In addition to its high compressive strength, UHPC is characterized by high durability. Both of these qualities are attributed to the low porosity which is a result of the dense packing of its constituent materials at the micro-level. The microstructure of one commercially developed UHPC, Ductal<sup>®</sup>, is completely closed which prevents any aggressive agents from penetrating (Acker and Behloul 2004). The result of the dense

packing of constitutive materials is a relatively low water-to-cement ratio, typically close to 0.20, compared with a w/c ratio of 0.30-0.45 for NSC. Higher amounts of superplasticizers are required to ensure adequate workability in the mix and also to allow fibers into the mix. For comparison, Figure 2-4 shows the compositions of high-performance concrete (HPC), self-compacting concrete (SCC), UHPC and reactive powder concretes (RPC).

While the compressive strength of UHPC is increased dramatically by its mix components, the brittleness increases as well. UHPC remains mainly a compression only material but the tensile strength is higher than NSC and HSC. The disadvantage of concrete is its low tensile strength in comparison to compressive strength and the brittle failure behavior in tension. Historically, steel reinforcing bars are used to carry the tensile forces in a section. As mentioned previously, UHPC relies on fibers, most commonly steel, to bridge the micro-cracks developed by tensile stresses. The fibers dramatically improve the tensile strength and produce a gradual softening behavior after the peak tensile strength is reached. This is the primary contributor to the tensile behavior of UHPC.

Figure 2-5 shows a comparison between NSC, HSC and UHPC compressive stress versus strain diagrams. While the NSC curve starts to soften and level out, showing some ductility before failure, UHPC shows a prompt decrease in capacity after the peak stress is reached. This behavior produces unpredictable and very rapid failure. Adding fibers to the mix greatly increases the tensile capacity and more importantly increases the ductility of the concrete. The fibers create a homogenous matrix in the mix and control local crack opening and propagation (Brandt 2008). Instead of large cracks

forming as per NSC, a network of micro-cracks forms and the fibers bridge the gaps of the micro-cracks as illustrated in Figure 2-6.

### **Ultra-High Performance Concrete Composition and Mixing Methodology**

UHPC can be characterized as a reactive powder concrete (RPC). RPCs do not include coarse aggregates typically found in conventional concrete but use fine aggregates and pozzolanic powders to achieve a densely packed mixture. The main constituents of UHPC are cement, sand, silica fume, superplasticizer, water and fibers. Below you will find a short description of these constituents most commonly used in UHPC mix design. Further, the mixing and curing methodology currently employed is reviewed.

**Cement.** The high strength compressive strength as well as the ductility and durability are attributed to the very low water-to-cement (w/c) ratios present in UHPC. The w/c ratio of UHPC typically ranges from 0.17 - 0.21. This is very low when compared to conventional concrete w/c ratios of 0.30 – 0.45. There is general agreement in the literature that the cement should have a low alkali and tricalcium aluminate (C3A) content (Richard and Cheyrezy 1995).

**Sand.** Quartz sand is typically used as the aggregate in UHPC with the mean particle size often being less than 1 mm although mixes with much higher particle sizes, between 8 and 16 mm, have been produced (Habel 2004).

**Superplasticizer.** Superplasticizers are used for two main reasons in UHPC; to increase the workability of the fresh concrete for placing without disturbing the mix composition and to reduce the w/c ratio in order to increase the strength and improve durability at a given workability (Colleparidi 1998). The most common type of superplasticizers used are based on polycaroxyletes which can reduce the water

requirement by up to 40% while maintaining flowability (Hirschi and Wombacher 2008; Lallemand-Gamboa et al. 2005).

**Fibers.** Metallic or synthetic fibers are used in UHPC mixes to increase the ductility of the otherwise brittle cementitious matrix. The fibers are randomly distributed and orientated in the cementitious matrix during mixing. The effect of percent volume of fibers in the mix has been investigated by (Rong et al. 2010). Three volume percentages of 0%, 3% and 4% fiber content were selected to study the mechanical properties of UHPC. Table 2-1 shows the results of quasi-static uniaxial compression tests performed on the three fiber contents. The compressive strength, peak value of strain and the toughness index of the specimens all increase with an increase of fiber content. Although these attributes increase with an increase in fiber content, a limit of roughly 5% by volume of fibers is the upper limit due to workability issues.

Figure 2-7 shows steel fibers used in Cor-Tuf1, a UHPC developed by the U.S. Army Engineer Research Development Center (ERDC). The fibers are approximately 30 mm long with a diameter of approximately 0.55 mm and have hooks at each end to help development. The tensile strength as reported by the manufacturer is 1,100 MPa (Williams et al. 2009).

The procedure for preparing UHPC specimens are outlined below and are typical of most UHPC. First, the dry constituents, cement, sand, and silica fume and/or silica flour, are weighed and dry-blended together in a mixer for 2-5 minutes. Water and superplasticizer are mixed together and gradually added to the dry mix allowing it to become a wetted, flowable paste, 5-15 minutes. Steel fibers are then added to the mixer and allowed to mix for 3-10 minutes. Casting is recommended to be done within 20

minutes of mix completion and most commonly is done on a vibrating table or accomplished with vibrating rods (Graybeal 2005; Williams et al. 2009).

While an optimum mixture of UHPC depends highly on the intended application, desired properties and cost, Park et al. (2008) generated an optimized mix proportion for 180 MPa UHPC by studying each ingredient and its influence on compressive strength. His recommendations are shown in Figure 2-8.

The curing procedure can be quite drastic and intensive and varies considerably depending on the manufacturer. Williams et al. (2009) proposed the curing procedure for Cor-Tuf as placing the fresh specimens at 22°C and 100% humidity for 7 days, being demolded after 24 hrs. Then the specimens are submerged in a water bath at 85°C for 4 days. Finally, specimens were oven dried at 85°C for 2 days leading to a total time of 13 days. Lafarge recommends its commercially available mix marketed under the name Ductal® to be steam treated at 90°C and 95% relative humidity for 48 hours directly after demolding (Graybeal 2005). Others have investigated a less intensive curing regime with results of lower compressive strength.

Table 2-2 shows results from Sayed (2004) of four different curing methods. steam, ambient air, tempered steam, and delayed steam. The difference in compressive strength between the steam cured and ambient air cured specimens is considerable.

### **UHPC Mechanical Properties**

In this section, the stress-strain relationship of UHPC is discussed followed by a discussion of the rate and size effect.

#### **UHPC stress-strain relationship**

As previously stated, the most significant benefits of UHPC are its high compressive and tensile strengths when compared to normal strength concrete.

Another important feature of UHPC is the added ductility of the material post-peak stress is reached. This ductility plateau is made possible by the matrix of fibers slowly yielding. The compressive and tensile stress-strain curves along with the demonstration of the added ductility are shown in Figure 2-9 which compares UHPFRC to NSC. Another observation is the gradual softening of the tensile stress-strain curve for UHPFRC compared to the rather abrupt decrease in stress post-peak of the NSC.

The elastic region of the stress-strain curve for UHPC and UHPFRC are very similar. In contrast to UHPFRC, UHPC without fibers has no post-peak capacity and fails in an explosive manner. This is represented in Figure 2-10.

The descending branch of the stress-strain curve for UHPFRC depends on the variables related to the fibers present such as the fiber content, geometry, length in regards to the maximum aggregate size and orientation. The effect of fiber orientation has been explored by Fehling et al. (2004). The influence of the fibers has a more dramatic effect on the tensile behavior of the concrete as illustrated in Figure 2-11 where tensile stress is plotted against crack opening. Of interest is the dramatic difference in the descending slope depending on fiber content, type and orientation.

Fiber orientation and volume determine the descending branch for compression also but with less pronounced differences. Typically, a 10-15% gain in compressive strength can be achieved by the addition of fibers. Like the tensile stress-strain relationship, the descending branch can vary depending on fiber content and orientation as depicted in Figure 2-12.

Fehling et al. (2004) studied the fiber direction by casting specimens vertically and horizontally. The results indicated a significant difference for specimens subjected to 3-

point bending tests. They calculated that the tensile capacity under static loading is reduced between 33% and 20% if the flow direction used during casting is vertical.

### **UHPC rate and size effect**

As with normal strength concrete, UHPC has a definite increase in strength from the application of a dynamic load such as blast or impact. Smaller specimens tend to have increased strength as well when compared to similar specimens of larger dimensions. Millard et al. (2010) has concluded through testing that the enhancement of shear strength, known as the dynamic increase factor, DIF, in push-off specimens is fairly insignificant for strain rates less than  $10 \text{ s}^{-1}$ . Dynamic shear testing was done using a drop hammer and push-off specimens with geometry shown in Figure 2-13. The push-off specimens used are very small when compared to other direct shear tests in the literature. Hopkinson bar tests are required to determine the dynamic increase factor for strain rates higher than those tested. Figure 2-14 shows the results of the dynamic shear tests performed.

This small increase in the DIF is verified by the design provisions set forth by the US Army design guide *Structures to Resist the Effects of Accidental Explosions*, where it is suggested to use only a 10% increase for shear strength as opposed to 25% for flexural strength

### **Ultra-High Performance Concrete Manufacturers**

UHPC has seen many proprietary mixes developed for specific application but only a few are commercially available. The most common two are Ductal<sup>®</sup> technology developed by three companies; Lafarge, Bouygues and Rhodia, all based in France and CEMTEC<sub>multiscale</sub> developed by The Laboratoire Central des Ponts et Chaussées (LCPC) also in France. Another proprietary mix that is not commercially available is

Cor-Tuf developed by the US Army. These mixes and their properties are briefly described below.

### **Ductal<sup>®</sup> technology**

Ductal<sup>®</sup> is an ultra-high performance fiber reinforced concrete developed over a decade by three companies; Lafarge, Bouygues and Rhodia, all based in France. The Ductal<sup>®</sup> technology includes a range of formulations that can be adjusted to produce different properties based on the structural demand of the customer. The main idea behind the development of Ductal was to create a very dense mixture to avoid voids in the concrete. This is accomplished by optimizing the mix to include very small particle sizes ranging from 600  $\mu\text{m}$  down to less than 0.1  $\mu\text{m}$ . This allows the granular mixture to be highly homogeneous and compacted. Fibers are included to improve the tensile strength and provide adequate ductility. Table 2-3 shows a typical composition. Ductal formulations include steel (Ductal<sup>®</sup>-FM), organic (Ductal<sup>®</sup>-FO) or steel and organic fibers (Ductal<sup>®</sup> AF) included in the mix. Most structural applications use Ductal<sup>®</sup>-FM while Ductal<sup>®</sup> AF is suited more towards architectural applications (Acker and Behloul 2004).

There were more than 15 universities and 6 testing laboratories involved in a comprehensive analysis of the mechanical properties. The data generated from these tests were used to define the mechanical behavior. Compressive and flexural behavior of Ductal<sup>®</sup>-FM compared to normal strength concrete is shown below in Figure 2-15. The difference in ultimate capacity in both behaviors is dramatically increased as is the ductility once the ultimate load is reached. According to Lafarge this can allow the omission of secondary and shear reinforcement. The steel fibers used had a tensile strength of 200 MPa and a Young's modulus of 200 GPa. They compose of 2% by

volume of the mix and are 13-15 mm in length with an average diameter of 0.2 mm.

These dimensions were found to give the best results out of thousands of tests (Acker and Behloul 2004).

### **CEMTEC<sub>multiscale</sub>**

CEMTEC<sub>multiscale</sub>, developed by The Laboratoire Central des Ponts et Chaussées (LCPC) in France, has a unique formulation. It is a UHPFRC with three different geometry fibers included in the mix and contains 11% per volume of fibers. This is an unusually large percent of fibers per volume. The three different sizes of fibers, short, medium, long, allow the fibers to perform at the micro and macro scale to increase the tensile strength, ductility and bearing capacity (Rossi et al. 2005). According to Rossi et al., CEMTEC<sub>multiscale</sub> has a compressive strength equal to 205 MPa and ultimate strain equal to 0.004. The ultimate tensile strain is reported as 0.005 with a Young's modulus equal to 55 GPa. Table 2-4 shows the formulation of CEMTEC<sub>multiscale</sub>.

### **Cor-Tuf**

Cor-Tuf was developed by the U.S. Army Engineering Research and Development Center (ERDC) located in Vicksburg, MS. ERDC sought a way to incorporate local materials to reduce production costs associated with specific materials used in other specialized mixes while maintaining workability and ultra-high compressive strengths (Williams et al. 2009). Six mechanical property tests were performed by the Geotechnical and Structures Laboratory (GSL) that included hydrostatic compression, unconfined compression, triaxial compression, unconfined direct pull, uniaxial strain, and uniaxial strain/constant volume strain tests.

The findings were compiled by Williams et al. in a report entitled *Laboratory Characterization of Cor-Tuf Concrete With and Without Steel Fibers*. As the title states two mixes were developed, Cor-Tuf1 includes steel fibers while Cor-Tuf2 does not. The mixture composition shown in Table 2-5 was used for testing. The w/c ratio is limited to roughly 0.21 and the percent of fibers by volume for Cor-Tuf1 is 3.6%. The steel fibers used have previously been discussed in the section *Fibers* above.

The Cor-Tuf cylinder specimens produced in the report had an unconfined compressive strength ranging from 190 to 244 MPa as shown in Table 2-6. The average compressive strengths for Cor-Tuf1, Cor-Tuf1 without fibers and Cor-Tuf2 are approximately 237, 210, and 214 MPa. The fibers appear to increase the unconfined compressive strengths by roughly 10%.

### **Mild Steel Reinforcement**

Because concrete is weak in tension, steel reinforcing bars are used to resist the tensile stresses induced in a section. Steel reinforcing bars are essentially round in cross section with lugs created to enhance anchoring capacity in concrete. Bars are produced according to ASTM standards with ASTM A 615 and ASTM A706 bars most commonly used. Bars are available in four grades referencing their yield strengths of 40, 50, 60 and 75 ksi. Grade 60 is the most common in buildings and bridges and is also the most commonly available. Sizes are expressed in nominal diameters of a 1/8 in. For example, a No. 5 bar has a nominal diameter of 5/8 in.

The stress-strain curve of mild steel is generally assumed to be elastic-perfectly plastic. This idealized relationship holds true for bare bars but changes once the reinforcement is embedded in concrete. Once cracking occurs in a section and the reinforcement bridges the cracks, the stress distribution is altered in both the concrete

and the steel. This changes the stress-strain curve of the concrete stiffened bar. Hsu (1993) noticed this difference and proposed a bi-linear stress-strain curve for imbedded reinforcing bars. His model is shown by the dashed line in Figure 2-16.

The maximum strain allowed in the model is 0.05. For higher strains, Koh (2011) has proposed to modify Hsu's model by introducing a cap in the strain. The next section summarizes a modified steel model base on Hsu's work.

### Modified Hsu Model for Steel Reinforcement

Presented below is the Modified Hsu Model for Steel Reinforcement as proposed by Koh (2011).

$$f_s = E_s \varepsilon_s \quad \text{for} \quad f_s \leq f_y' \quad (2-12)$$

$$f_s = f_y' = \left(1 - \frac{2 - \alpha/45}{1000\rho}\right) \left(0.43 + 0.5 \frac{f_y^*}{f_y}\right) f_y \quad \text{for} \quad f_s \geq f_y' \quad (2-13)$$

$$E_p' = \left(3.3 - 2.5 \frac{f_y^*}{f_y}\right) E_p \quad (2-14)$$

$$E_p = 0.025 E_s \text{ or } 10 f_y \quad (2-15)$$

$$f_s = f_{\max} \quad \text{when} \quad f_s \geq f_{\max}$$

$$\varepsilon_{sc} = \frac{f_{\max} - f_y'}{E_p'} + \varepsilon_y' \quad (2-16)$$

where,

$$\varepsilon_y' = \frac{f_y'}{E_s} \quad (2-17)$$

$\varepsilon_{sc}$  is the maximum strain used in the model

and  $\varepsilon_y'$  is the equivalent yield strain for the bilinear stress-strain curve.

### Park and Paulay Steel Model

Park and Pauley (1975) proposed a steel model in their book *Reinforced Concrete Structures*. The model uses the principles of strain hardening. As can be seen in Figure

2-19, the model is elastic up to the yield strength of the steel followed by a purely plastic region and a strain-hardening region. The model can be described by the following equations.

Region AB.

$$f_s = E_s \varepsilon_s \quad \text{For } (\varepsilon_s < \varepsilon_y) \quad (2-17)$$

Region BC.

$$f_s = f_y \quad \text{For } (\varepsilon_y \leq \varepsilon_s < \varepsilon_{sh}) \quad (2-18)$$

Region CD.

$$f_s = f_y \left[ \frac{m(\varepsilon_s - \varepsilon_{sh}) + 2}{60(\varepsilon_s - \varepsilon_{sh}) + 2} + \frac{(\varepsilon_s - \varepsilon_{sh})(60 - m)}{2(30 + r + 1)^2} \right] \quad \text{For } (\varepsilon_y \leq \varepsilon_s < \varepsilon_{sh}) \quad (2-19)$$

where.

$$m = \frac{\left(\frac{f_u}{f_y}\right)(30 + r + 1)^2 - 60r - 1}{15r^2} \quad (2-20)$$

$$r = \varepsilon_{su} - \varepsilon_{sh} \quad (2-21)$$

and.

$\varepsilon_{su}$  is the ultimate strain.

$f_u$  is the ultimate stress.

$m$  and  $r$  are variables of the equation.

$f_y$  is the yield strength of the steel.

$f_s$  is the compressive stress at a point on the curve.

$E_s$  is the modulus of elasticity for the steel.

$\varepsilon_{sh}$  is the strain when strain hardening begins.

$\varepsilon_s$  is the strain at a point on the curve.

## **Finite Element Method**

The Finite Element Method (FEM) involves using numerical techniques to find approximate solutions to partial differential equations which many physical phenomena in engineering can be described. It can be used to solve various field problems such as stress analysis, heat transfer and fluid flow employing the use of computer simulation.

The FEM was developed in the 1950's to solve complex structural analysis problems in aerospace, civil, and aeronautical engineering. The first paper to describe the major ideas was written by M.J. Turner, R.W. Clough, H.C. Martin and L.J. Topp and published in 1956 but failed to use the term 'finite elements' (Fish and Belytschko 2007). Ray Clough, the second author on the paper, is typically referred to as one of the founders of the method after publishing a paper coining the term 'finite elements'. The work of these men inspired other professors and graduate students at Berkeley to define the center of finite element research for many years. Their research was taking place at a time when computing power was rising exponentially with time and allowed the method to develop fairly quickly. Their research was quickly put to use in the defense, nuclear power aeronautical and automotive industries (Fish and Belytschko 2007).

The approach involves dividing a body into finite elements connected to one another by nodes to obtain approximate solutions to the field problem in question. These divided elements and nodes make up the mesh. The process of making the mesh is called the mesh generation.

The FEM uses a systematic approach to solve for the unknowns in the system. Linear and non-linear problems can be solved using finite element analysis (FEA) by solving a system of equations for the unknowns which equal the number of nodes

generated during meshing. In general, the accuracy of the solution improves as the number of elements increase but computational requirements and cost also increase with an increase in mesh density. Results can be output in the way of computer visualizations through post-processing (e.g. contour plots) as well as output to data files where it can be analyzed for use in the design process.

Software packages began to be available in the 1960's. Early software packages such as NASTRAN, a program funded by NASA, and ANSYS, a program developed at Westinghouse Electric by John Swanson, included capabilities such as two- and three-dimensional stress analysis, vibration analysis, dynamic loading and both linear and non-linear analysis. More recent FE programs such as LS-DYNA and ABAQUS began as non-linear codes used for dynamic analysis and have evolved to include linear capabilities as well (Fish and Belytschko 2007).

There are very few reported efforts in the literature on the use of commercial FEA software packages, such as the ones listed in the previous paragraph, for validating and predicting tests on UHPC specimens. Rong et al. (2010) performed Split Hopkinson pressure bar tests to study the compression behavior of UHPC dynamically loaded. The authors also used the FEA software package LS-DYNA to perform numerical modeling for comparison. They had good agreement from the experimental and numerical studies, but with most FEA analysis, the material properties were calibrated to fit the experimental data which cannot be applied to different cases with expectations of reliable results. A specific material model will need to be developed for UHPC in order to advance the capabilities of numerical modeling of various types of specimens and cases.

There also exists no reported effort on studying the direct shear behavior of push-off specimens through the use of finite elements. While typical bending and axial behavior has been studied previously with good results, push-off specimens have yet to be modeled with precise accuracy.

### **Verification and Validation**

Verification of a finite element code is performed to ensure the accuracy of a solution generated by the code by verifying it to a well-known solution. This process is usually performed by the software company for each specific FE code. For special applications, one might need to perform verification to improve the confidence of a specific model.

Validation is the process of comparing a numerical model to real world or experimental data to assess the accuracy of the model. Considerations must be taken during this process to closely depict the real world conditions such as loading, boundary conditions, instrumentation, etc. If the mathematical model built in the FE code does not accurately describe the real world conditions, the solutions obtained can be questionable.

### **Finite Element Code Abaqus**

The following review of relevant features of Abaqus to this study is based on Abaqus Version 6.11 documentation (Simulia 2011). Abaqus is a general-purpose finite element analysis package which has a variety of applications such as structural response, heat transfer, acoustics, soil mechanics and fluid dynamics. It also includes the capabilities to couple these various applications. It was originally designed to model non-linear physical behavior and thus has an extensive library of material models for this purpose.

It includes three analysis products; Abaqus/Standard, Abaqus/Explicit, and Abaqus/CFD. Abaqus/Standard can be used to solve both static and quasi-static problems while Abaqus/Explicit is mainly used for highly dynamic problems such as blast and impact events.

Abaqus/Standard employs an implicit integration solution process. This means that it must solve multiple equations at each solution time step and the global stiffness matrix,  $K$ , must be inverted to arrive at a solution. This can be a disadvantage as a full inversion of the stiffness matrix is required and equilibrium must be satisfied at each time step. This can lead to solution convergence issues for non-linear models and can be computationally expensive, compared to explicit integration.

Abaqus/Explicit uses an explicit integration solution process. Explicit integration method satisfies the equation of motion at the current time ( $t_i$ ) and extrapolates to determine the solution for the next time step ( $t_{i+1}$ ). This solution process requires the time steps to be small enough to minimize errors when extrapolating to the next time step. This small time step requirement is useful when trying to model non-linear behavior and dynamic events and makes Abaqus/Explicit more applicable to these types of problems.

### **Concrete material models**

Three concrete specific material models are available in Abaqus; concrete smeared cracking model, cracking model for concrete, and the concrete damaged plasticity model (CDP). These models can be used for modeling plain and reinforced concrete sections although they are intended for analysis of reinforced concrete structures. The smeared cracking model can only be used in Abaqus/Standard and the

cracking model for concrete can only be used in Abaqus/Explicit. The CDP model can be used in both Abaqus/Standard and Explicit.

For this study, the CDP model is used as the concrete material model. It is a continuum, plasticity based model which also accounts for concrete damage and is suitable for structures subjected to monotonic, cyclic and/or dynamic loading under low confining pressures. It uses damaged elasticity in combination with tensile and compressive plasticity to represent the inelastic behavior of concrete. The two main failure mechanisms are compressive crushing and tensile cracking of the concrete. In order to describe these behaviors, stress-strain input for both compression and tension must be specified by the user.

The model assumes the uniaxial compressive stress-strain curve, Figure 2-18, is characterized by damaged plasticity. The response is linear up to the yield point, strain hardening takes place up to the ultimate stress, and strain softening occurs past the ultimate stress until failure.

The CDP model also assumes the uniaxial tensile response is characterized by damaged plasticity, as shown in Figure 2-22. The stress-strain response follows a linear elastic relationship until the failure stress is reached. The failure stress corresponds to the point in which the concrete starts to develop micro-cracks. The micro-cracking is represented globally by a softening stress-strain response, which causes strain localization in the concrete, after the peak stress. The post failure behavior is represented by tension stiffening. Abaqus allows the user to define the strain-softening behavior for the cracked concrete directly. This behavior represents a simplified approach to the interaction between the concrete and the reinforcement such as dowel

action and bond slip. Users can specify tension stiffening by means of a post failure stress-strain relation or by using a fracture energy criterion. . Abaqus recommends reducing the failure stress over an ultimate failure strain of 10 times the initial failure strain. Too little tension stiffening can cause local failure of the concrete due to cracking leading to unstable behavior in the concrete. While these representations are fairly simplified, they capture the main response mechanisms of the concrete fairly well.

### **CDP material model parameters**

Plasticity parameters are required in order to fully define the material properties in Abaqus for the CDP concrete model. These include the dilation angle,  $\varphi$ , the flow potential eccentricity,  $\varepsilon$ , the compressive stresses ratio,  $f_{bo} / f_{co}$ , the stress invariant ratio,  $K$ , and the viscosity parameter,  $\mu$ .

The dilation angle is the angle in the p-q plane under high confining pressures and is caused by plastic distortion. This distortion can be represented by a suitable plastic (Malm 2009) potential function,  $G$ . Abaqus employs the Drucker-Prager hyperbolic plastic potential function shown in Figure 2-23. Nielsen (1999) found a relationship between the friction,  $\phi$ , angle and the dilation angle,  $\varphi$ , of concrete as  $\sin(\phi) = \tan(\varphi)$ .

Malm (2009) summarized various reports in the literature on dilation angle values and his findings suggest a range between 25-40 degrees is most suitable when using the CDP material model for conventional concrete.

$f_{bo} / f_{co}$ , the compressive stresses ratio, defines the ratio of the equibiaxial compressive strength to the initial uniaxial strength. Abaqus uses a default value of 1.16

$\varepsilon$ , which is the flow potential eccentricity, defines the rate at which the plastic potential, as shown in Figure 2-23, approaches the asymptote. The plastic potential is a straight line when  $\varepsilon$  is zero. Abaqus uses a default value of 0.1.

$K$  is the ratio of the second stress invariant on the tensile meridian to that of the compressive meridian. The default value in Abaqus is 0.667.

The viscosity parameter,  $\mu$ , is used to describe the viscoplastic regularization of the constitutive law for concrete. The default value in Abaqus/Standard is zero but this parameter is not used in Abaqus Explicit. It can be used to resolve convergence issues in an implicit analysis where the material model employs a softening behavior.

### **Reinforcement material models**

Reinforcement can be modeled by using a combination of linear elastic and classical metal plasticity material models in Abaqus. By utilizing both material models, reinforcement behavior can be defined. If damage needs to be applied to the model, in the case of highly dynamic loads, etc., these material models can be used in conjunction with progressive damage and failure models in Abaqus. These allow the user to specify different damage initiation and damage evolution criteria that allow for progressive degradation of the material stiffness as well as the removal of elements from the analysis.

### **Elements**

Abaqus offers a variety of element types to model many different problems. Abaqus/Standard and Abaqus/Explicit offers two separate element libraries. Certain elements can only be used in Abaqus/Standard. Described here are the elements used and in this study. For further information on the extensive element library available in Abaqus, please refer to the Abaqus user manual.

C3D8R elements, as shown in Figure 2-24 are commonly used to model concrete. The C3D8R elements are 8-node continuum elements with reduced integration and hourglass control. This element has one integration point per face as opposed to the four integration points per face for a non-reduced integration brick element, see Figure 2-25 . This prevents shear locking from occurring and also drastically reduces running time for non-linear problems. Enhanced hourglass control is also utilized in the model. This method gives more accurate displacement solutions for models with coarse meshes compared to other hourglass control methods. It also provides increased resistance to hourglassing for nonlinear materials. This hourglass method may give overly stiff response in problems displaying plastic yielding under bending, which is not an issue for the shear behavior of the model.

B31 elements are commonly used to model embedded reinforcement, see Figure 2-26. B31 elements are linear 2-node beam elements which employ the Timoshenko beam theory, accounting for transverse shear strain. This allows for a shear flexible element which is needed in accurately modeling the stirrups crossing the shear plane. Meley and Krauthammer (2003) showed that beam elements, in lieu of truss elements which only resist axial forces, more accurately model the reinforcement in both shear and bending.

### **Direct Shear Behavior**

Direct shear is classified as a sliding type failure along a well-defined plane, where slip occurs perpendicular to the axis of the member. Shear failure in structural members can occur suddenly and have catastrophic effects. This is especially true for critical sections, near supports for example, in systems where reinforcement placement may be

extremely difficult to place in reality. Failure in direct shear can happen under static loading conditions or during dynamic events such as blast loading.

Direct shear or dynamic shear as it is also referred, can occur in structural systems where very high, short duration impulsive loads are generated (Slawson 1984). The failure behavior is essentially a vertical shear of the section that results in a rupture of the reinforcing bars crossing the shear plane. The direct shear failure response occurs when the member subjected to the load has no time to react in a flexural mode. It occurs very early in the loading phase, roughly one millisecond, before any significant flexural response can occur. If the member does not fail in direct shear over the initial loading phase, a flexural mode of failure dominates (Slawson 1984). In contrast, diagonal or flexural shear is characterized by cracks that form at an angle to the horizontal plane and occurs where both shear and flexural stresses exist in the member. Diagonal shear will occur when the primary response of the system is flexure. Krauthammer et al. (1986) proposed the uncoupling of the direct shear response from the flexural response and concluded that the shear mechanism in direct shear is similar in nature to shear transfer across an uncracked concrete interface as described by Park and Paulay (1975).

This behavior has been reported in slabs subjected to severe and rapid loading by Kiger and Getchell (1980) and Slawson (1984). While some slabs exhibited flexural failure, others failed in direct shear. Figure 2-27 shows a photograph of the roof slab of a RC buried box structure that failed due to direct shear. The shear failure created a vertical failure plane at the supports. While the side walls appear practically undamaged, the roof slab sheared off completely at the side walls. The top and bottom

reinforcement experienced necking before being severed nearly flush with the failure plane.

### **Experimental Work**

Several different types of test specimens have been used over the years to study shear transfer. The most common is the so-called push-off specimens, shown below in Figure 2-29. These specimens allow the study of the shear interface and the transfer of shear stresses through the shear plane. Hofbeck et al. (1969) and Mattock and Hawkins (1972) reported tests where the specimens either did or did not have pre-cracked shear planes. Other variables were the amount and type of reinforcement crossing the shear plane. The failure load and amount of transverse reinforcement were reported. Walraven and Reinhardt (1981) also conducted studies on push-off specimens. The testing included a series of specimens with embedded reinforcing bars and also specimens with external restraint bars.

Valle and Buyukozturk (1993) studied the effect of high strength concrete with fibers on push-off specimens to generate a model to describe the shear transfer. Tests also included normal strength concrete push-off tests. The model predicts the shear stress-shear strain relationship for an element in the shear plane. Below is a summary of the tests performed by these studies.

#### **Hofbeck et al. (1969) and Mattock and Hawkins (1972)**

Thirty-eight push-off specimens were tested in the 1969 study “Shear Transfer in Reinforced Concrete”. Of these, fifteen were uncracked while the remaining twenty-three were initially cracked along the shear plane. The push-off specimens had a shear plane equal to 50 in.<sup>2</sup> (32,258 mm<sup>2</sup>). The geometry is shown in Figure 2-30.

The main objectives of the study were to determine the influence of a pre-existing crack along the shear plane on the shear transfer strength, the reinforcement crossing the shear plane (strength, size and arrangement), and the concrete strength on the shear transfer strength. Other objectives included examining dowel action of the reinforcing bars on the shear strength and also the applicability of the “shear friction” theory presented by Birkeland and Birkeland (1966) and Mast (1968) on specimens that were initially cracked along the shear plane. Typical load-slip curves are shown in Figure 2-31.

The specimens that were initially uncracked generally have less slip than specimens with initially cracked shear planes. The ultimate shear stress generally reduces with initially cracked specimens as well. The variable  $\rho f_y$  was used to normalize the test results where  $\rho$  is the total cross section of the stirrups crossing the shear plane,  $A_s$ , divided by the area of the shear plane,  $bd$ . It was concluded that the way in which  $\rho$  changed did not affect the shear strength.

Two series, 2 and 5, were used to compare the effects of the concrete strength on the shear transfer strength. They were both initially cracked and were identical in every way except concrete strengths, Series 2 having 4,000 psi concrete and Series 5 having 2,500 psi concrete. Figure 2-32 shows the results. They concluded that the concrete strength appears to set an upper limit on the value of  $\rho f_y$ , below which the relationship between  $v_u$  and  $\rho f_y$  is the same for concretes of strength equal to or greater than that of the concrete being considered, and above which the shear transfer strength increases at a much reduced rate.

The different cracking patterns of the uncracked and initially cracked specimens were determined to be the cause of the differing effects of dowel action. The uncracked specimens, where cracking happens via short diagonal cracks crossing the shear plane, as illustrated in Figure 2-33, create concrete struts that rotate causing the measured slip. This puts the reinforcement into tension as a truss-like action develops, instead of in a shearing action at the shear plane. Mattock believes this is why no dowel action is observed in the uncracked specimens. In the initially cracked specimens, the reinforcement crosses the crack, and therefore the shear plane, at a 90° angle, creating a shearing action on the reinforcement from the concrete on either side of the crack. This allows dowel action to be developed in the bars crossing the shear plane.

In summary, both papers findings are as followed.

1. A pre-existing crack along the shear plane will reduce the ultimate shear transfer strength and will increase the amount of slip at all levels of load.
2. The shear transfer strength is a function of the reinforcement ratio multiplied by the yield strength of the reinforcement,  $\rho f_y$ .
3. In initially cracked specimens, the concrete strength sets an upper limit value for  $\rho f_y$ , below which the relationship between  $v_u$  and  $\rho f_y$  is the same for concretes of strength equal to or greater than that of the concrete being considered, and above which the shear transfer strength increases at a much reduced rate.
4. Dowel action of bars crossing the shear plane is trivial in uncracked concrete but is significant in initially cracked concrete.
5. The shear friction theory gives reasonably conservative estimates of shear transfer strength in NSC with a pre-existing crack along the shear plane
6. The Zia failure envelope can be used to derive the relationship between  $\rho f_y$  and the shear transfer strength for uncracked concrete

## **Walraven and Reinhardt (1981)**

Walraven and Reinhardt developed a theoretical model along with an experimental program to study the mechanism of aggregate interlock. The model is based on the assumption that concrete is a two phase material consisting of the aggregate particles with high strength and stiffness (phase I) and the cement matrix consisting of the fine particles (phase II), sand and cement, with a lower strength and stiffness. A crack in the composite material will generally intersect the matrix while going around the aggregate particles. This creates a rough surface for aggregate interlock to occur along the cracked plane as shown in Figure 2-34.

Push-off specimens with embedded reinforcing bars, external restraint bars or plain concrete were used in the study. The external restraint bars were used because it is not possible to measure the steel stress in a bar at a crack when it is simultaneously pulled by normal forces and transversely pressed by dowel action. For brevity and relevance, the tests with external restraint bars will not be included here. Variables of the tests included the reinforcement ratio, bar diameter, concrete strength, roughness of the crack plane, effect of inclination of the stirrups to the crack plane and dowel action.

Reinforcement ratios ranged from 0.14% to 3.35%. Bar diameter was investigated by holding the reinforcement ratio constant while changing bar sizes. Three concrete strengths of 20, 30/35, and 56 N/mm<sup>2</sup> (approximately 2,900, 4,350/5,075, and 8,100 psi) were used for comparison. The effect of roughness of the crack plane was studied by employing a special gap-graded mix and also using a sanded lightweight mix. Angles of inclination of the stirrups relative to the shear plane included in the study were 45°, 60°, 67.5°, 75°, 105°, 112.5°, 120° and 135°. The presence of dowel action was studied by

including specimens with soft sleeves of 20 mm (approximately 0.75 in.) over the stirrups on both sides of the crack.

The geometry of the test specimens used was similar to that of Mattock and Hawkins (1972) and is shown in

Figure 2-35. The geometry produced a shear plane of  $36,000 \text{ mm}^2$  (300 x 120 mm) in area. The reinforcement crossing the shear plane was in the form of closed stirrups to provide adequate anchorage on both sides of the shear plane. Additional reinforcement was used as shown in Figure 2-36 to ensure that the failure would be along the shear plane. This is typical of push-off tests in the literature.

**Results of tests with embedded bars.** It was found that an increase in reinforcement ratio and also an increase in concrete compressive strength lead to an increased maximum shear stress. Most of the tests reached their maximum shear stress at a shear displacement greater than 0.5 mm (0.02 in.). This is summarized in Figure 2-37 where the maximum shear displacement,  $T_{\max}$ , is plotted against the concrete compressive strength,  $f_{cc}$ , and the mechanical reinforcement ratio,  $\rho f_{sy}$ . The influence of particle size and lightweight aggregate had almost no effect unless the mechanical reinforcement ratio was low. As one would expect, the lightweight concrete had lower maximum shear stresses and the mix with the larger diameter aggregate had higher maximum shear stresses.

The crack width was also measured during the whole loading cycle during testing. This allows the comparison of crack opening under certain shear stresses as a function of various reinforcement ratios. From the results, it can be stated that by increasing the

reinforcement ratio at all shear stresses, the crack width decreases. This can be seen in Figure 2-38, showing mix No. 1-3 as well as the lightweight concrete mix.

By comparing different bar sizes and holding the reinforcement ratio constant, it was found that no significant difference could be found. Bar sizes ranged from 6 to 16 mm. Concerning the effect of roughness of the crack, no significant difference between the gap-graded and continuously graded mixes could be found. From Figure 2-39, it can be seen that mix No. 3, the high quality gravel mix, and the lightweight mix show the least crack widths,  $W$ , at the same shear displacements,  $\Delta$ . This can be attributed to the surface roughness being less than the other mixes.

By varying the angle of inclination of the reinforcement crossing the shear plane it can be seen that the smaller angles are the most efficient at producing the highest shear stress for any shear deflection as shown in Figure 2-40.

The dowel action in embedded reinforcing bar specimens was studied by providing soft sleeves of 20 mm on each side of the shear plane as shown. This will not allow bond stresses to develop under loading and the crack will open up and be constant across the vertical plane. For deformed bars, the bond stresses develop and cause a reduction in the crack width in the vicinity of the bars. These two different crack opening patterns can be seen in Figure 2-41. The diagonal cracking that occurs along the shear plane can be explained by these bond stresses that develop and the concrete compression strut that forms from the tension in the reinforcing bars. This behavior can be seen in Figure 2-42.

### **Valle and Buyukozturk (1993)**

Valle and Buyukozturk (1993) investigated the behavior of normal and high strength concrete, both with and without fibers, under direct shear both experimentally

and through modeling. Like previous studies, push-off specimens were used, shown in Figure 2-43, with varying parameters such as the strength of concrete, type of fibers, and stirrups crossing the shear plane. All the specimens tested were initially uncracked along the shear plane. A previous analytical model describing shear transfer strength by Hsu et al. (1987) was modified to predict the shear stress-shear strain behavior for the specimens involving high strength concrete and specimens containing fibers. The Hsu model is based on a truss model theory that takes into account the softening of concrete in compression due to the propagation of cracks. The modified shear transfer model is presented later in this section.

Table 2-7 shows an overview of the test specimens organized by type and shear reinforcement. . The test specimen nomenclature is as follows. normal strength concrete (NC), steel fiber reinforced normal strength concrete (SNC), polypropylene fiber reinforced normal strength concrete (PNC), high-strength concrete (HC), steel fiber reinforced high-strength concrete (SHC) and polypropylene fiber reinforced high strength concrete (PHC). The test specimens that included stirrups crossing the shear plane include an “S” at the end of the notation. There were two specimens for each specimen type that were tested. The results are shown in Table 2-8 for NSC and Table 2-9 for HSC.

The NSC specimens had an average compressive strength of approximately 4,200 psi, while the HSC specimens had an average compressive strength of approximately 10,000 psi. From the experimental data, it can be seen that all specimens with fibers, especially in the HSC mixes, improved the ductility and shear strength. Polypropylene fibers were less effective than steel fibers. When fibers and stirrups were combined in

HSC, a significant improvement in ductility was seen over NSC with stirrups alone. All mixes containing fibers had a 1.0% by volume fraction of fibers and specimens with stirrups had a reinforcement ratio of 1.47%.

The observed failure modes of the specimens containing no stirrups or fibers, in both the NC and HC, were very brittle and sudden as one would expect. Specimens reinforced with fibers alone developed very small diagonal cracks along the shear plane as shown in

Figure 2-44(a). For the SNC, PNC, and PHC specimens, failure was observed when the small diagonal cracks joined together across the entire shear plane and the fibers bridging the crack pulled out. In the SHC specimens the same behavior was observed but after the maximum load was reached, a softening behavior with a rapid drop in load occurred. This may have been caused due to some of the steel fibers yielding in tension while bridging the crack. Valle and Buyukozturk (1993) believe that this behavior can be attributed to the increase in bond provided by the HC.

The failure for all specimens with stirrups crossing the shear plane occurred with the formation of discrete diagonal cracks crossing the shear plane at an angle of  $50^{\circ}$  to  $75^{\circ}$  with respect to the horizontal as seen in

Figure 2-44(b). These diagonal cracks formed concrete compressive struts and tensile forces in the stirrups creating a truss-like action. Ultimate failure occurred when the compressive struts failed in compression, crushing the concrete. This type of failure has also been observed and discussed by Walraven and Reinhardt (1981) as depicted in Figure 2-42.

The modified shear transfer model developed by Valle and Buyukozturk (1993) applied to the high-strength concrete with steel fibers gave good agreement with the test results as shown in Figure 2-45 and it is worth noting that the predicted values were conservative. Results from the polypropylene reinforced high-strength concrete also gave good predictions when compared to the experimental results.

## **Numerical Models**

### **Original and modified Hawkins shear models**

Mattock and Hawkins (1972) proposed a model for direct shear based on the shear stress-slip relationship. The model describes the shear transfer of reinforced concrete members with well anchored main reinforcement without compressive forces in the static domain. Krauthammer et al. (1986) modified Hawkins model to account for compression and rate effects produced by severe dynamic loads. Hawkins original model can be found described in great detail by Murtha and Holland (1982). The modification proposed by Krauthammer et al. (1986) was employed by applying an enhancement factor of 1.4 to account for the effects of compression and rate effects. The original Hawkins model and the modified model are represented in Figure 2-46.

A direct shear failure occurs at the last point on the model, point E, where the slip has reached the ultimate slip,  $\Delta_{max}$ . The difference between the Hawkins model and the enhanced or modified model by Krauthammer is a factor, K, designated to account for compressive effects and strain rate effects. The factor was determined to be equal to 1.4. This includes the dynamic effects stated above and modifies the original static model to be applicable in the dynamic domain. Below, the various line segments of the model are described.

**Segment OA.** The response in this region is elastic and the slope  $K_e$ , is defined by the shear resistance,  $\tau_e$ , for a slip of 0.004 in. (0.1 mm). The resistance is given by the expression,

$$\tau_e = 165 + 0.157 f'_c \quad (2-18)$$

in which both  $\tau_e$  and  $f'_c$  are in psi. The initial response elastic limit should be taken as no greater than  $\tau_m/2$ .

**Segment AB.** The slope of the curve decreases continuously with increasing displacements until a maximum strength,  $\tau_m$ , is reached at a slip of 0.012 in. (0.3mm).

The maximum strength,  $\tau_m$ , is given by the expression,

$$\tau_m = 8\sqrt{f'_c} + 0.8\rho_{vt}f_y \quad (2-19)$$

where  $\tau_m$ ,  $f'_c$ , and  $f_y$  are in psi,  $\rho_{vt}$  is the ratio of total reinforcement area to the area of the plane it crosses and  $f_y$  is the yield strength of the reinforcement crossing the plane.

**Segment BC.** The shear capacity remains constant with increasing slip. Point C corresponds to a slip of 0.024 in. (0.6 mm).

**Segment CD.** The slope of the curve is negative, constant and independent of the amount of reinforcement crossing the shear plane. The slope, in units of psi/in., is given by the expression,

$$K_u = 2,000 + 0.75 f'_c \quad (2-20)$$

**Region DE.** The capacity remains essentially constant until failure occurs at a slip of  $\Delta_{max}$ . For a well-anchored bar the slip at failure is given by the expression,

$$\Delta_{max} = 2 \left( \frac{e^x - 1}{120} \right) \quad (2-21)$$

where,

$$x = \frac{900}{2.86 \sqrt{\frac{f'_c}{d_b}}} \quad (2-22)$$

and  $d_b$  is the bar diameter in inches.

The limiting shear capacity,  $\tau_L$ , is given by the expression,

$$\tau_L = \frac{0.85 A_{sb} f'_s}{A_c} \quad (2-23)$$

Where  $A_{sb}$  is the area of bottom reinforcement crossing the shear plane,  $f'_s$  is the tensile strength of the reinforcement and  $A_c$  is the cross-sectional area.

### **Modified shear transfer model**

The modified shear transfer model used by Valle and Buyukozturk (1993) is based on a truss model theory presented by Hsu et al. (1987) that considers the softening of concrete in compression due to the propagation and interaction of cracks. The objective of the model is to predict the shear stress vs. shear strain relationship for the element shown in Figure 2-47. The truss action must satisfy equilibrium, compatibility and material laws.

The concrete is assumed to behave linear-elastically until first cracking occurs. The model accounts for the softening of concrete in tension before cracking caused by compressive stresses in the orthogonal direction. Empirical constants were used for this behavior, by which the tensile stiffness was multiplied, and determined to be 0.35 for normal and 0.40 for high strength concrete. For precracking behavior, it was assumed and determined experimentally later that the shear strain distribution along the shear plain is parabolic as shown in Figure 2-48. After cracking, the shear stresses are uniformly distributed along the shear plane. This was also confirmed from experimental results.

Below is a presentation of the modified shear transfer model.

**Material law for steel reinforcement.** For all steel reinforcing bars, the steel is assumed to behave as an elastic-perfectly plastic material represented by the following equations.

$$f = E_s \varepsilon \quad \text{for} \quad \varepsilon < \varepsilon_y \quad (2-24)$$

$$f = f_y \quad \text{for} \quad \varepsilon \geq \varepsilon_y \quad (2-25)$$

where,

$\varepsilon$  = normal strain

$f$  = stress in the steel

$E_s$  = modulus of elasticity of steel

$f_y$  and  $\varepsilon_y$  are the yield stress and strain for steel, respectively.

**Material law for concrete.** The model takes into account the different types of concrete used, normal and high strength with and without fibers, and uses different stress-strain behaviors for tension and compression for these materials.

**Compressive behavior of concrete.** All concrete types were assumed to behave basically in the same manner, as shown in Figure 2-49, but with different parameters for strain values corresponding to the peak strain and the ultimate strain. The numerical values used are given in Table 2-10 at the end of the model description. The ascending branch behavior of the stress-strain curve is described mathematically below.

$$\sigma_d = f_c' \left[ 2 \left( \frac{\varepsilon_d}{\varepsilon_o} \right) - \lambda \left( \frac{\varepsilon_d}{\varepsilon_o} \right)^2 \right] \quad \text{for} \quad |\varepsilon_d| \leq |\varepsilon_p| \quad (2.26)$$

$$\lambda = \sqrt{0.7 - \frac{\varepsilon_r}{\varepsilon_d}} \quad (2.27)$$

where,

$\epsilon_d$  = compressive strain of concrete

$\epsilon_o$  = peak strain for uniaxial compression

$\epsilon_p = \epsilon_o/\lambda$

$f_c'$  = cylinder compressive strength

$\epsilon_r$  = tensile strain of concrete

$\lambda$  is the coefficient that incorporates the softening of concrete due to tensile stresses in the orthogonal direction.

The descending branch behavior of the stress-strain curve is described mathematically below for normal strength concrete with or without fibers.

$$\sigma_d = \frac{f_c'}{\lambda} \left[ 1 - \left( \frac{\frac{\epsilon_d - \frac{1}{\lambda}}{\epsilon_o}}{2 - \frac{1}{\lambda}} \right)^2 \right] \quad \text{for} \quad |\epsilon_d| > |\epsilon_p| \quad (2-28)$$

The descending branch behavior of the stress-strain curve is described mathematically below for high strength concrete with or without fibers.

$$\sigma_d = \frac{f_c'}{\lambda} - 0.15 f_c' \frac{(\epsilon_d - \epsilon_p)}{(\epsilon_u - \epsilon_o)} \quad \text{for} \quad |\epsilon_d| \leq |\epsilon_p| \quad (2-29)$$

Different values for  $\epsilon_o$  and  $\epsilon_u$  are used according to the type of concrete. See Table 2-10.

**Tensile behavior of concrete.** For all concrete types, precracking behavior was assumed to be similar. After cracking, the behavior was modified according to whether or not the mix contained fibers. Figure 2-50 is a graphical representation of the tensile stress-strain behavior. Below describes mathematically concrete with fibers.

$$E_{ct} = C(E_{mt} V_{mt} + E_f V_f \eta_1 \eta_0) \quad (2-30)$$

$$E_{mt} = 40,000 \sqrt{f_c'} + 1,000,000 \cdot psi \quad (2-31)$$

where,

$E_{ct}$  = modulus of composite in tension (psi)

$E_{mt}$  = modulus of concrete (psi)

$C$  = empirical constant, NC = 0.35, HC = 0.40

$V_{mt}$  = volume percent of concrete in mix

$E_f$  = modulus of fibers

$V_f$  = volume percent of fibers in mix

$\eta_0 = 0.14$ , orientation factor

$\eta_1$  = length efficiency factor

Below describes mathematically concrete with fibers.

$$E_{ct} = CE_{mt} \quad (2-32)$$

Using the above equations, the precracking behavior of concrete in tension, can be defined as,

$$\sigma_r = E_{ct}\epsilon_r \quad \text{for} \quad \epsilon_r \leq \epsilon_{cr} \quad (2-33)$$

where,

$$\epsilon_{cr} = \frac{f_{cr}}{E_{ct}} = \text{cracking strain}$$

$$f_{cr} = 7.5\sqrt{f'_c} \cdot \text{psi for normal strength concrete without fibers}$$

$$f_{cr} = 6\sqrt{f'_c} \cdot \text{psi for high strength concrete without fibers}$$

The cracking strain for specimens with fibers is calculated using the following formula.

$$\epsilon_{cr} = \eta_1\eta_0' V_f (\epsilon_{fp} - \epsilon_{mp}) + \epsilon_{mp} \quad (2-34)$$

where,

$\eta_0' = 0.405$ , orientation factor at cracking

$\epsilon_{fp}$  = strain at the proportionality limit for the fibers

$\epsilon_{mp}$  = strain at the proportionality limit for the matrix

Postcracking behavior for normal strength and high strength concrete without fibers can be defined as follows.

$$\sigma_r = \frac{f_{cr}}{1 + \sqrt{\frac{\epsilon_r - \epsilon_{cr}}{0.005}}} \quad \text{for} \quad \epsilon_r > \epsilon_{cr} \quad (2-35)$$

Postcracking behavior for concretes with fibers, the behavior is assumed to be bilinear as expressed by the following equations.

$$\sigma_r = f_{cr} + E_f V_f \eta_1 \eta_0 (\epsilon_r - \epsilon_{cr}) \quad \text{for} \quad \epsilon_{cr} < \epsilon_r < \epsilon_{cr2} \quad (2-36)$$

$$\sigma_r = f_u - E_f V_f \eta_1 \eta_0 (\epsilon_r - \epsilon_{cr2}) \quad \text{for} \quad \epsilon_r > \epsilon_{cr2} \quad (2-37)$$

where,

$$\epsilon_{cr2} = \epsilon_{cr} + \frac{\sigma_{sfu}}{E_{sf}}, \text{ strain at peak tensile load}$$

$$f_u = f_{cr} + \eta_1 \eta_0' V_{sf} E_{sf}$$

$\sigma_{sfu}$  = ultimate steel fiber strength

$E_{sf}$  = ultimate steel fiber modulus

By combining these equations of equilibrium and compatibility with the material laws, a system of 11 non-linear equations are formed involving 14 unknowns. For the shear transfer problem, the stresses acting on the element located at the shear plane are shown in Figure 2-47(c). Here  $\tau_{lt}$  is the average shear stress acting on the plane and is equal to,

$$\tau_{lt} = \frac{P_t}{LH} \quad (2-38)$$

where,

$P_t$  = externally applied load

L and H are defined in Figure 2-47(a) and Figure 2-47(b)

Furthermore,  $\sigma_t$  and  $\tau_{lt}$  can be related by,

$$\sigma_t = K\tau_{lt} \quad (2-39)$$

and,

$$\sigma_l = 0 \quad (2-40)$$

where,

$K = L/B$ , with  $L$  and  $B$  defined in Figure 2-47

By substituting Equations 2-38, 2-39 and 2-40 into the previously described equations, a solution for shear stress,  $\tau_{lt}$ , and shear strain,  $\gamma_{lt}$ , can be found for a given value of  $\epsilon_d$ . A detailed description of the solution procedure can be found in Hsu et al. (1987).

### **Summary**

This chapter was devoted to the review of the materials and procedures related to shear transfer and the direct shear phenomenon. Ultra-high performance concrete, normal strength concrete and mild steel reinforcement were summarized. The finite element method was summarized next followed by direct shear and shear transfer behavior of concrete and the corresponding related literature.

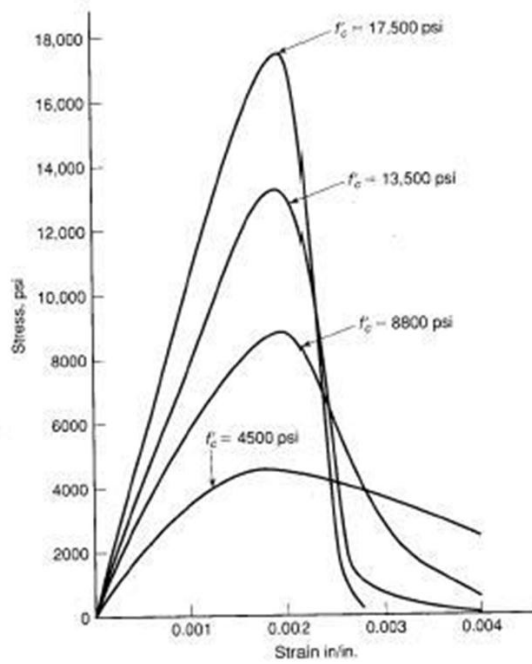


Figure 2-1. Typical concrete stress-strain curves in compression (Wight and MacGregor 2008)

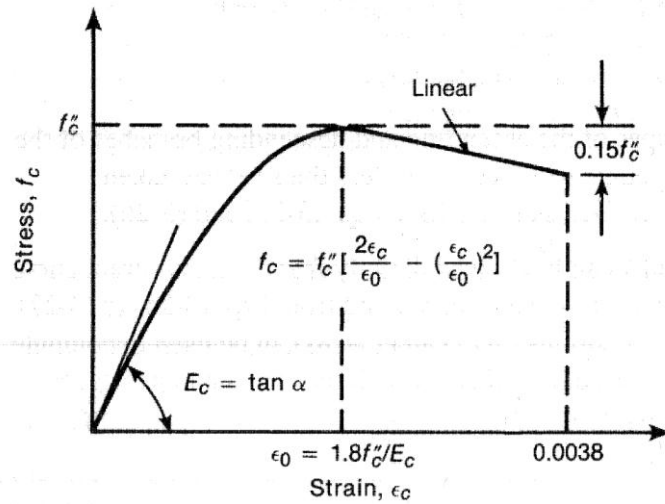


Figure 2-2. Modified Hognestad curve for concrete in compression (Wight and MacGregor 2008)

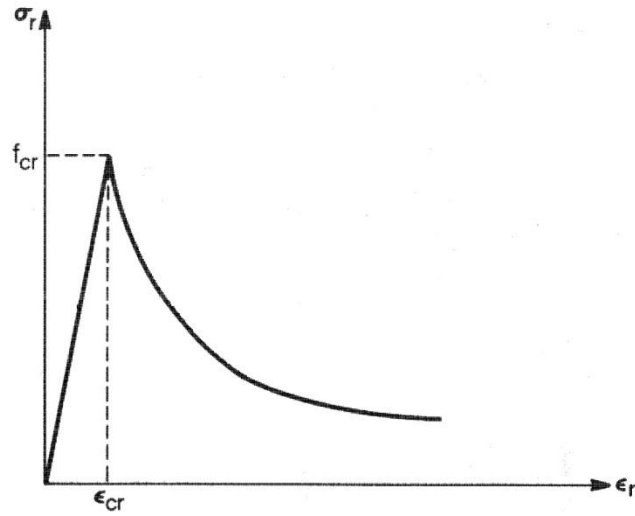


Figure 2-3. Tensile stress-strain curve of concrete (Hsu 1993)

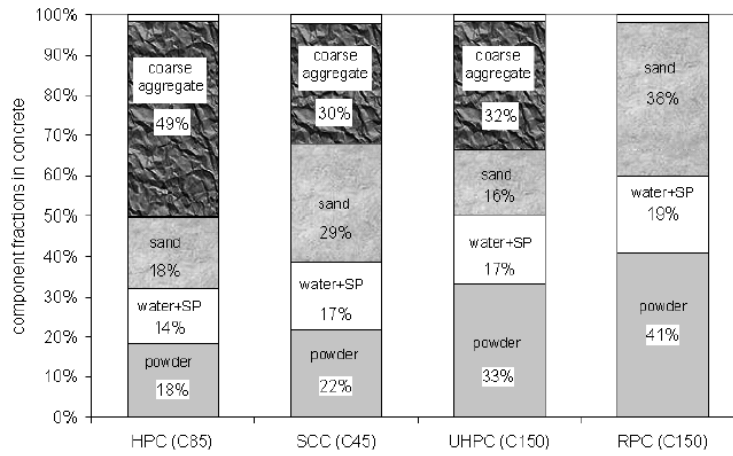


Figure 2-4. Component volume percentages in HPC, SCC, UHPC and RPC (Ma et al. 2004)

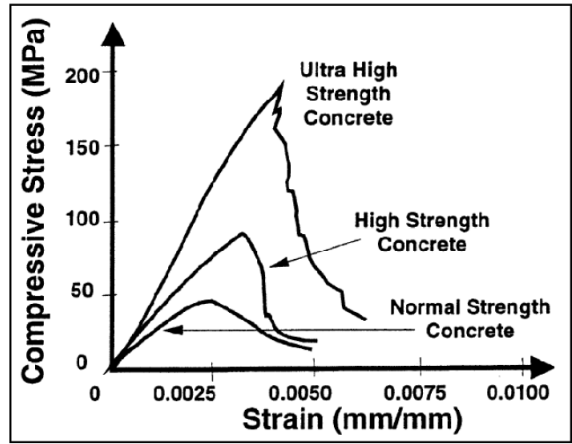


Figure 2-5. Increasing brittleness with strength (Shah and Weiss 1998)

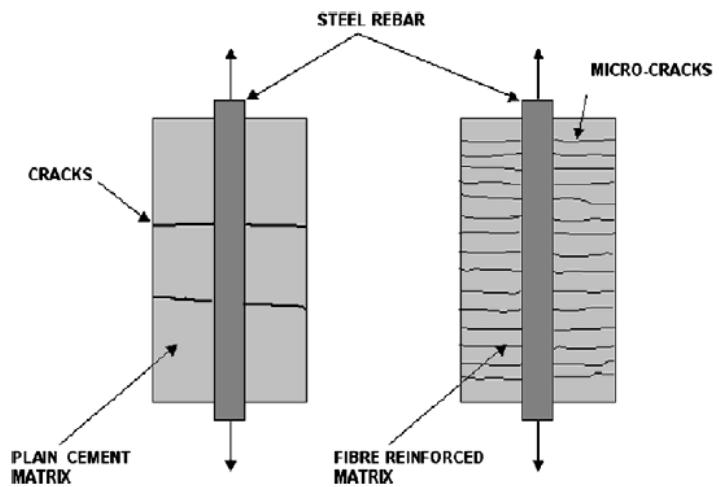


Figure 2-6. Crack pattern in reinforced concrete and fiber reinforced concrete elements subjected to tension (Brandt 2008)

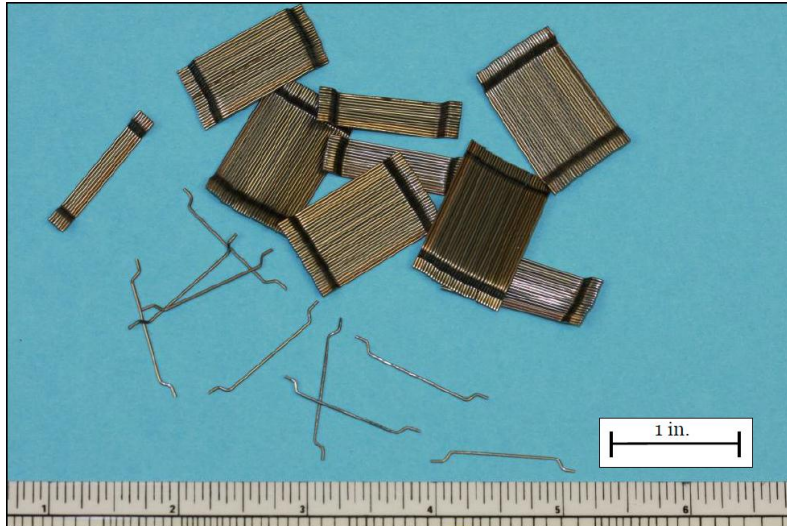


Figure 2-7. Bekaert Dramix® ZP305 fibers used in Cor-Tuf (Williams et al. 2009)

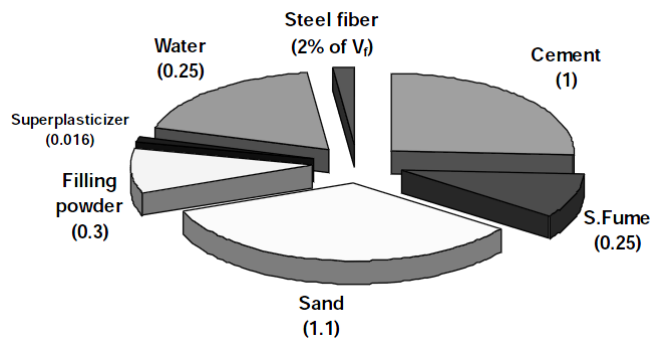


Figure 2-8. Example of optimum mix proportion of UHPC (J. J. Park et al. 2008)

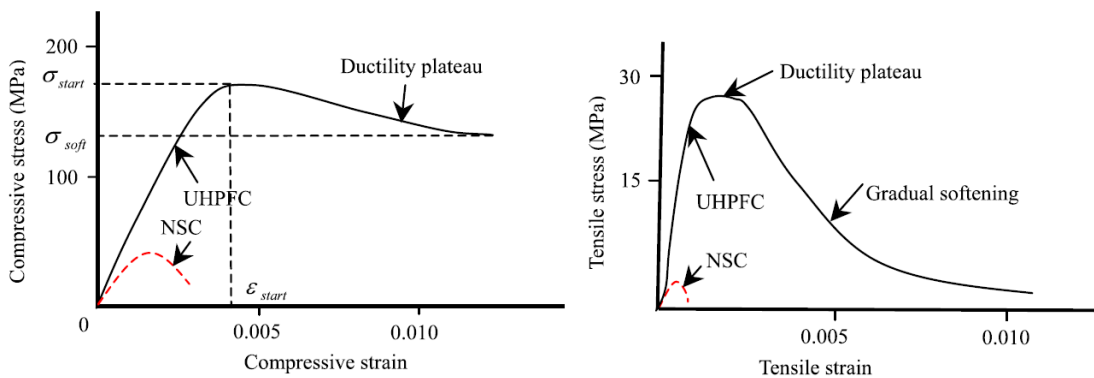


Figure 2-9. Mechanical properties of conventional concrete and UHPFRC (Wu et al. 2009)

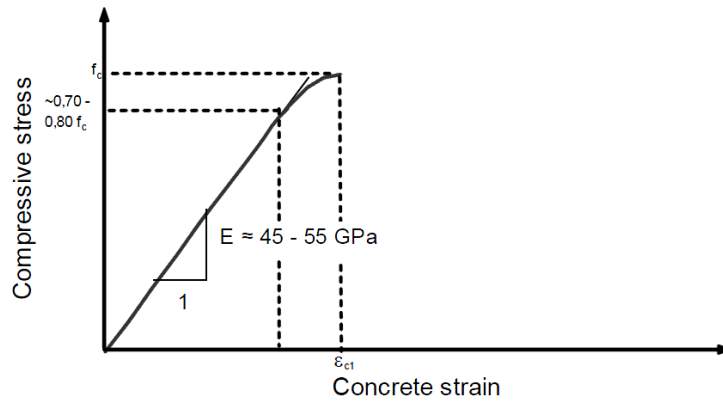


Figure 2-10. Compressive stress-strain diagram of UHPC without fibers (Fehling et al. 2004)

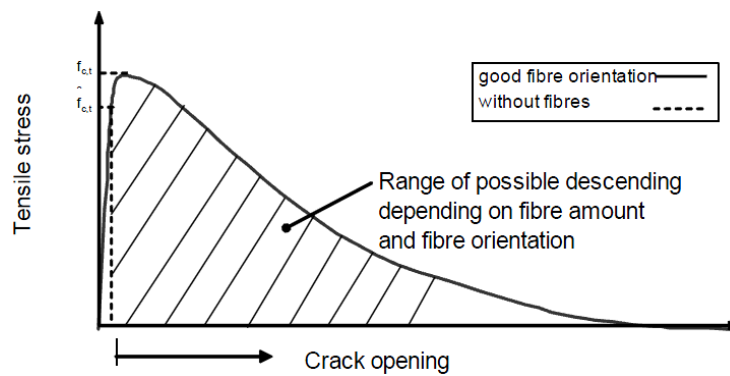


Figure 2-11. UHPFRC stress-crack opening curve (Fehling et al. 2004)

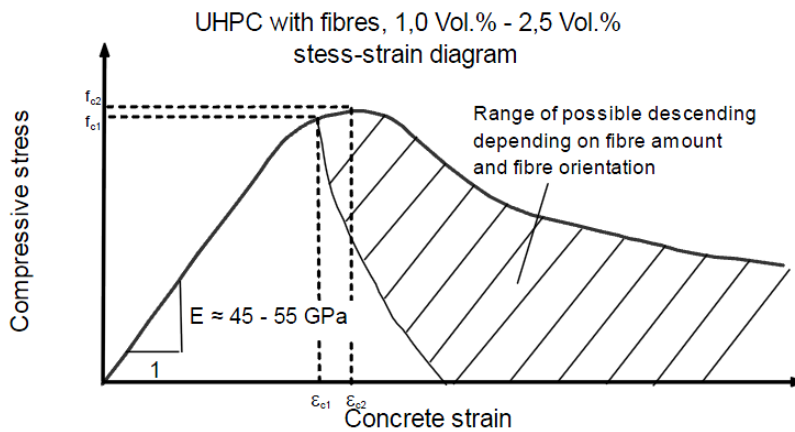


Figure 2-12. Effect of fibers on UHPFRC descending compressive stress-strain curve (Fehling et al. 2004)

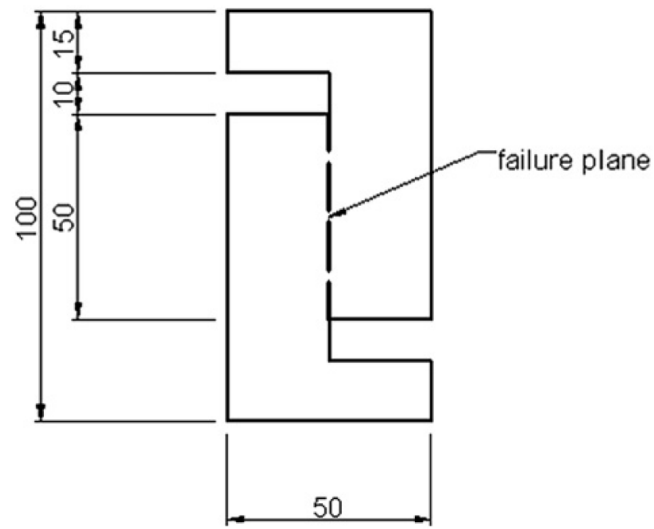


Figure 2-13. Shear specimen dimensions (in mm) (Millard et al. 2010)

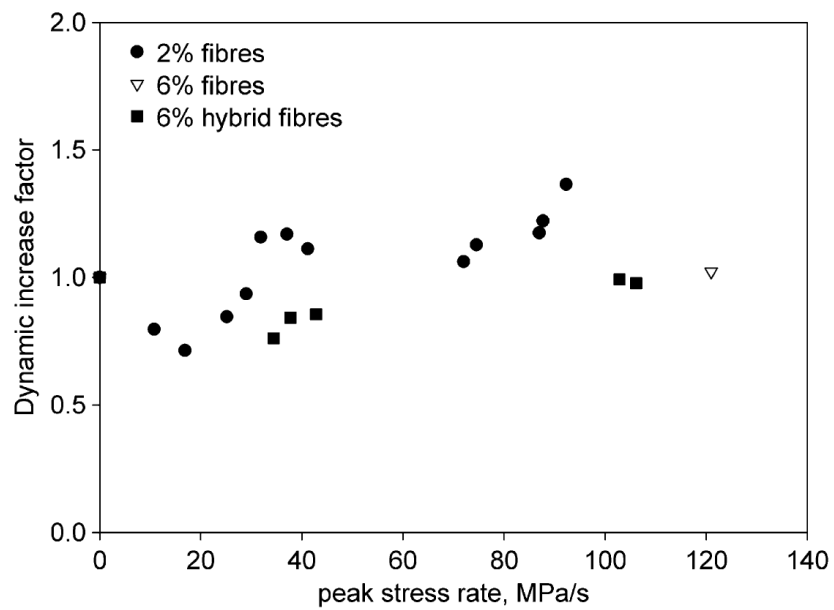


Figure 2-14. Dynamic increase factor versus peak loading rate for shear tests (Millard et al. 2010)

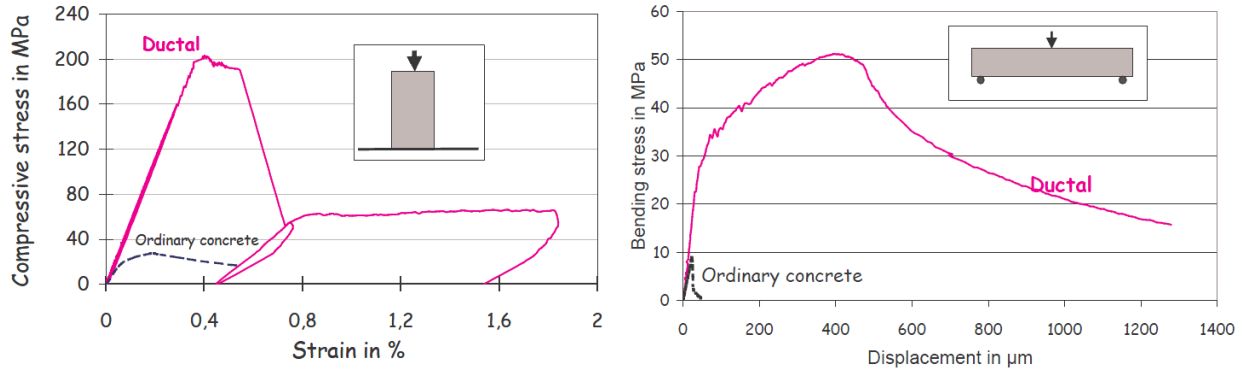


Figure 2-15. Ductal<sup>®</sup> behavior in compression and bending (Acker and Behloul 2004)

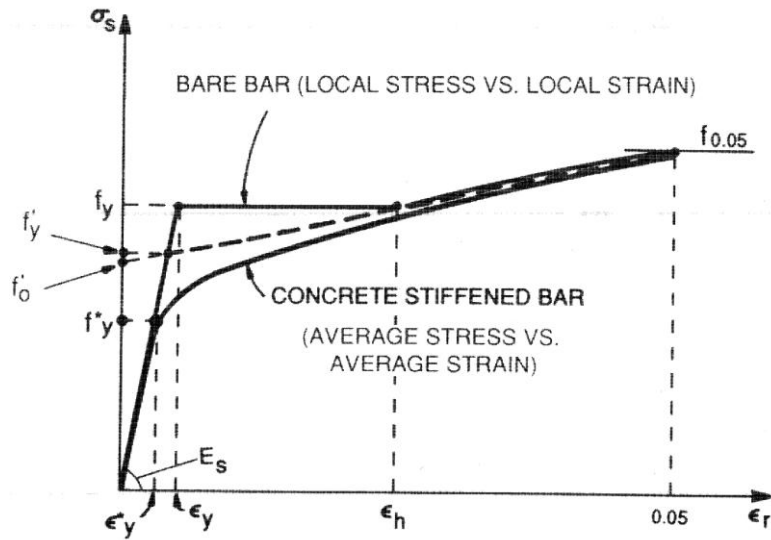


Figure 2-16. Bi-linear stress-strain curve for embedded reinforcement (Hsu 1993)

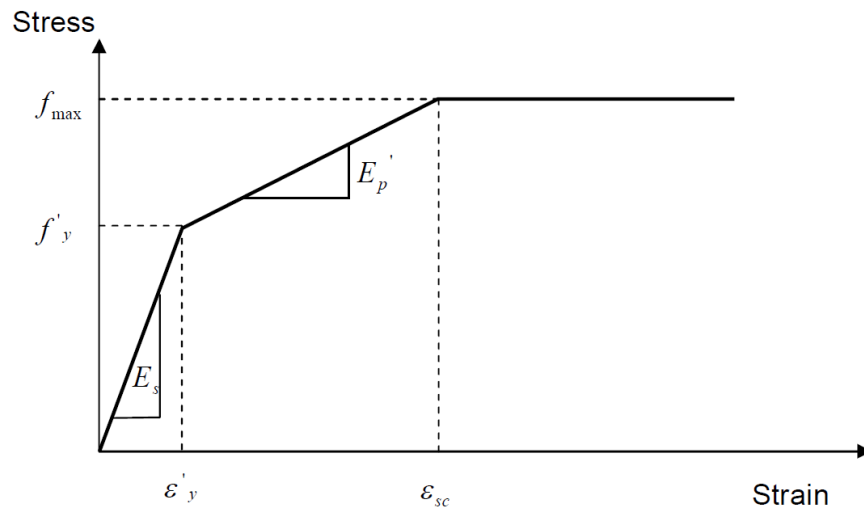


Figure 2-17. Modified Hsu model for steel reinforcement (Y. H. Koh 2011)

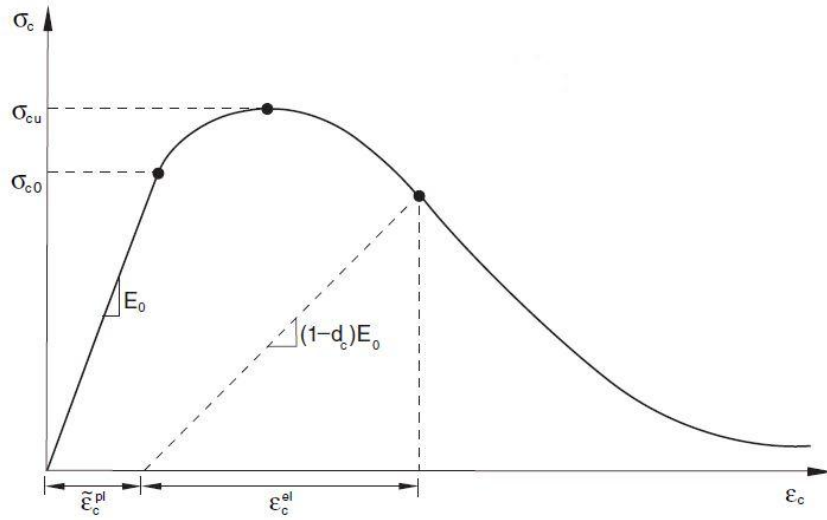


Figure 2-18. Uniaxial compressive stress-strain behavior for CDP material model (Simulia 2011)

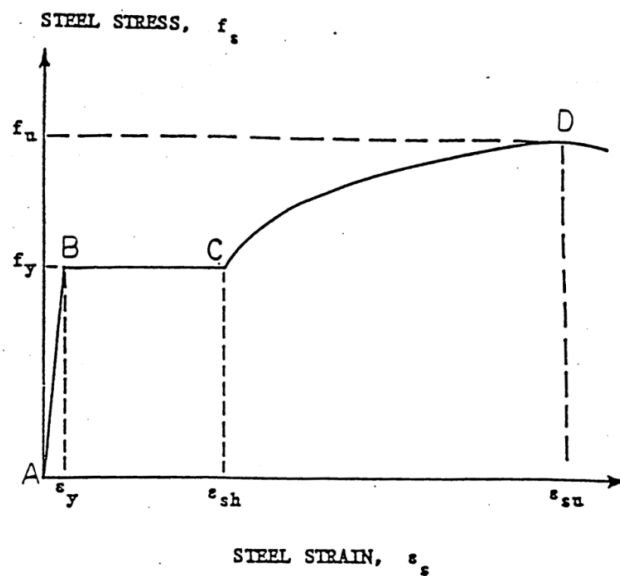


Figure 2-19. Park and Paulay strain-hardening model

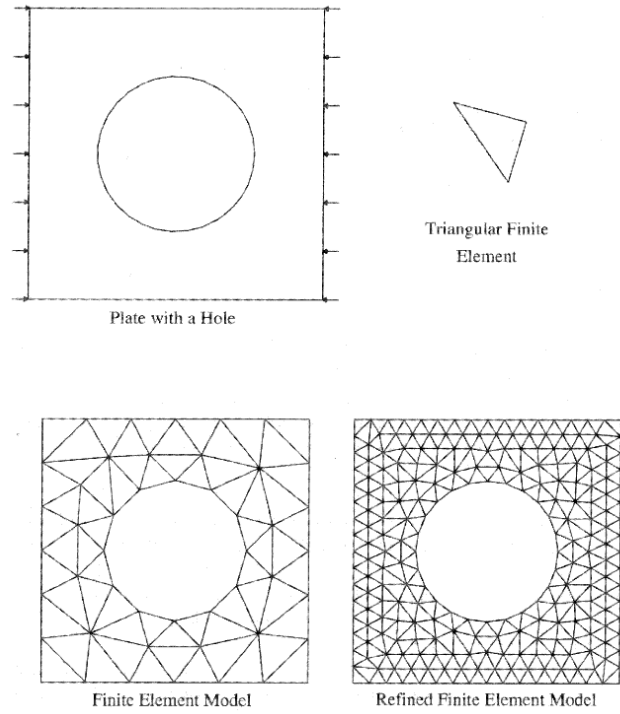


Figure 2-20. Finite Element Mesh (Fish and Belytschko 2007)

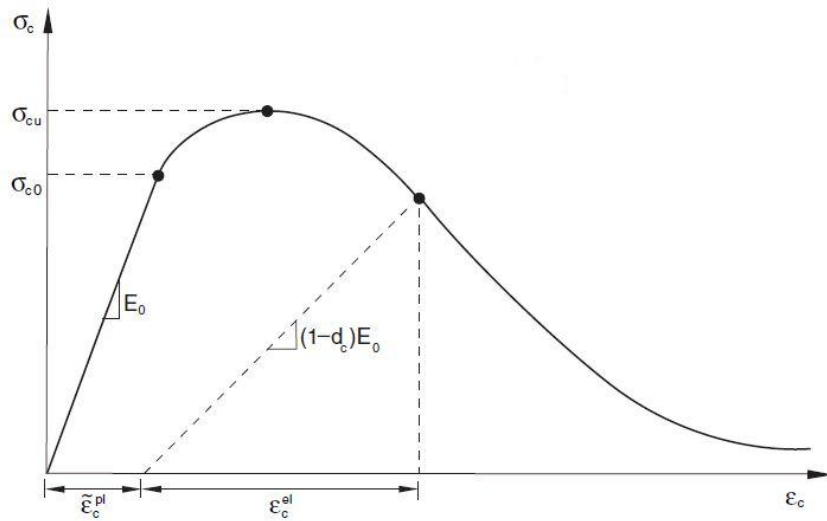


Figure 2-21. Uniaxial compressive stress-strain behavior for CDP material model (Simulia 2011)

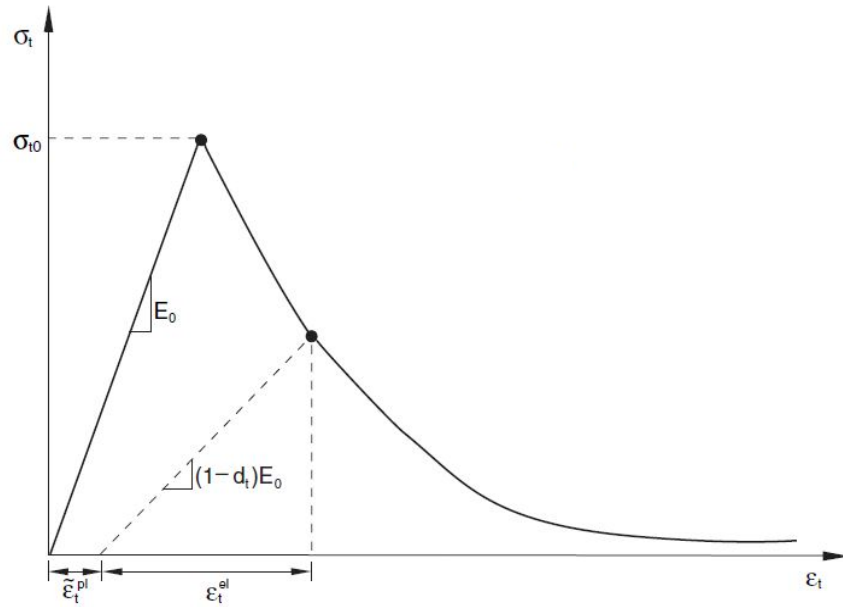


Figure 2-22. Uniaxial tensile stress-strain-curve in CDP material model (Simulia 2011)

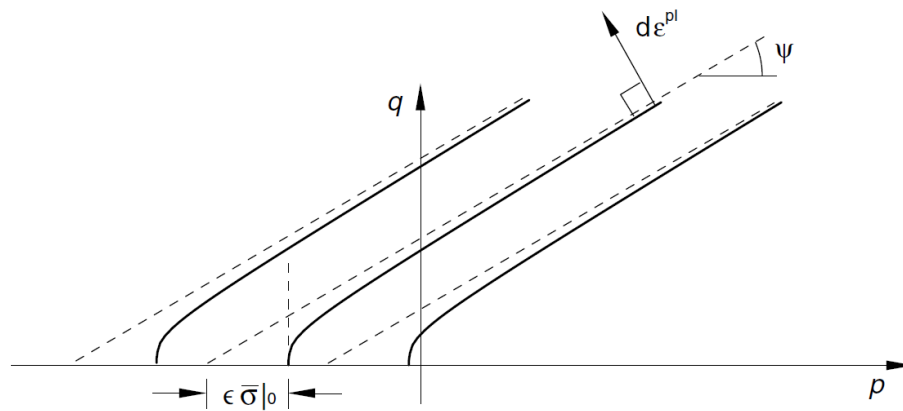


Figure 2-23. Drucker-Prager plastic flow potential (Simulia 2011)

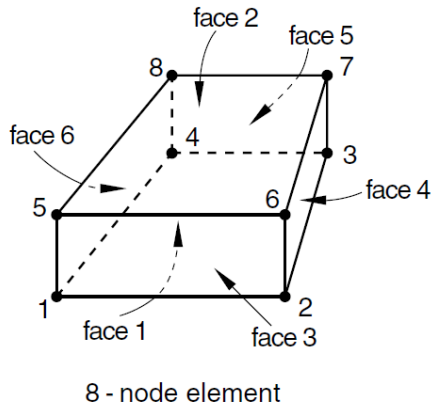


Figure 2-24. 8-node brick element (Simulia 2011)

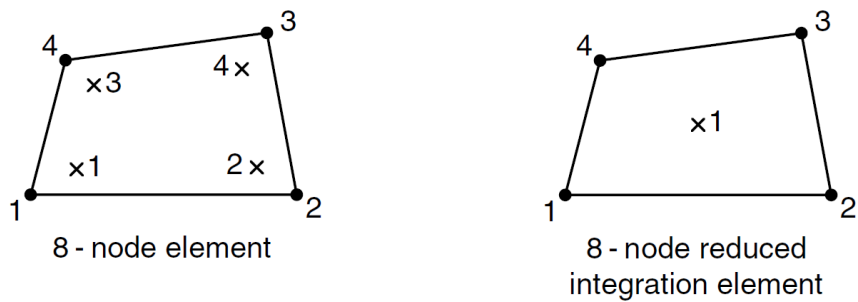


Figure 2-25. Full integration and reduced integration 8-node brick elements (Simulia 2011)

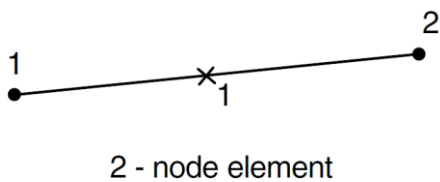


Figure 2-26. 2-node beam element (Simulia 2011)



Figure 2-27. Direct shear failure in RC box top slab (side view) (Slawson 1984)

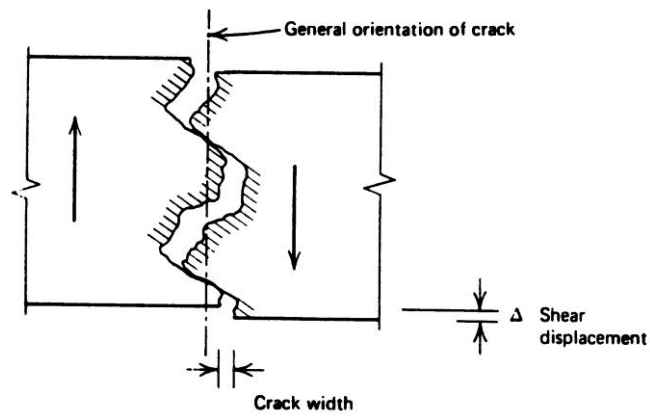


Figure 2-28. Displacement along a cracked shear plane (R. Park and Paulay 1975)

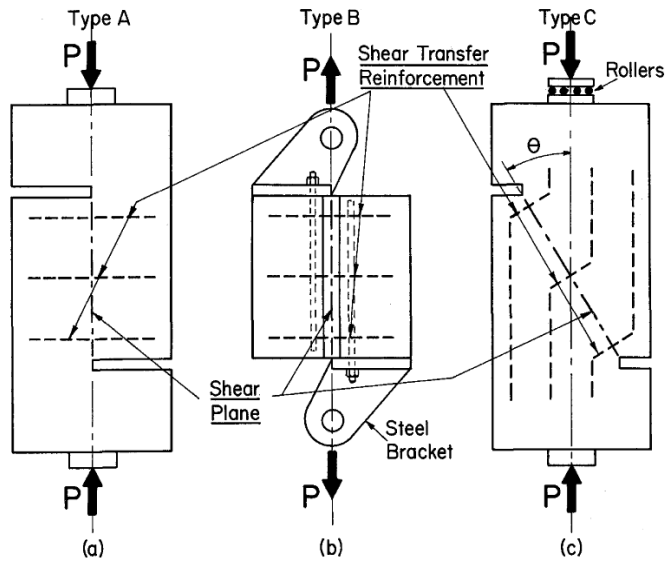


Figure 2-29. Shear transfer test specimens. (a) push-off; (b) pull-off; (c) modified push-off (Mattock and Hawkins 1972)

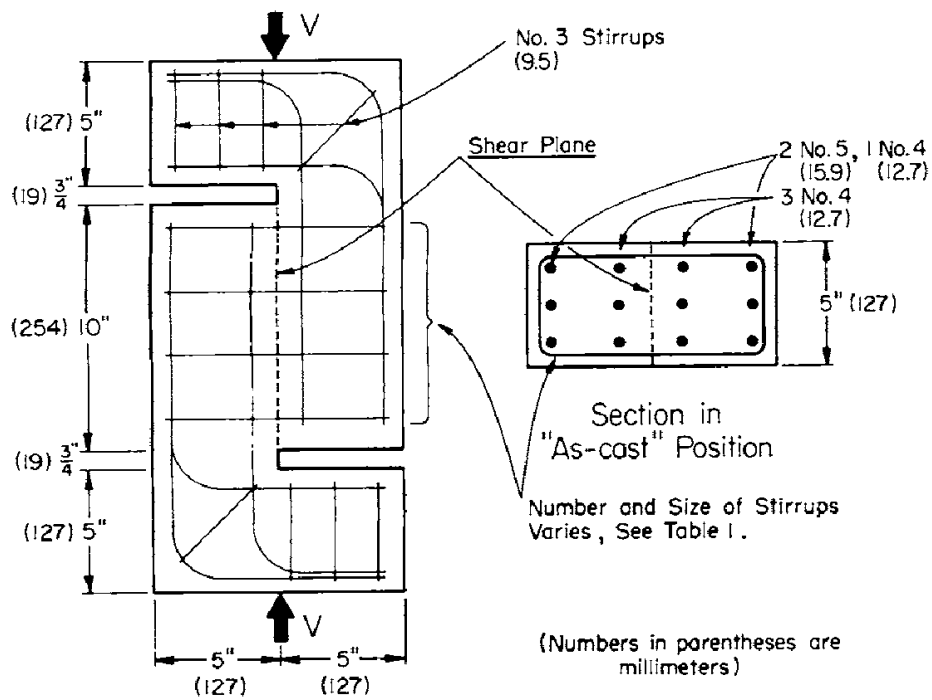


Figure 2-30. Push-off specimen details (Hofbeck et al. 1969)

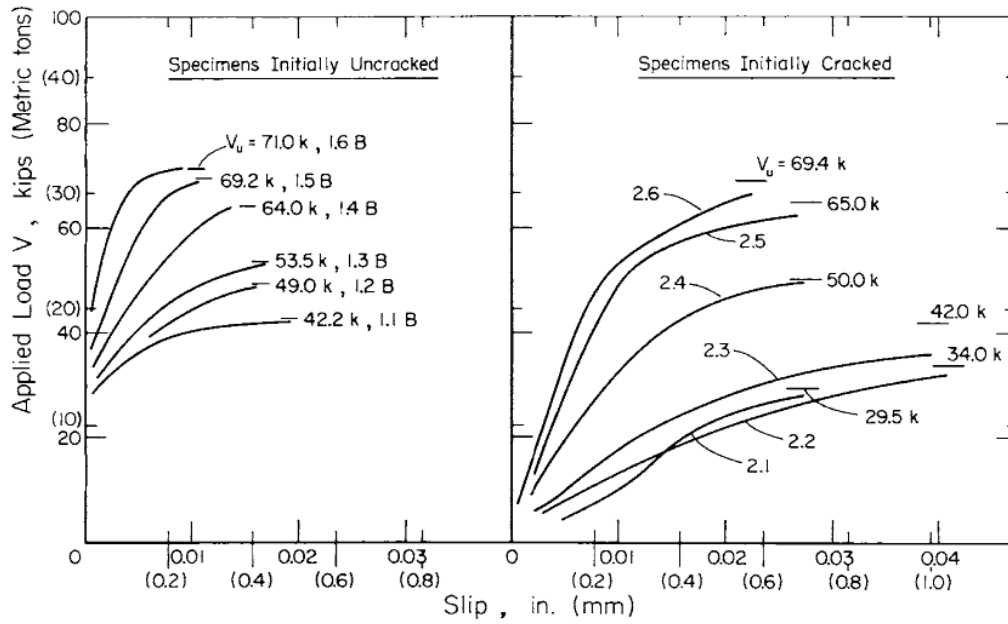


Figure 2-31. Typical load-slip curves (Hofbeck et al. 1969)

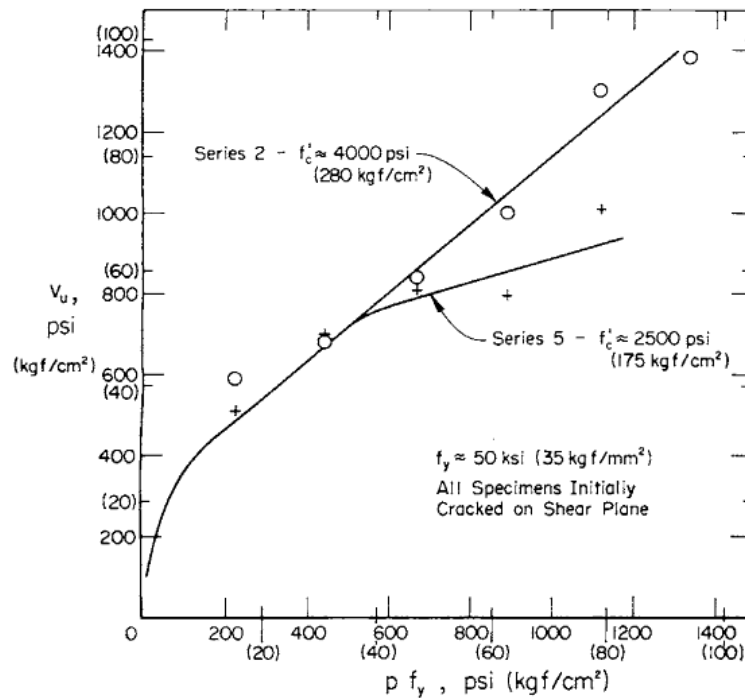


Figure 2-32. Effect of concrete strength on shear strength of initially cracked specimens (Hofbeck et al. 1969)

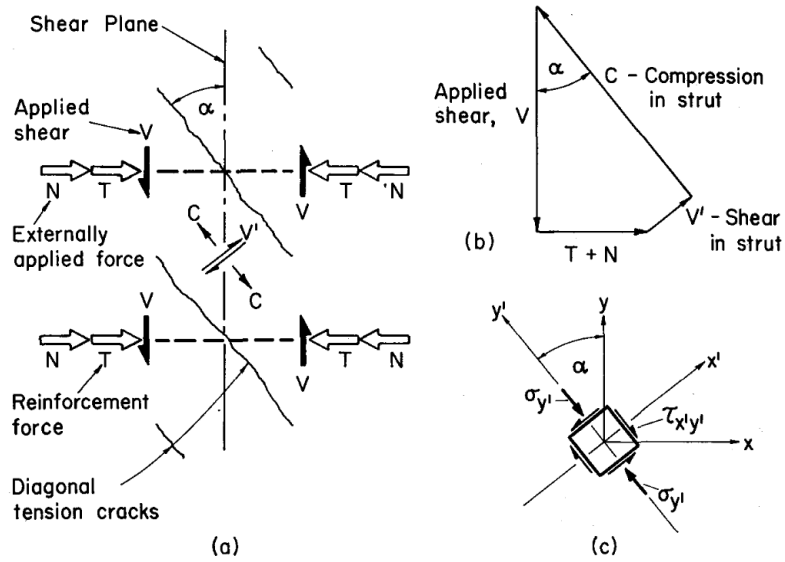


Figure 2-33. Shear transfer in initially uncracked concrete (Mattock and Hawkins 1972)

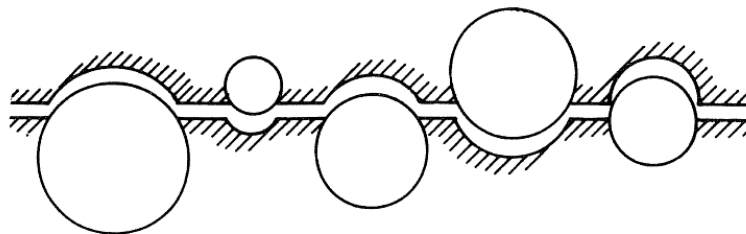


Figure 2-34. Structure of a crack plane (Walraven and Reinhardt 1981)

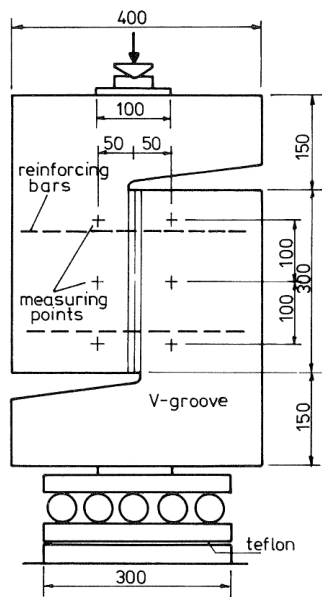


Figure 2-35. Push-off specimen geometry (in mm) (Walraven and Reinhardt 1981)

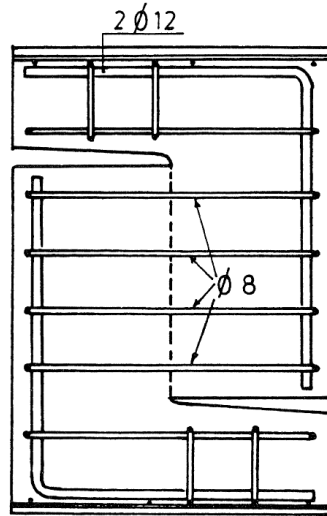


Figure 2-36. Stirrups and additional reinforcement (Walraven and Reinhardt 1981)

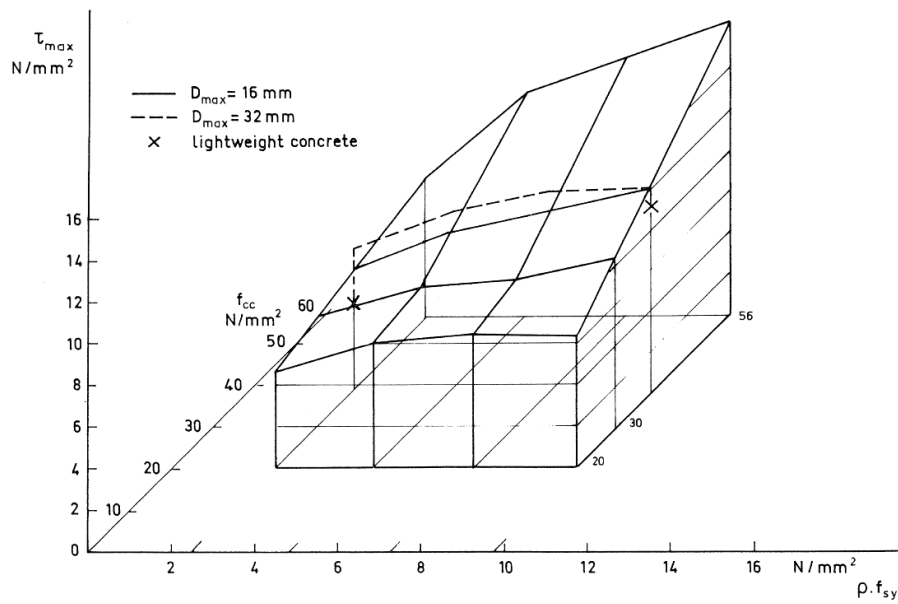


Figure 2-37. Maximum shear stresses as a function of concrete compressive strengths,  $f_{cc}$ , and mechanical reinforcement ratio,  $\rho f_{sy}$  (Walraven and Reinhardt 1981)

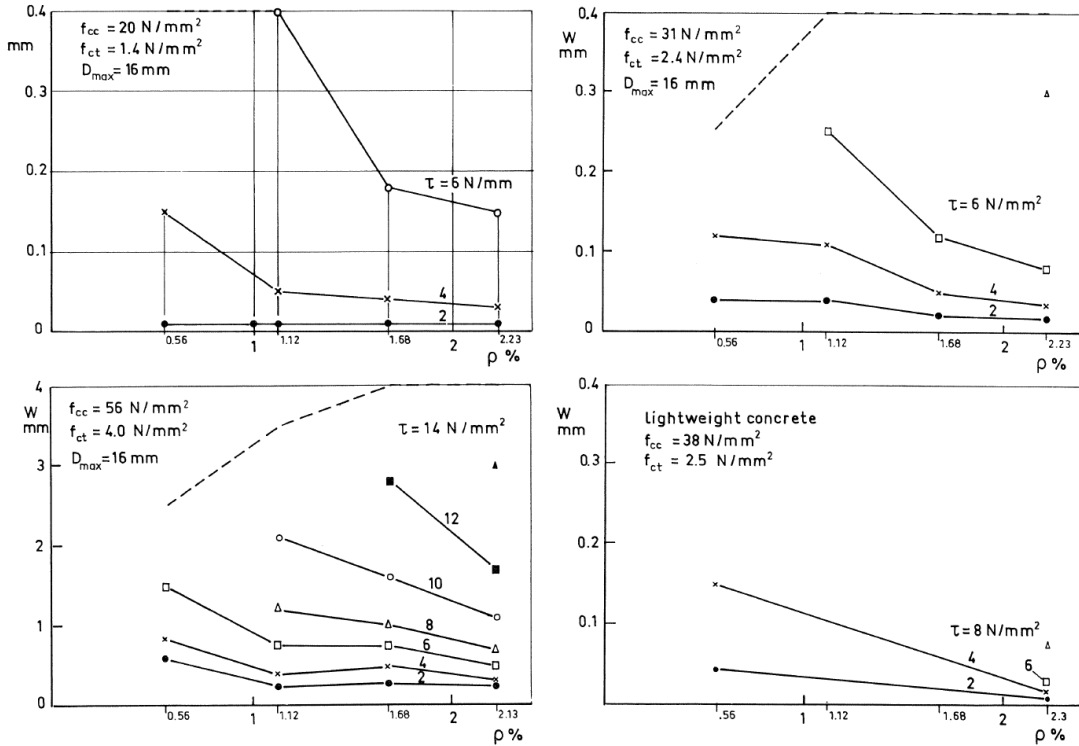


Figure 2-38. Crack opening under a certain shear stress,  $\tau$ , as a function of the reinforcement ratio,  $\rho$  (Walraven and Reinhardt 1981)

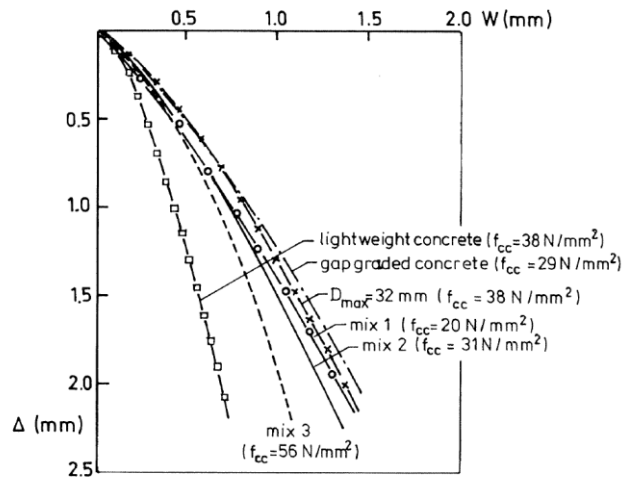


Figure 2-39. Average crack opening paths (Walraven and Reinhardt 1981)

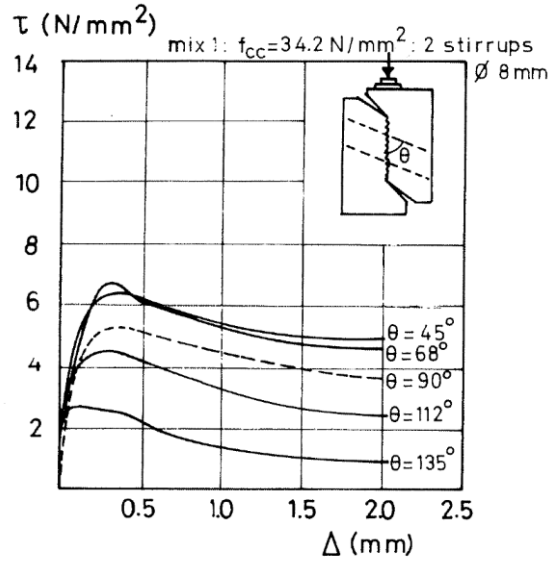


Figure 2-40. Shear stress-shear displacement at various angles of inclination,  $\theta$  (Walraven and Reinhardt 1981)

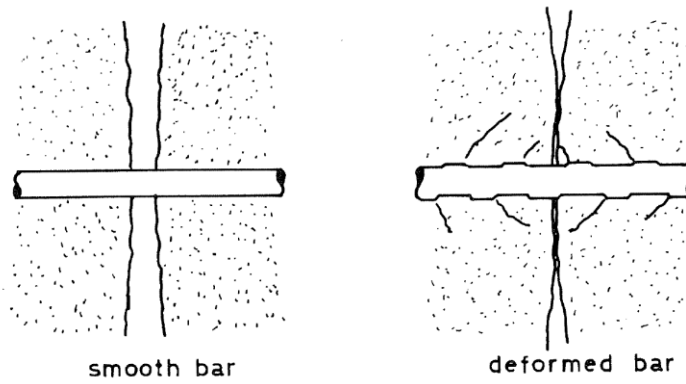


Figure 2-41. Crack opening for smooth and deformed bars (Walraven and Reinhardt 1981)

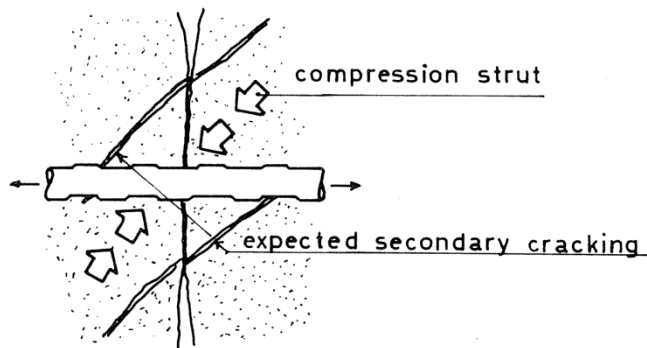


Figure 2-42. Expected additional cracking for shear loading with deformed bars (Walraven and Reinhardt 1981)

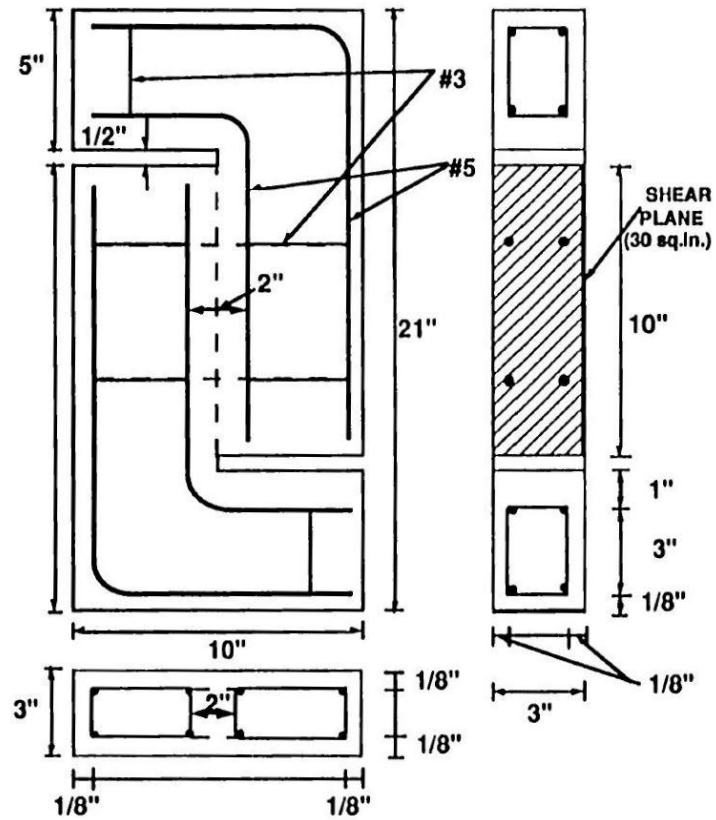


Figure 2-43. Push-off specimen geometry (1 in. = 25.4 mm) (Valle and Buyukozturk 1993)

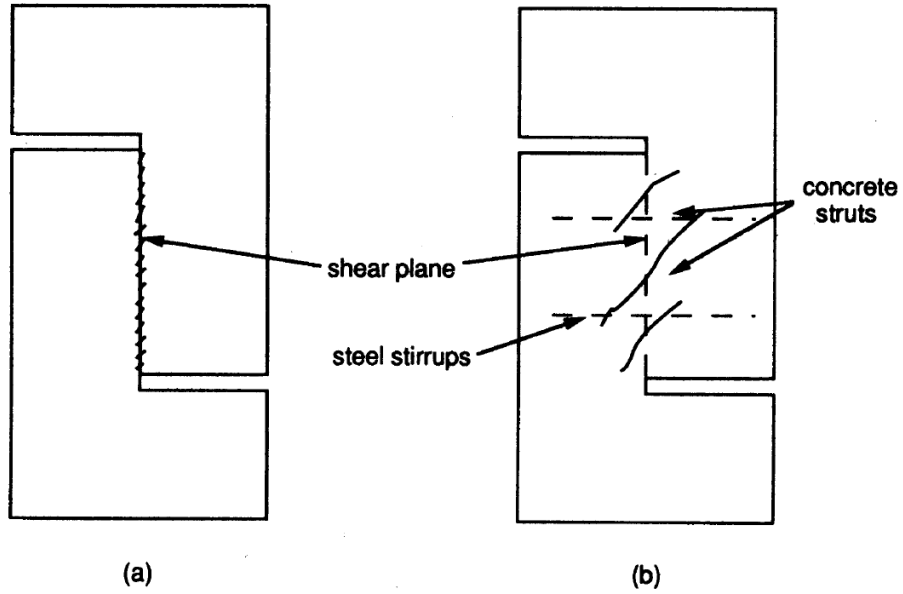


Figure 2-44. Cracking patterns for push-off specimens. (a) no stirrups crossing the shear plane. (b) stirrups crossing the shear plane (Valle and Buyukozturk 1993)

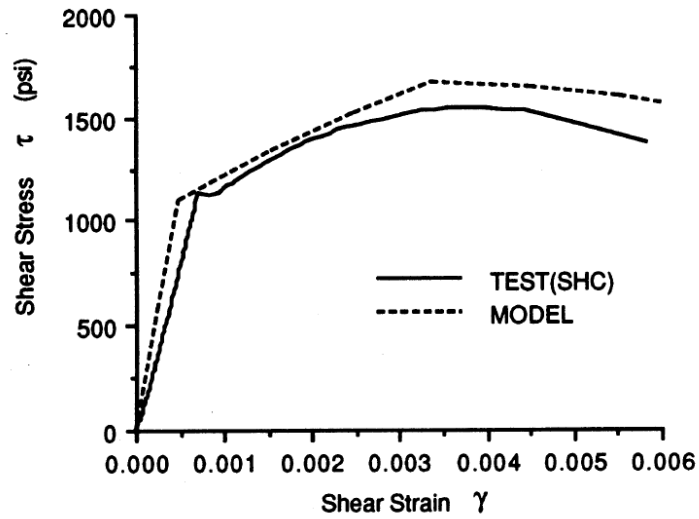


Figure 2-45. Shear stress versus shear strain for SHC (Valle and Buyukozturk 1993)

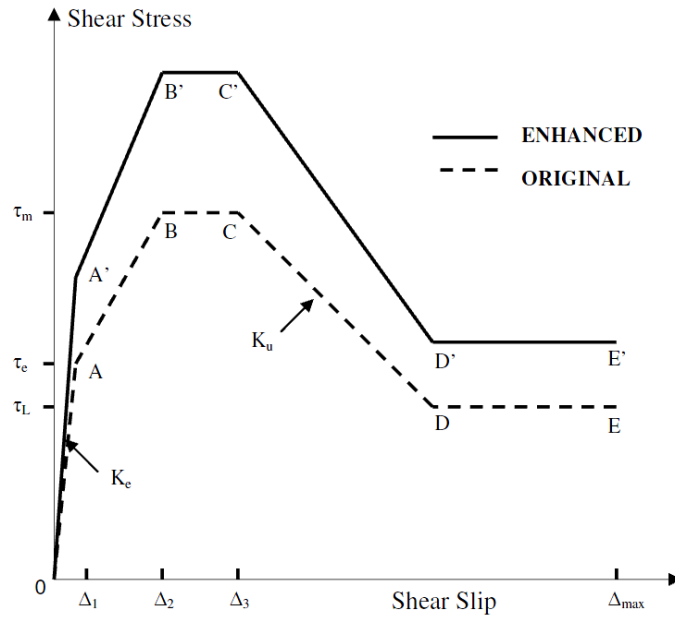


Figure 2-46. Original and modified shear stress-slip relationship for direct shear (T. Krauthammer et al. 1986)

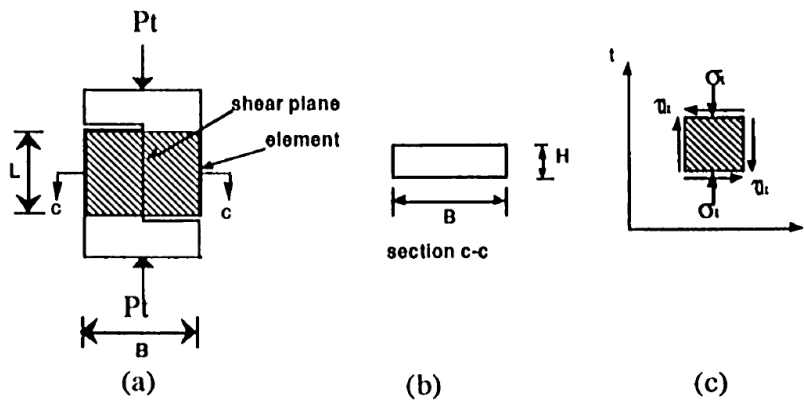


Figure 2-47. Shear transfer problem. (a) element considered (b) cross-section, and (c) stress state of element at shear plane (Valle and Buyukozturk 1993)

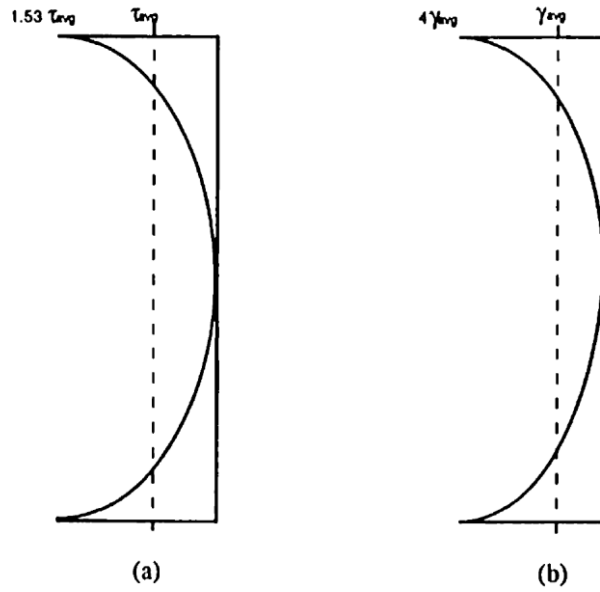


Figure 2-48. Before cracking (a) shear stress distribution and (b) shear strain distribution (Valle and Buyukozturk 1993)

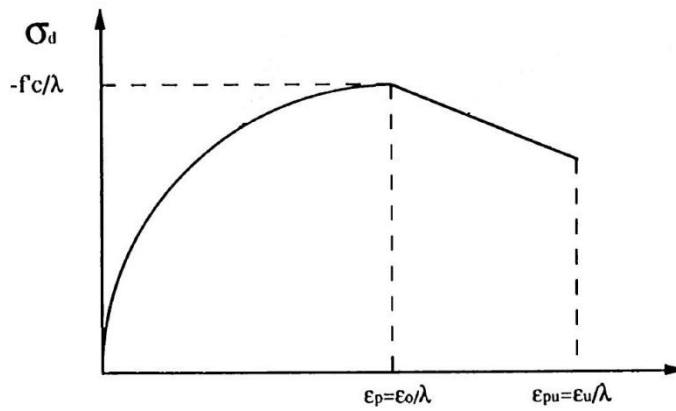


Figure 2-49. Idealized stress-strain curve for concrete in compression (Valle and Buyukozturk 1993)

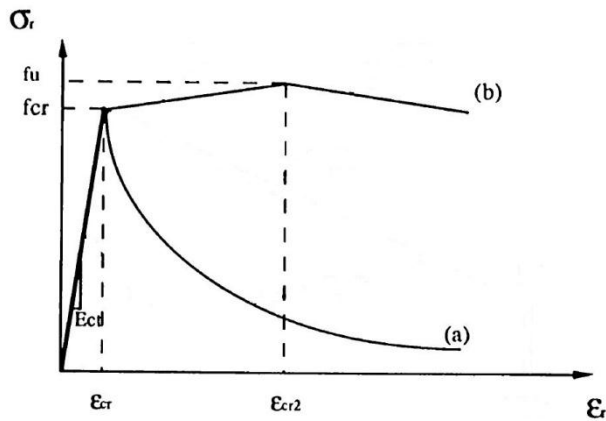


Figure 2-50. Idealized tension stress-strain curve for (a) plain concrete and (b) steel fiber reinforced concrete (Valle and Buyukozturk 1993)

Table 2-1. Quasi-static uniaxial compressive performance of UHPCC at 60 days (Rong et al. 2010)

Number	Compressive strength (MPa)	Peak value of strain ( $\times 10^{-3}$ )	Elastic modulus (GPa)	Toughness index		
				$\eta_{c5}$	$\eta_{c10}$	$\eta_{c30}$
UHPCC( $V_0$ )	143	2.817	54.7	2.43	2.43	2.43
UHPCC( $V_3$ )	186	3.857	57.3	3.59	5.08	5.57
UHPCC( $V_4$ )	204	4.165	57.9	4.57	6.32	7.39

Table 2-2. Compressive strength of 3 in x 6 in UHPC cylinders (Sayed 2004)

Curing Method	Compressive Strength (ksi)
Steam	28.0
Ambient Air	18.0
Tempered Steam	25.2
Delayed Steam	24.9

Table 2-3. Formulation of Ductal® (Lafarge n.d.)

Formulation	(kg/m <sup>3</sup> )
Cement	710
Silica fume	230
Ground quartz	210
Sand	1020
Water	140
Superplasticizer	13
Steel fibers	160

Table 2-4. Formulation of CEMTEC<sub>multiscale</sub> (kg/m<sup>3</sup>) (Rossi et al. 2005)

Material	Amount
Cement	1050.1
Silica Fume	268.1
Sand	514.3
Water	180.3
Superplasticizer	44
Steel Fibers	858
Water/cement	0.201
Water/binder	0.160
Air entrained	20.1

Table 2-5. Cor-Tuf mixture composition (Williams et al. 2009)

Material	Product	Proportion by Weight
Cement	Lafarge, Class H, Joppa, MO	1.00
Sand	US Silica, F55, Ottawa, IL	0.967
Silica flour	US Silica, Sil-co-Sil 75, Berkeley Springs, WV	0.277
Silica fume	Elkem, ES 900 W	0.389
Superplasticizer	W.R. Grace, ADVA 170	0.0171
Water (tap)	Vicksburg, MS Municipal Water	0.208
Steel Fibers <sup>1</sup>	Bekaert, Dramix ® ZP305	0.31

<sup>1</sup> Steel fibers used in Cor-Tuf1 material only

Table 2-6. Unconfined compressive strengths for Cor-Tuf cylinders (Williams et al. 2009)

Cor-Tuf1 UC Strength, Mpa			Cor-Tuf 2 UC Strength, Mpa
75-by 150-mm Cylinder	100-by 200-mm Cylinder	75-by 150-mm Cylinder Without Steel Fibers	75-by 100-mm Cylinder
237	216	216	228
231	219	208	225
243	226	206	209
233	228		190
238	229		225
244			209

Table 2-7. Test specimen classification by type of concrete and shear reinforcement (Valle and Buyukozturk 1993)

Specimen Identification	Concrete Type	Vol. fraction steel fibers	Vol. fraction polypropylene	Steel stirrup reinforcing ratio
-------------------------	---------------	----------------------------	-----------------------------	---------------------------------

		$V_{sf}\%$	fibers $V_{pf}\%$	$\rho$
NC	NC	-	-	-
SNC	SNC	1.0%	-	-
PNC	PNC	-	1.0%	-
NCS	NC	-	-	1.47%
SNCS	SNC	1.0%	-	1.47%
PNCS	PNC	-	1.0%	1.47%
HC	HC	-	-	-
SHC	SHC	1.0%	-	-
PHC	PHC	-	1.0%	-
HCS	HC	-	-	1.47%
SHCS	SHC	1.0%	-	1.47%
PHCS	PHC	-	1.0%	1.47%

Table 2-8. Results for normal strength concrete specimens (Valle and Buyukozturk 1993)

Specimen	$f'_c$ (psi)	Max. load, $P_t$ (lbs)	$\tau_{max}$	$\frac{\tau_{max}}{\sqrt{f'_c}}$	% incr. avg. $\tau_{max}$	$\tau_{cr}$
NC-1	4,500	23,251.8	775.06	11.55	-	775.06
NC-2	4,500	22,323.9	744.13	11.09		744.13
SNC-1	4,200	30,303.0	1,010.10	15.60	36.00	618.26
SNC-2	4,200	29,552.1	985.07	15.20		593.44
PNC-1	4,010	23,651.7	788.39	12.45	9.76	788.39
PNC-2	4,010	23,556.6	785.22	12.40		785.22
NCS-1	4,950	39,258.9	1,308.63	18.60	62.10	823.87
NCS-2	4,950	38,203.5	1,273.45	18.10		805.58
SNCS-1	3,800	36,024.9	1,200.83	19.48	68.20	669.46
SNCS-2	3,800	34,397.4	1,146.58	18.60		621.99
PNCS-1	4,900	38,535.0	1,284.50	18.35	62.32	747.60

PNCS-2	4,900	38,640.0	1,288.00	18.40	755.30
--------	-------	----------	----------	-------	--------

Table 2-9. Results for high-strength concrete specimens (Valle and Buyukozturk 1993)

Specimen	$f'_c$ (psi)	Max. load, $P_t$ (lbs)	$\tau_{max}$	$\frac{\tau_{max}}{\sqrt{f'_c}}$	% incr. avg. $\tau_{max}$	$\tau_{cr}$
HC-1	9,000	24,843.3	828.11	8.73		827.90
HC-2	9,000	26,927.1	897.57	9.16		869.07
SHC-1	11,600	45,493.8	1,516.46	14.08	58.58	1,151.35
SHC-2	11,600	46,172.4	1,539.08	14.29		1,129.81
PHC-1	9,100	29,763.0	992.10	10.40	17.16	884.30
PHC-2	9,100	30,220.8	1,007.36	10.56		903.38
HCS-1	9,680	52,155.0	1,738.50	17.67	112.69	1,024.21
HCS-2	9,680	60,153.9	2,005.13	20.38		1,054.71
SHCS-1	10,930	67,557.9	2,251.93	21.54	139.68	1,259.79
SHCS-2	10,930	66,930.9	2,231.03	21.34		1,323.55
PHCS-1	9,020	49,377.0	1,645.90	17.33	92.45	1,009.57
PHCS-2	9,020	48,721.5	1,624.05	17.10		1,001.67

Table 2-10. Peak and ultimate strains used for different types of concrete (Valle and Buyukozturk 1993)

Concrete type	Peak strain ( $\epsilon_0$ )	Ultimate strain ( $\epsilon_u$ )
NC	0.0020	0.0035
SNC	0.0035	0.0050
HC	0.0025	0.0030
SHC	0.0030	0.0045

## CHAPTER 3 RESEARCH APPROACH AND METHODS

The emphasis of this study is to implement a continuum based FE model to simulate the direct shear behavior of push-off specimens subjected to quasi-static loading. The numerical simulations will be conducted using Abaqus v. 6.11. Validation of the model must be accomplished in order to give confidence that the model can produce reasonably accurate results. The validation of the push-off model is necessary to gain the confidence needed to make pre-test predications for a future study.

In order to attain an understanding of the behavior of UHPC and UHPFRC under direct shear, a finite element analysis of normal strength concrete push-off specimens were conducted. These were chosen as there is experimental research available to validate the model to gain confidence in the numerical solution. Accurately modeling the direct shear behavior of NSC was a challenging task. No such effort has been reported in the literature. This coupled with the added complexity introduced by using a material model for UHPC led the work to focus on validating the numerical model for normal strength concrete only using test results from Valle and Buyukozturk (1993). The focus of the finite element work was based on the Valle and Buyukozturk tests performed on normal strength concrete ( $f'_c = 4,500-4,950$  psi).

This study will attempt to capture this behavior numerically in order to predict behavior for future experimental studies and to be the starting point for numerically assessing shear blocks with the UHPC Cor-Tuf as the concrete material.

### **Model Validation**

Model validation is based on the specimens tested by Valle and Buyukozturk in 1993. While the emphasis of their research was on shear strength and ductility

improvements achieved by the addition of steel and polypropylene fibers in the concrete mix, they also performed test with plain and reinforced push-off specimens under direct shear. The focus in this study will only be on the normal strength push-off specimens. These experiments were chosen due to the shear stress-shear slip data that was recorded. This section will lay out the specifics of the specimens that were tested which were used in this study for the numerical assessment of capturing this shear stress-shear slip behavior through the finite element code Abaqus.

Although some of this material was covered in Chapter 2, it is best to include a full investigation on the normal strength concrete specimens which will be used for validation in this study.

### **Specimen Geometry and Materials**

The direct shear transfer behavior of initially uncracked push-off specimens were conducted. The dimensions of the specimens were 21 x 10 x 3 in. (533 x 254 x 76 mm), and had a shear plane area of 30 in.<sup>2</sup> (19,335 mm<sup>2</sup>) as shown in Figure 3-1. They based this geometry on previous research by the authors. Nomenclature for the specimens are as follows; normal strength concrete with no shear plane reinforcement (NC) and normal strength concrete with shear plane reinforcement (NCS). Two specimens of both NC and NCS were tested.

All specimens contained reinforcement in the form of L-shaped #5 deformed bars in order to avoid any local failures and to force the specimen to fail along the shear plane. In addition to the vertical bars, specimens with reinforcing crossing the shear plane (NCS), two closed steel stirrups made with #3 deformed bars were placed ( $\rho = 1.47\%$ ). This is shown in Figure 3-2. Exact placement of the shear plane closed stirrups was not reported.

The test specimens used the following materials. type 1 portland cement, pea gravel with maximum aggregate size of 3/8", mortar sand, superplasticizers, water, and mild steel deformed bars (#3 and #5) with a yield strength of 60 ksi. Mixing proportions for the normal strength concrete are show in Table 3-1. It was designed to develop a 4,000 psi compressive strength at 7 days. Each specimen type, NC and NCS, where mixed in a separate batch.

### Test Setup

The specimens were placed in an MTS machine loading frame and tested in a stroke-controlled configuration with a displacement rate of 1/19,000 in./sec (1/750 mm/sec). In order to measure the horizontal and vertical displacements at the shear plane, LVDTs were attached to the front face of the specimen. The position of the LVDTs and the loading configuration are shown in Figure 3-3 while the specimens in the MTS loading frame are shown in Figure 3-4.

### Results

Compression and splitting tension tests were performed on 3 x 6 in. cylinders at the time of testing for both NC and NCS mixes. Compressive strengths ( $f'_c$ ) and splitting tensile strengths ( $f'_{sp}$ ) are summarized in Table 3-2. Results from the direct shear tests are also summarized in Table 3-2 for both NC and NCS specimens. Reported shear stress was obtained by dividing the applied load by the area of the shear plane (30 in.<sup>2</sup>). The table includes both the maximum shear stress,  $\tau_{max}$ , and their normalized values with respect to  $\sqrt{f'_c}$ , are reported. This will effectively eliminate the varying material strength between the two mixes. The shear stress at first cracking,  $\tau_{cr}$ , is also reported. The authors use the horizontal displacement to measure crack width. The horizontal

displacement measurements are approximately zero up to cracking. The NC specimens fail with no horizontal displacement, leading to the assumption of the first crack developing and the NC specimen failing with no reinforcement to take over. The NCS specimens cracking shear stress were then determined when the horizontal displacement started. Figure 3-5 and Figure 3-6 show the vertical and horizontal deflections for one of the NC specimens while Figure 3-7 and Figure 3-8 show the vertical and horizontal displacement for one of the NCS specimens. These plots are representative of the behavior of both specimens of both the NC and NCS sets. Although only two tests per specimen were completed, very consistent results were obtained giving confidence in correct results.

The shear stress vs. vertical displacement for the NC specimens (Figure 3-5) was linear up to failure, which is also the point of first cracking. Since no shear plane reinforcement was provided, the specimens failed immediately after the first crack developed. The shear stress vs. vertical displacement behavior for the NCS specimens (Figure 3-7) was linear up to first cracking. After first cracking, the steel reinforcement allows the specimen to carry higher loads of roughly 60% over the NC specimens. After the peak load was reached, a softening behavior can be seen. Once the concrete fails, an unloading type of behavior can be seen. This is attributed to the failure mode of the NCS specimens and will be discussed later in this section.

### **Failure Modes**

The NC and NCS specimens exhibited two distinct failure modes which will be discussed and can be seen in Figure 3-9. For the NC specimens with no shear plane reinforcement, inclined cracks along the shear plane developed and failure occurred when these cracks developed into one cohesive crack band along the shear plane

which can be seen in Figure 3-10. In the case of the NCS specimens with shear plane reinforcement, cracks formed inclined to the shear plane and extended to develop well defined compressive struts in shear plane which can be seen in Figure 3-11. The stirrups developed tensile forces which created a truss action. Ultimate failure occurred when the concrete struts failed by crushing.

After failure, the unloading phase in the NCS specimens is explained by the relaxation of the stirrups once the concrete compression struts crushed. This explains why the NCS specimen vertical displacement returns to zero at the end of loading. This theory leads to the assumption that the stirrups did not reach their yield strength and thus no permanent vertical deformation was recorded.

### **Evolution of the FE model**

This section attempts to describe the evolution of the FE model up to the point of the final model used for the results. Many evolutions took place in this process that led to the decisions of analysis type, element type, boundary conditions, loading conditions, etc. These will briefly be discussed to get a sense of the progression of the model up until the final model used in the results section. This is not a comprehensive list of all various models used over the course of the study, just a brief synopsis in order to describe the difficulty in accurately capturing this behavior in Abaqus that was encountered.

Early models attempted to use Abaqus/Standard to run the models using both force controlled loading, based on the maximum recorded force from the tests, and displacement controlled loading, using a parametric study to determine the displacement of the top surface that would be enough to get past the ultimate strength

of the specimen. Both methods gave the same results up to the first non-linear behavior where the force controlled model would fail. This is common in finite element codes.

Modeling of the support conditions of the MTS loading device proved to be problematic. Early models attempted to use support conditions accurate to the experimental work by including steel plate at the base and loading surface of the specimen. This involved specifying contact conditions which led to convergence issues during the analysis. Since issues arose from including these and our interest was only on the behavior of the shear plane, it was decided to not include the steel plates in further analyses.

### **Defining the FE model**

This section will describe the various parameters used in modeling the push-off specimens in Abaqus. Push-off specimens from the Valle experiments are used in this study. The push-off specimen with no reinforcement crossing the shear plane will be referred to as NC while the specimen with reinforcement in the form of #3 closed stirrups ( $\rho = 1.47\%$ ) will be referred to as NCS. This notation is carried over from their investigation.

### **Material Models**

This section will describe the material models used for both the concrete and steel reinforcement in the models.

#### **Concrete material model**

The CDP material model in Abaqus was used to describe the concrete in the models. Stress-strain data was calculated using the modified Hognestad formulation for compressive behavior and Hsu tension model for concrete in tension. These concrete models have been tested and used extensively in the past with great accuracy. Included

in the material formulations where linear damage functions for both compression and tension. Since the push-off specimens utilized two separate compressive strengths for the specimens with and without shear plane reinforcement, two separate material behaviors were needed. Stress-strain curves for NC specimens,  $f'_c = 4,500\text{psi}$ , are shown in Figure 3-12 and Figure 3-13. Stress-strain curves for NCS specimens,  $f'_c = 4,950\text{psi}$ , are shown in Figure 3-14 and Figure 3-15.

Other parameters are required in the CDP model as described in the Finite Element Method section in Chapter 2. Table 3-3 shows the values used for both the NC and NCS models.

### **Steel material model**

Material models used to describe the behavior of the reinforcement in the models were elasticity and plasticity material models in Abaqus. The Park and Paulay steel model, as described in Chapter 2 was implemented to calculate the stress-strain behavior of the reinforcement for both NC and NCS specimens (R. Park and Paulay 1975). Mild steel deformed bars in both specimens had a yield strength of 60 ksi. The stress-strain behavior is shown in Figure 3-16.

### **Elements**

The concrete was modeled using first-order C3D8R elements, as described in the Finite Element section in Chapter 2. Earlier models used Abaqus/Standard, which allowed higher-order elements to be used, but had convergence issues during the analysis. An explicit analysis had to be used to overcome these convergence issues in the model. Abaqus/Explicit does not allow the use of quadratic brick elements. These elements were selected due to their suitability for large strain gradients as well as plasticity analysis.

Reinforcement was modeled using B31 beam elements. This is the only wire element available in Abaqus/Explicit but has been validated in previous work its ability to capture the behavior of the reinforcement. The embedded element technique is used in conjunction with the beam elements and will be discussed further in this section.

### **Rebar Embedment**

The embedment feature in Abaqus was used to tie the concrete and the reinforcing bars in the model. Modeling the reinforcement as 3D elements is possible but introduces much complexity. Not only is the modeling technique advanced but the interaction between the concrete and the steel would need to be defined properly if good agreement with physical behavior is expected. Since the main behavior of the steel in uncracked push-off specimens is tension, wire elements with the embed constraint in Abaqus is justified. Essentially, the embedment feature in Abaqus ties the nodes of the wire elements to the solid elements so that they move together. Although this behavior is an approximation to the physical behavior, it is acceptable for this application.

### **Element Dimensions**

The mesh for early models of the push-off specimens was seeded and meshed so that all the elements had a characteristic length of 0.5 inch. This means all C3D8R brick elements were 0.5 inch cubes while the B31 beam elements were 0.5 inches long. Figure 3-17(a) depicts this mesh. Once the load-deformation behavior was established as acceptable, this mesh was refined to include a varying mesh size. Finer elements were used in the region of the shear plane (0.5 in.<sup>3</sup>) while element size increased in the region outside the shear plane. In these refined mesh models, the shear plane stirrups were meshed such that the elements were the same size as the shear plane elements.

This reduced the run time by roughly ten times. The refined mesh can be seen in Figure 3-17(b). For completeness, Figure 3-18 shows the model with the reinforcement placed. Embedment of the reinforcing in the concrete will be discussed further in this section.

### **Analysis Type**

All models were run using Abaqus/Explicit. Abaqus/Standard had convergence issues that could not be overcome. Abaqus/Explicit also allows the simulations to be run with dynamic loading such as drop hammer simulations which are outside the scope of this work but planned for future research.

### **Boundary Conditions**

As mentioned in the beginning of this section, modeling of the steel supports proved to be unnecessary and cause convergence issues mainly due to the contact conditions that need to be specified in Abaqus. Instead, the top and bottom surfaces were prescribed boundary conditions. The bottom surface was prescribed a fix boundary condition while the top surface was prescribed a displacement.

As can be seen in Figure 3-4 and mentioned earlier, the exact width of both the loading and base plates were not reported by Valle and Buyukozturk. An assumption had to be made from the picture of the test setup and validated through a parametric study to see the effect, if any, the surface area of the displacement condition and the base condition had on the results. The results are presented and discussed in the following chapter.

### **Summary**

This chapter discussed the research approach and methods used in this study which included selecting a study for use of verifying the FE model, the details of that study to be replicated in Abaqus, and the results obtained for the experimental work.

This was followed by a brief summary of the evolution of the modeling techniques and finally the details of the model used for the final results.

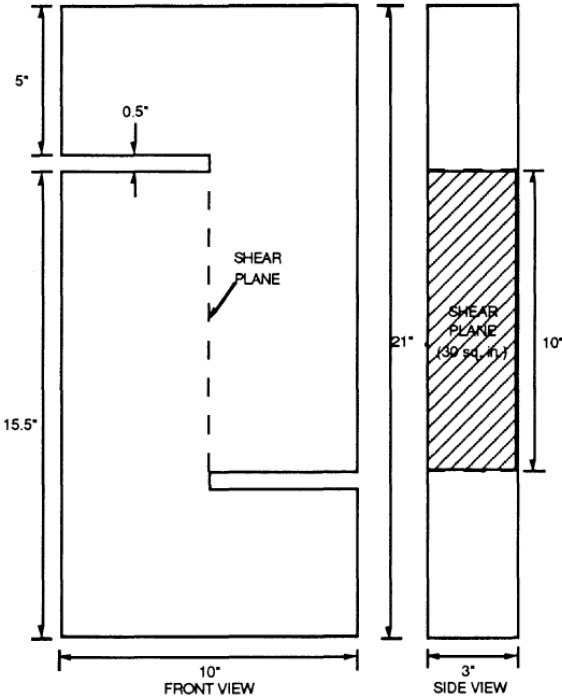


Figure 3-1. Push-off specimen geometry (Valle and Buyukozturk 1993)

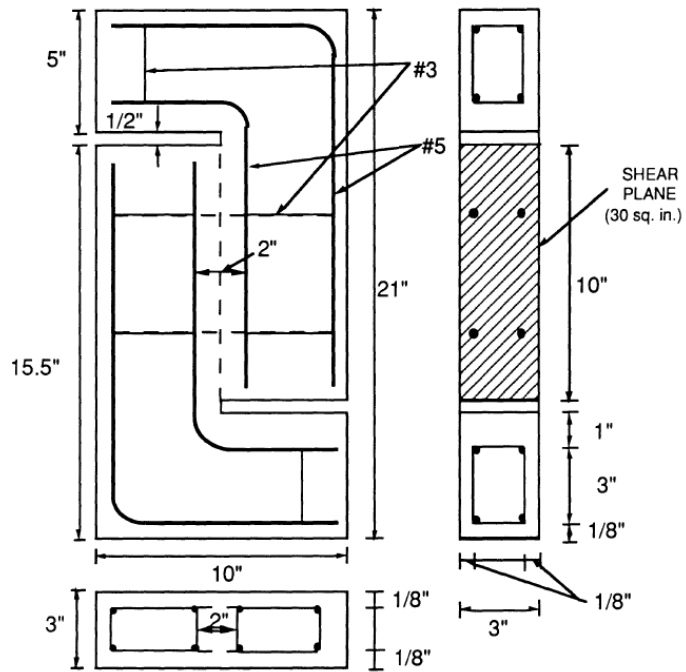


Figure 3-2. Push-off specimen reinforcement detail (Valle and Buyukozturk 1993)

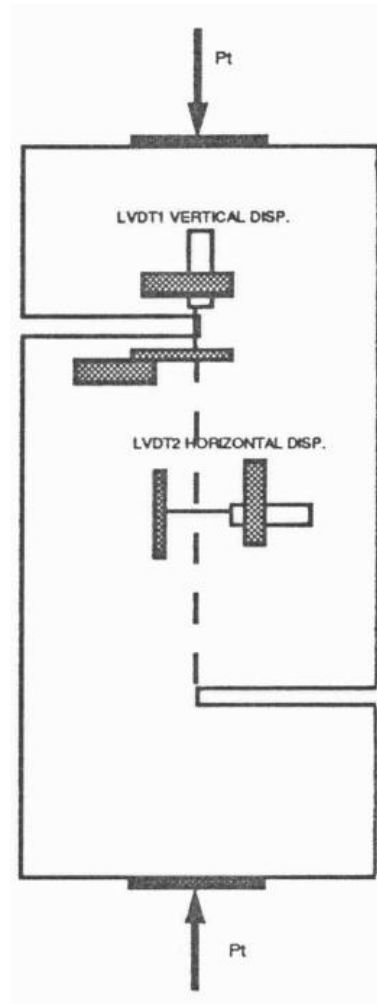


Figure 3-3. LVDT placement and loading configuration (Valle and Buyukozturk 1993)

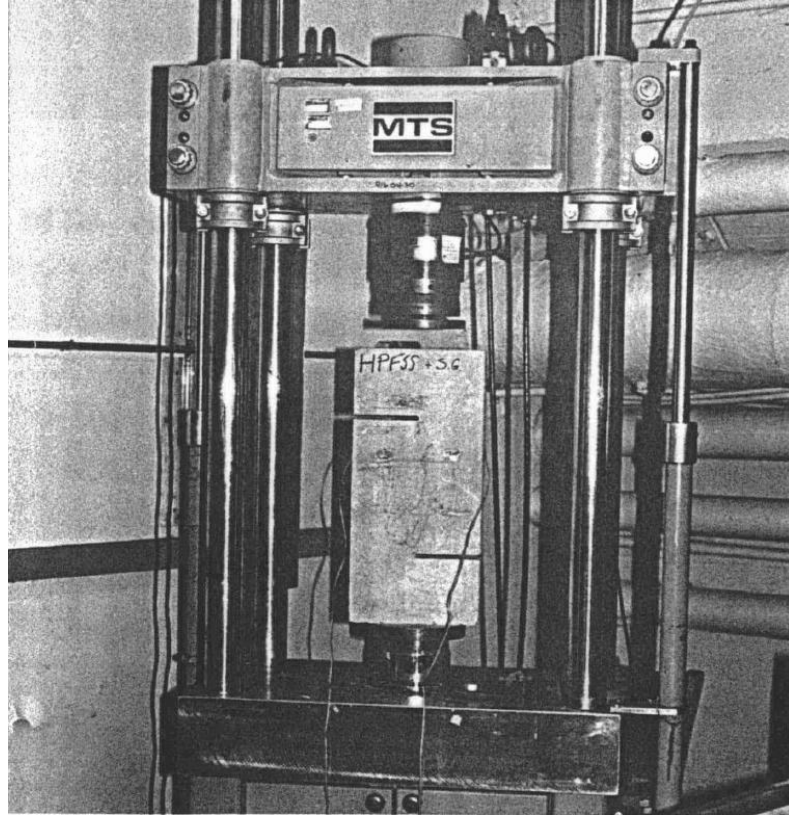


Figure 3-4. Loading configuration (Valle and Buyukozturk 1993)

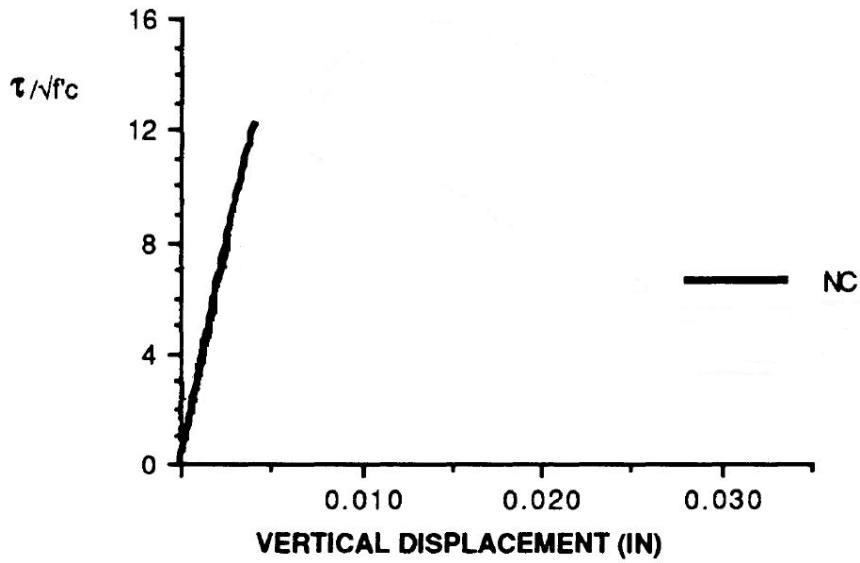


Figure 3-5. Normalized shear stress vs. vertical displacement for NC (Valle and Buyukozturk 1993)

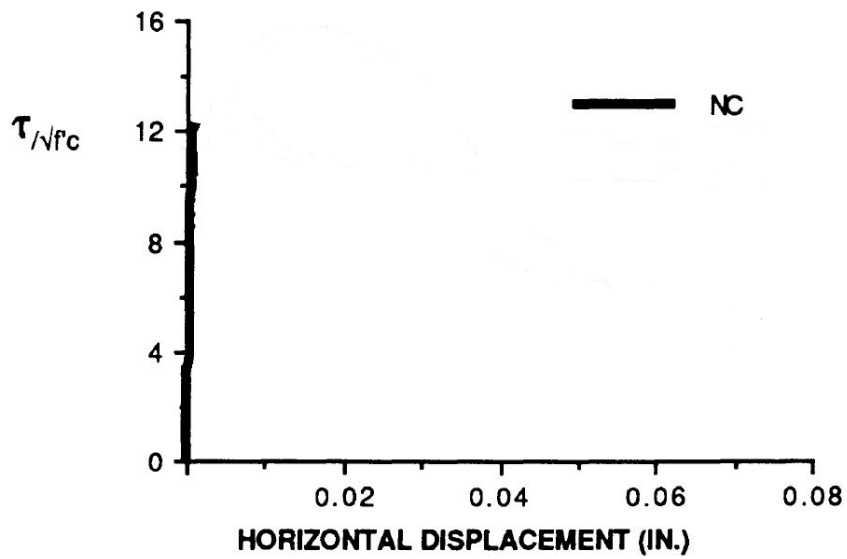


Figure 3-6. Normalized shear stress vs. horizontal displacement for NC (Valle and Buyukozturk 1993)

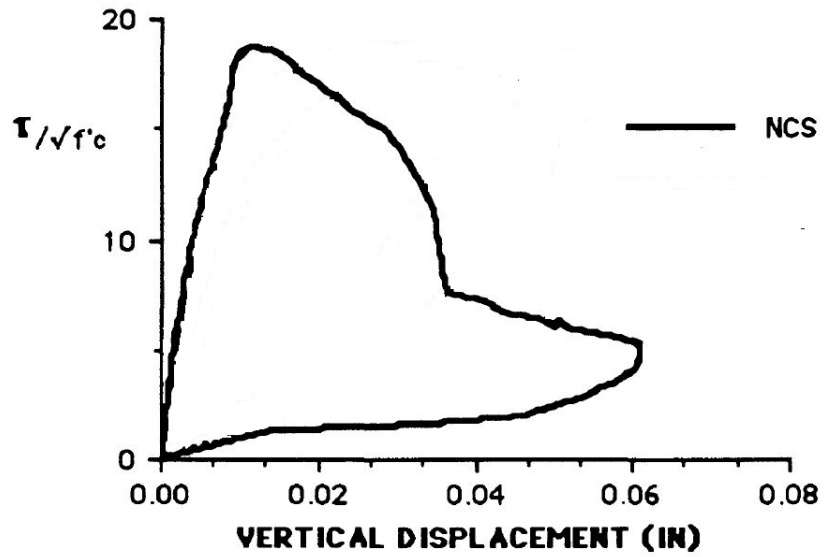


Figure 3-7. Normalized shear stress vs. vertical displacement for NCS (Valle and Buyukozturk 1993)

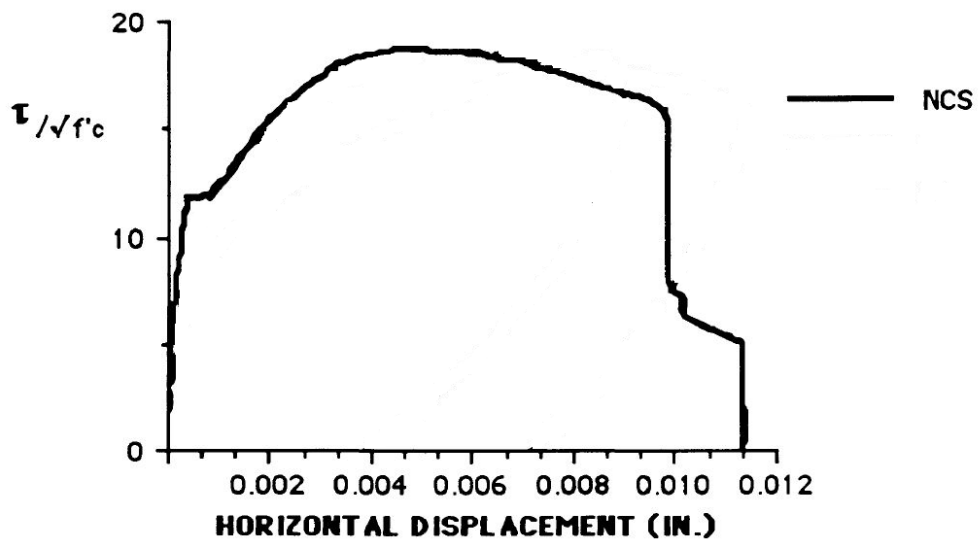


Figure 3-8. Normalized shear stress vs. horizontal displacement for NCS (Valle and Buyukozturk 1993)

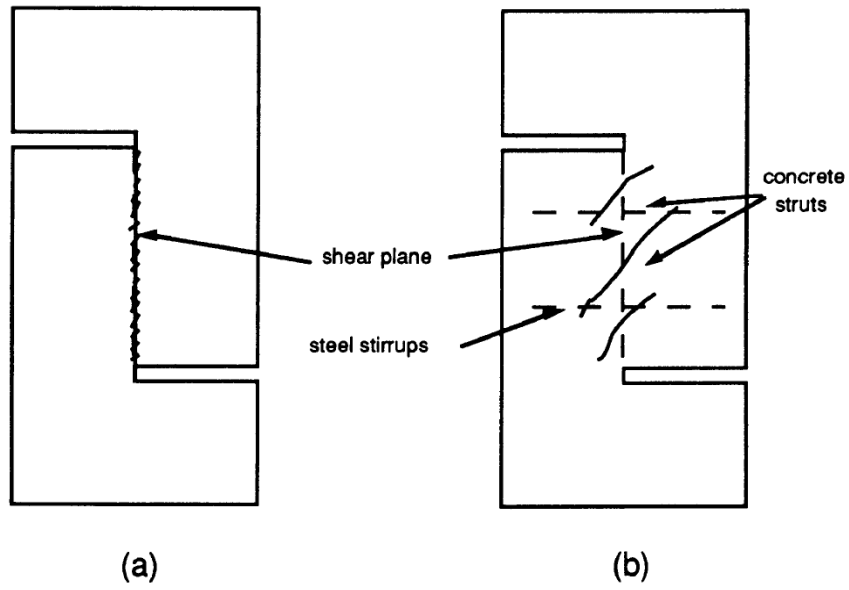


Figure 3-9. Cracking patterns for push-off specimens. (a) with no shear plane stirrups and (b) with shear plane stirrups (Valle and Buyukozturk 1993)

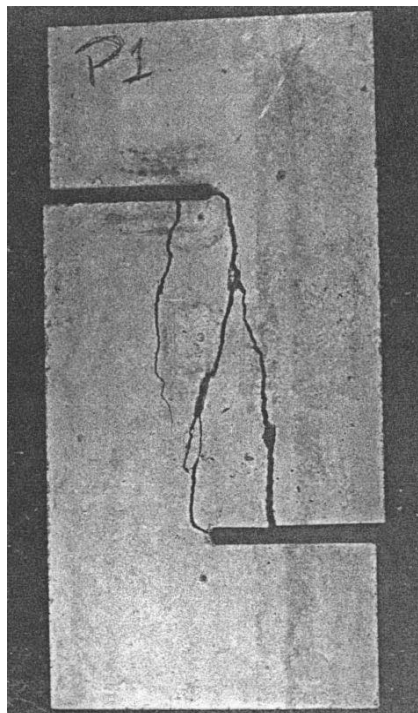


Figure 3-10. NC specimen after failure (Valle and Buyukozturk 1993)



Figure 3-11. NCS specimen after failure (Valle and Buyukozturk 1993)

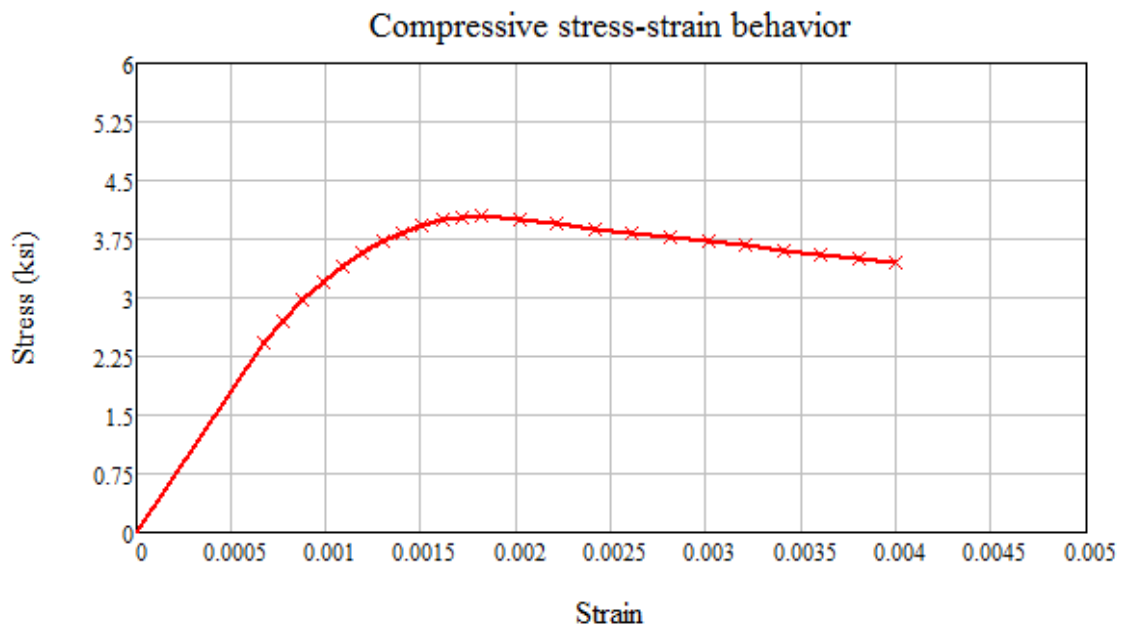


Figure 3-12. NC compressive stress-strain relationship

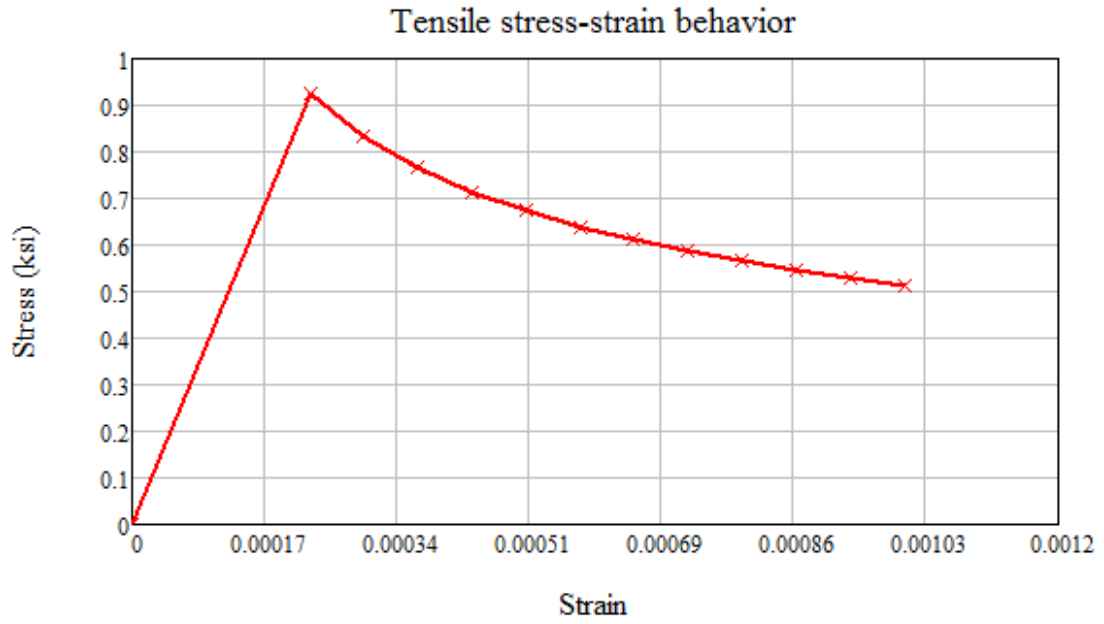


Figure 3-13. NC tensile stress-strain relationship

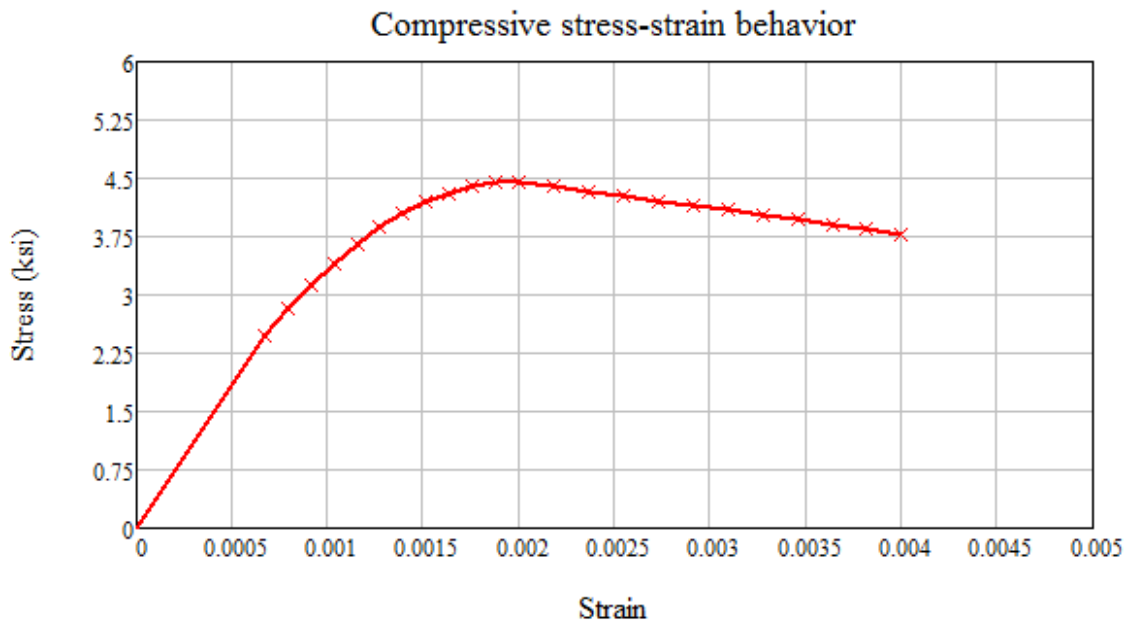


Figure 3-14. NCS compressive stress-strain relationship

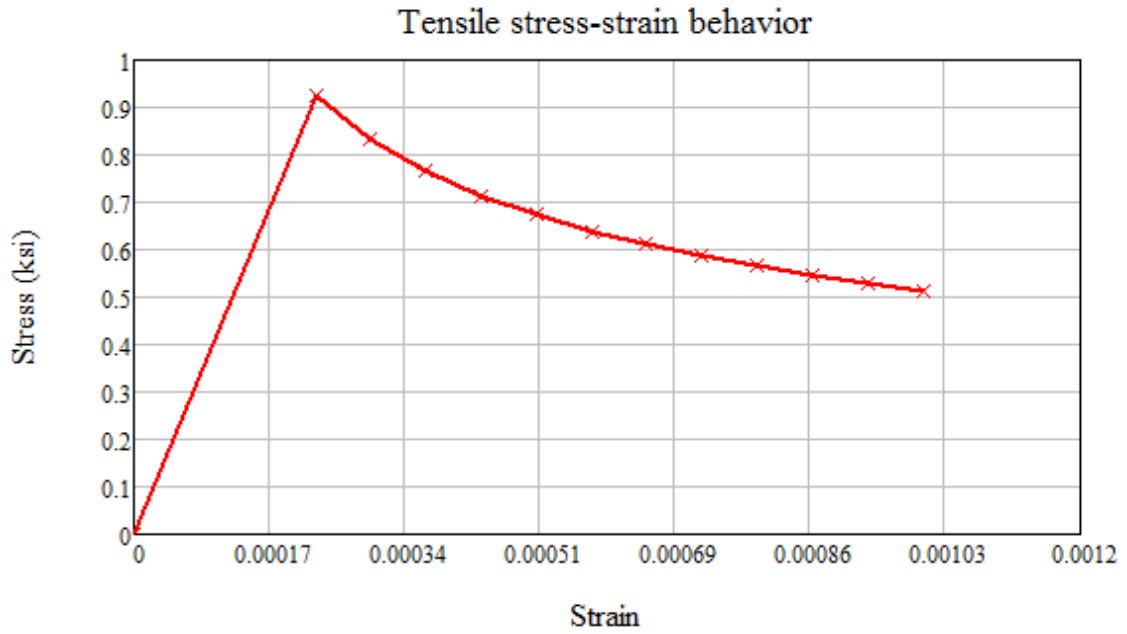


Figure 3-15. NCS tensile stress-strain relationship

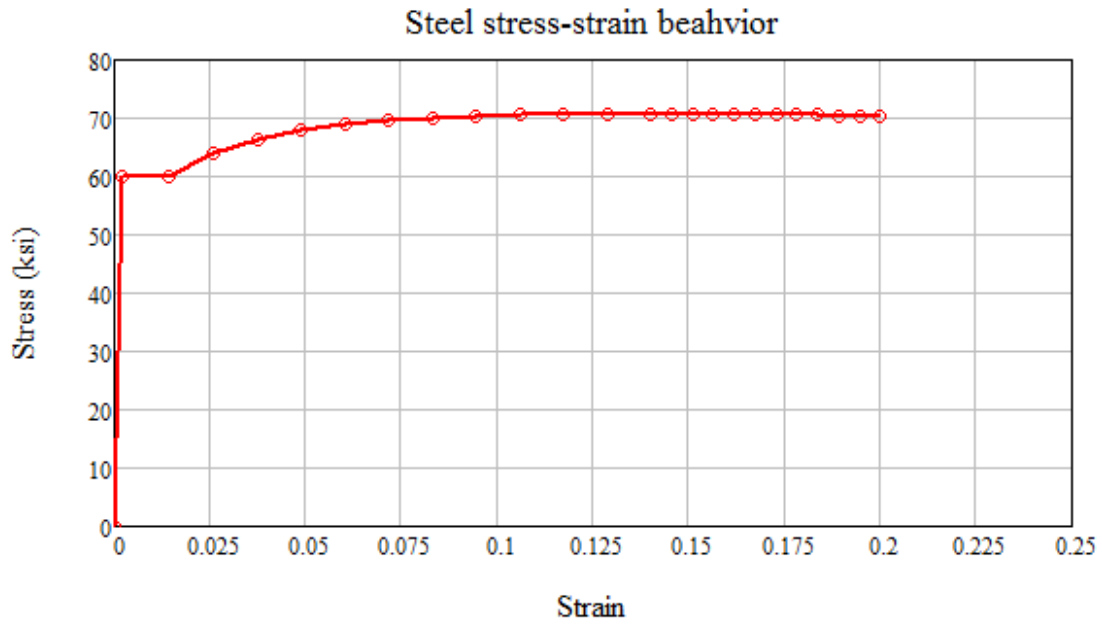
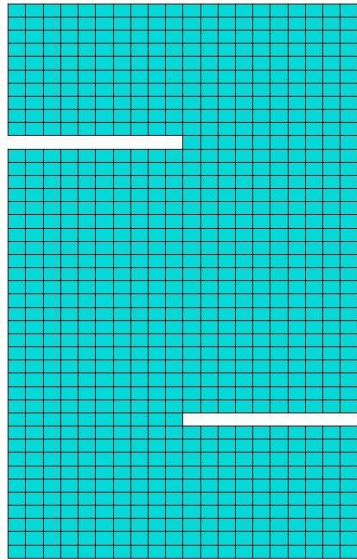
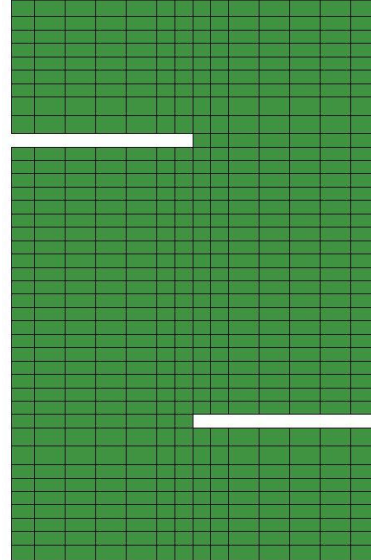


Figure 3-16. Mild steel stress-strain behavior for 60 ksi deformed bars



(a)



(b)

Figure 3-17. Mesh density. (a) initial mesh. (b) refined mesh

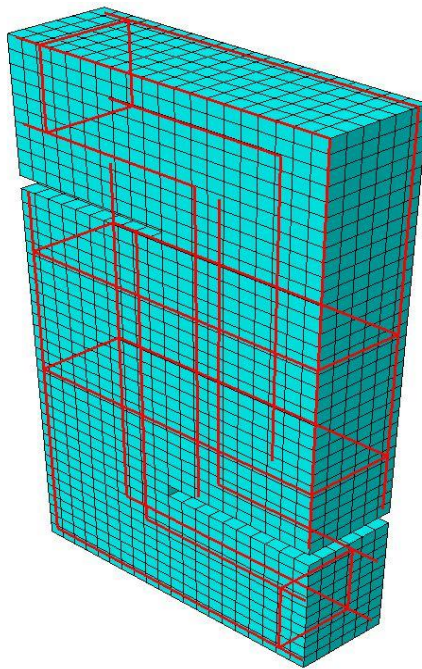


Figure 3-18. Reinforcement in the model

Table 3-1. Concrete mix proportions by weight

Mix	Cement	Sand-cement Ratio	Aggregate-cement ratio	Superplasticizer-cement ratio	Water-cement ratio
NC	1	1.7	2.0	0.5%	0.40

Table 3-2. Valle test results for NC and NCS push-off specimens

Specimen	$f'_c$ (psi)	$f'_{st}$ (psi)	$P_{max}$ (lbs)	$\tau_{max}$ (psi)	$\tau_{max} / \sqrt{f'_c}$	$\tau_{cr}$ (psi)
NC-1	4,500	350	23,251.8	775.06	11.55	775.06
NC-2	4,500	350	22,323.9	744.13	11.09	744.13
NCS-1	4,950	470	39,258.9	1,308.63	18.6	823.87
NCS-2	4,950	470	38,203.5	1,273.45	18.1	805.58

Table 3-3. CDP material model parameters

Parameter	Value
E, Young's modulus	3,824 – 4,010 ksi
Density	150 lb/ft <sup>3</sup>
$\nu$ , Poisson ratio	0.20
$\varphi$ , Dilation angle	36.31
$\varepsilon$ , eccentricity	0.1
$f_{bo} / f_{co}$	1.16
$K$	0.666667
$\mu$ , Viscosity parameter	0

## CHAPTER 4 RESULTS AND DISCUSSION

This chapter will present and discuss the simulation results for the finite element models. The method of recording the vertical displacement and selection of boundary conditions will be discussed and the results compared. The Hawkins shear model will also be discussed and compared to the experimental results.

### **Loading Cases**

Three load cases, or boundary conditions were modeled to compare the effect on the results. As mentioned previously, the loaded area and base area of the experimental tests were not recorded. The load cases are shown below in Figure 4-1. It was assumed that the entire width of the top and bottom surface was loaded. Three cases were chosen as follows.

- Load Case 1. Full top and bottom surface (10" x 3") (100%)
- Load Case 2. Partial top and bottom surface (3.675" x 3") (36.75%)
- Load Case 3. Partial top and bottom surface (7.05" x 3") (70.5%)

### **Recording Vertical Displacement**

In the process of the study, it was observed that depending on where the vertical displacement was recorded from in the model, results varied considerably. After investigating the experimental setup, see Figure 4-2, the relative slip, or vertical displacement, of the shear plane was measured as the difference between the attachment point of LVDT1, located in the top portion of the specimen, and the attachment point of the LVDT1 plate, located on the left block. Both of these were on the face of the specimen. These locations are marked by red dots in the figure. Their decision to record the vertical displacement in this fashion was not discussed in the paper.

The simulations conducted utilized five different methods of recording and calculating the relative slip between the left and right blocks across the shear plane.

- Type 1
- Type 2
- Type 3
- LVDT 1
- LVDT 2

The Type 1 node set took the average of all the nodes vertical to the shear plane roughly in the middle of the left and right side block as shown in Figure 4-3. The difference was then taken to get the relative vertical displacement between the two blocks. The Type 2 node set had the same methodology except the nodes vertical to the shear plane were taken on the outside of the elements on either side of the shear plane as shown in Figure 4-4. The Type 3 node set also had the same methodology of the previous two except the nodes vertical to the shear plane were located on the edges of the specimen as shown in Figure 4-5. All three methods recorded the nodes at mid-thickness of the model.

The other two methods of recording the relative vertical displacement attempted to simulate locations on the specimen where LVDTs could be placed in a lab setting. They both record single points on the face of the concrete and track that point throughout the loading as opposed to averaging nodes along the shear plane. LVDT 1 was devised to match the recordings of LVDT1 in the experimental tests. The nodes recorded for LVDT 1 are shown in Figure 4-6. The difference of the recorded vertical displacements was taken to get the relative slip of the shear plane. LVDT 2 recorded the same left block node as LVDT 1 but changed the location of the node on the right block. The right side

node was recorded in the same location of the left side node. The nodes recorded for LVDT 1 are shown in Figure 4-7.

### **Simulation Results**

Presented here are the results of both NC and NCS simulations. The specimen bottom surface is fixed while the top surface was prescribed a displacement. For each loading case and specimen type, normalized shear stress vs. vertical displacement is plotted. Shear stress was calculated by summing the reaction forces over the nodes of the bottom surface and dividing by the shear plane area (30 in.<sup>2</sup>). This was then normalized by the square root of the compressive strength of the specimen.

The three loading cases as described earlier in the chapter are applied to both NC and NCS specimens. In addition, the five vertical displacement measurement methods are plotted for each load case. This gives a comprehensive look at the effect the loading condition as well as the vertical displacement recording can have. The NC and NCS experimental results are included in the plots for comparison.

### **NC Results**

As stated earlier, these specimens had no shear plane reinforcement. Figure 4-8 shows load case 1, full top and bottom boundary conditions (10" x 3"). Figure 4-9 shows load case 2, partial top and bottom boundary conditions (3.675" x 3"). Figure 4-10 shows load case 3, partial top and bottom boundary conditions (7.05" x 3").

Failure of the specimens occurred along the shear plane. This can be seen in Figure 4-11 which shows the maximum principle strains at the integration points at the time of failure.

Table 4-1 shows a summary of the results for the NC model. Numerically, the model continues to run past the abrupt loss of stiffness which can be seen in all the preceding plots for the NC specimen. The assumption is that the specimen would fail at the first loss of stiffness. This sharp drop in load can be attributed to concrete spalling near the cut-out corners and possibly the development of a crack through the shear plane. In the results comparison table, the values for the maximum load,  $P_{max}$ , are taken at the point before this abrupt loss in stiffness. Since no displacement values were reported in the experimental study, Figure 3-5 was digitized in order to estimate the displacement at failure for the NC specimen.

### **NCS Results**

As stated earlier, these specimens included shear plane reinforcement in the form of (2) #3 closed stirrups which produces a reinforcement ratio of  $\rho = 1.47\%$ . Figure 4-12 shows load case 1, full top and bottom boundary conditions (10" x 3"). Figure 4-13 shows load case 2, partial top and bottom boundary conditions (3.675" x 3"). Figure 4-14 shows load case 3, partial top and bottom boundary conditions (7.05" x 3").

Table 4-2 shows a summary of the results for the NCS model. In the results comparison table, the values for the maximum load,  $P_{max}$ , are taken at the maximum load. Since no displacement values were reported in the experimental study, Figure 3-5 was digitized in order to estimate the displacement at failure for the NC specimen. The failure displacement can be taken as when the concrete compression struts failed by crushing and unloading started to take place and can be seen in Figure 3-7.

## **Hawkins Shear Model**

As discussed in Chapter 2, the Hawkins shear model was proposed for shear transfer in flexural members with very small shear span to depth ratios. There also is a modified Hawkins shear model proposed by Krauthammer et al. (1986) that included the effects of in-plane compression and strain rate. For the direct shear specimens tested by Valle & Buyuktozurk (1993), the Hawkins shear model is applied to see its usefulness in capturing the shear stress-shear slip behavior of push-off specimens. Figure 4-15 shows the comparison to the model predictions and the test data for the NCS specimen. The peak normalized shear stress of the NCS specimen was 18.34 while the Hawkins model predicts a peak normalized shear stress of 18.01. This is a difference of 1.8%. While the behavior after the peak shear stress is quite different, it very accurately predicts the peak capacity of the push-off specimen. A closer look at the initial stiffness and cracking shear stress shows very good agreement as well as can be seen in Figure 4-16. The average cracking normalized shear stress of the two NCS specimens was reported as 11.58 while the Hawkins model predicts the cracking normalized shear stress as 8.99. This is a difference of roughly 22%.

### **Summary**

This section discussed the details of the FE model used to capture the results. This was followed by a presentation of the FE results as well as a summary of the results for comparison. Finally, the Hawkins shear model was compared to the experimental results to explore its usability in predicting the shear stress-shear slip relationship for push-off specimens

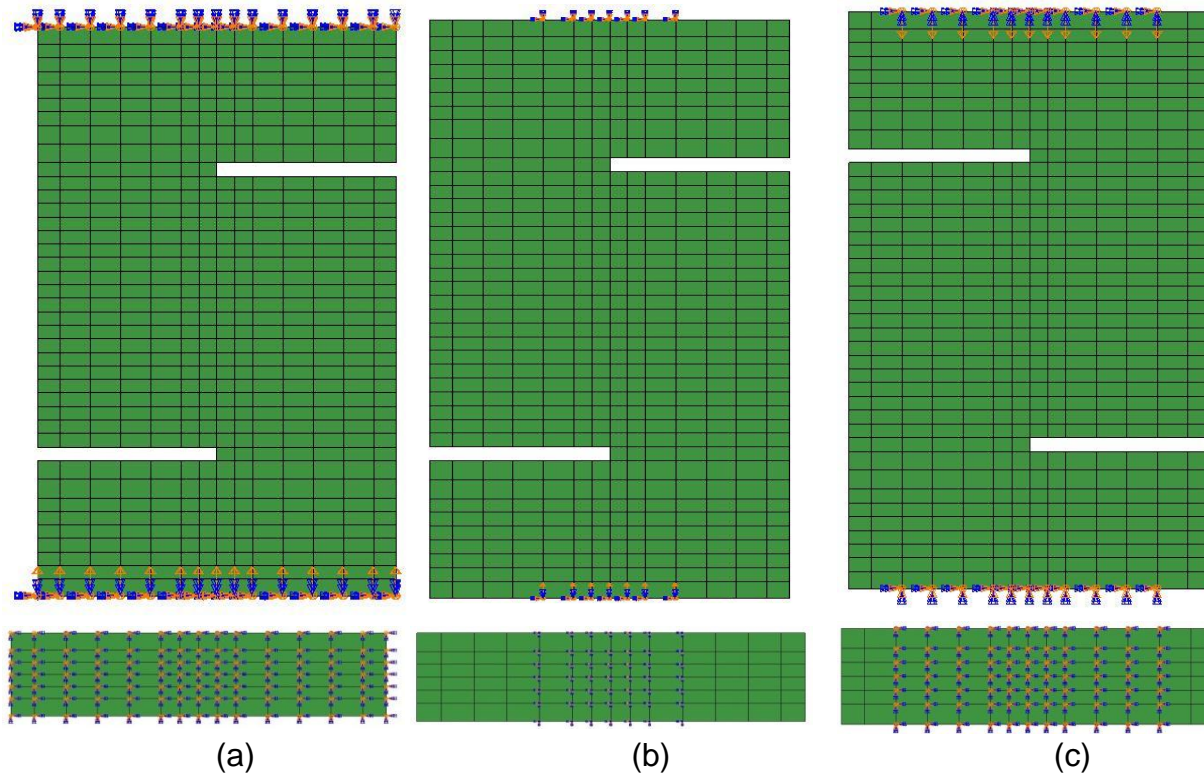


Figure 4-1. Boundary conditions. (a) Load case 1. (b) Load case 2. (c) Load case 3

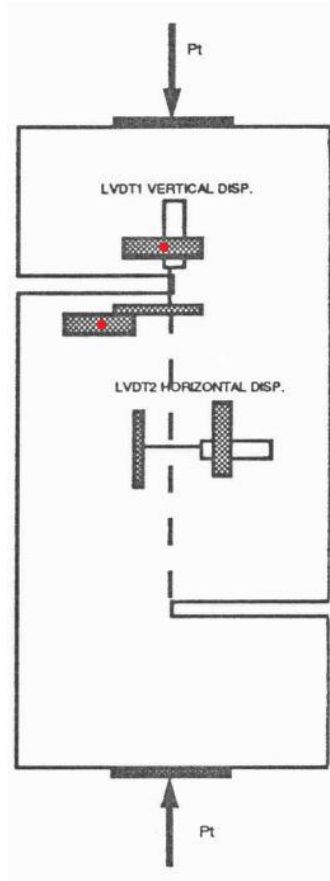


Figure 4-2. LVDT setup for the experimental testing

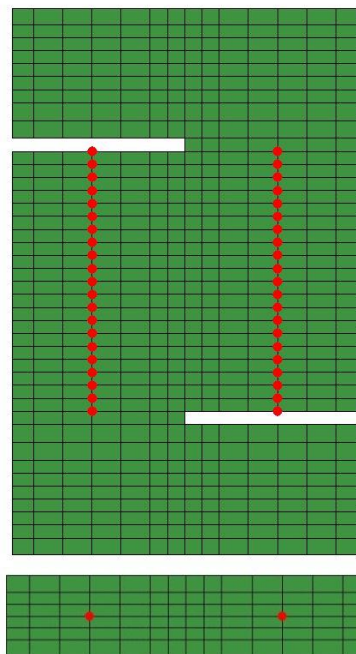


Figure 4-3. Type 1 node set



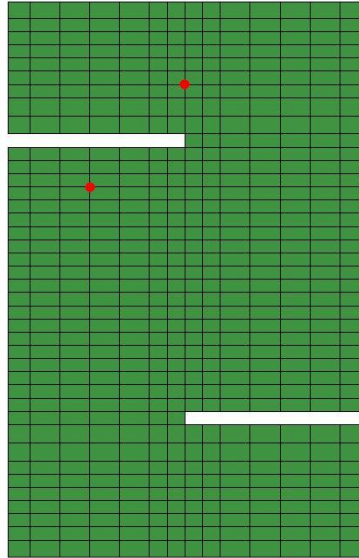


Figure 4-6. LVDT 1 node set

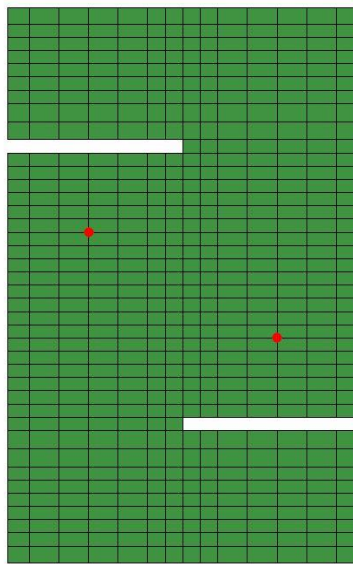


Figure 4-7. LVDT 2 node set

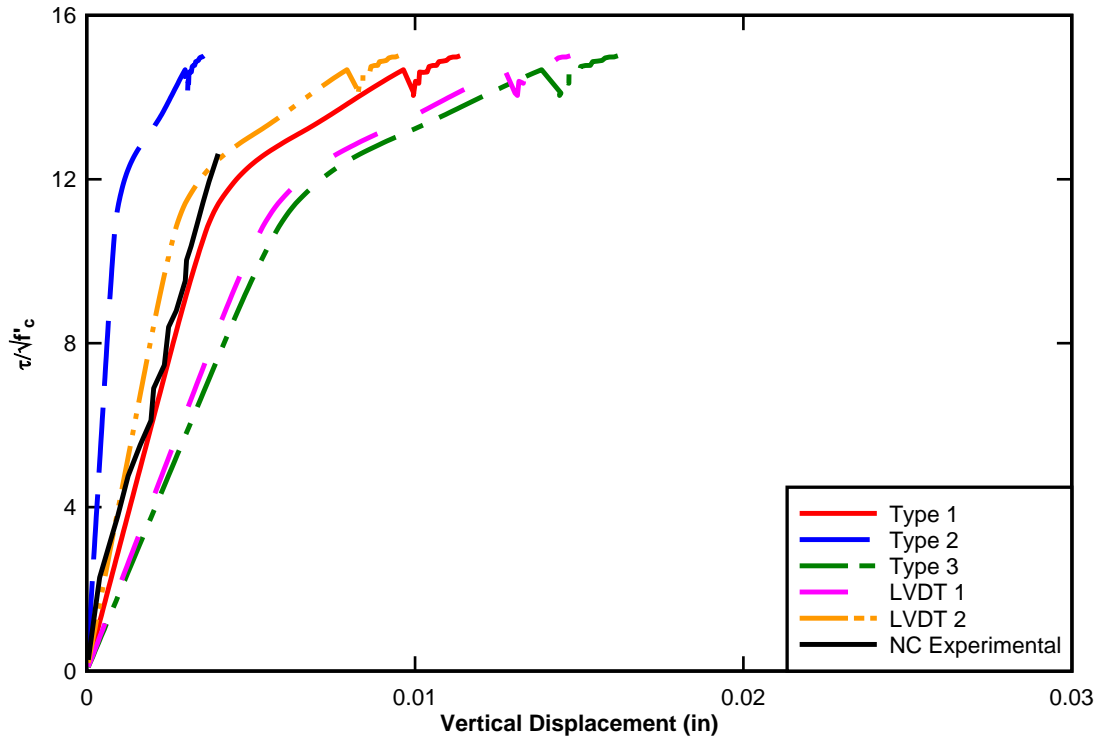


Figure 4-8. NC with load case 1

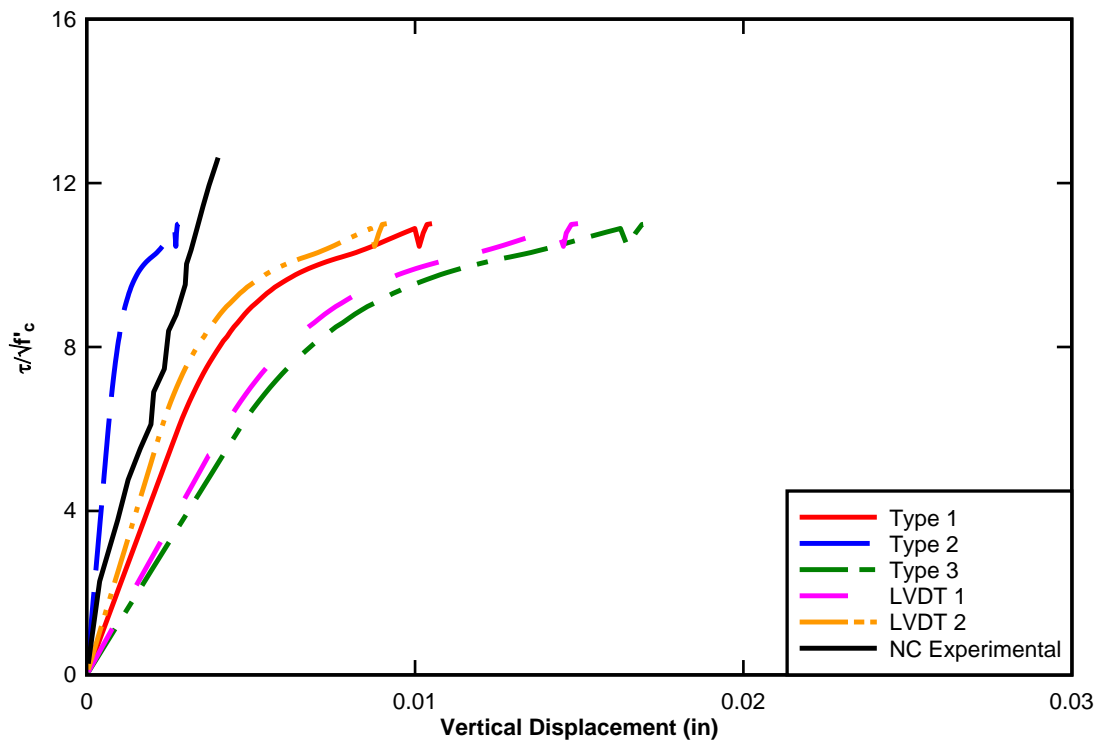


Figure 4-9. NC with load case 2

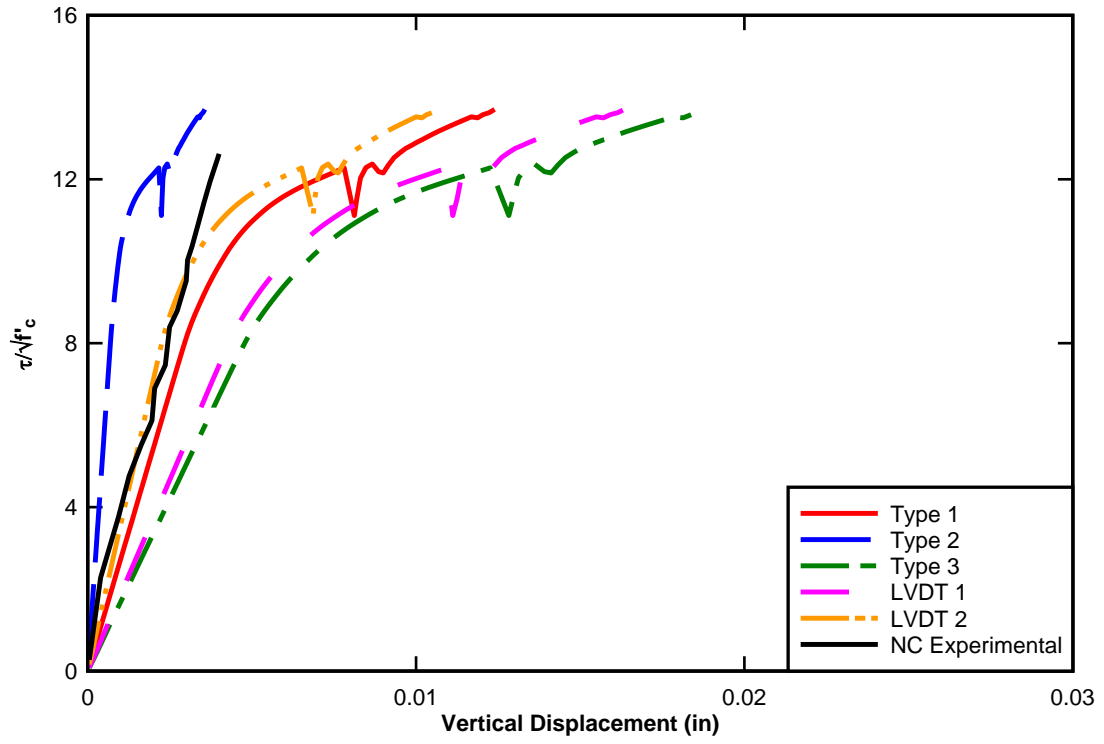


Figure 4-10. NC with load case 3

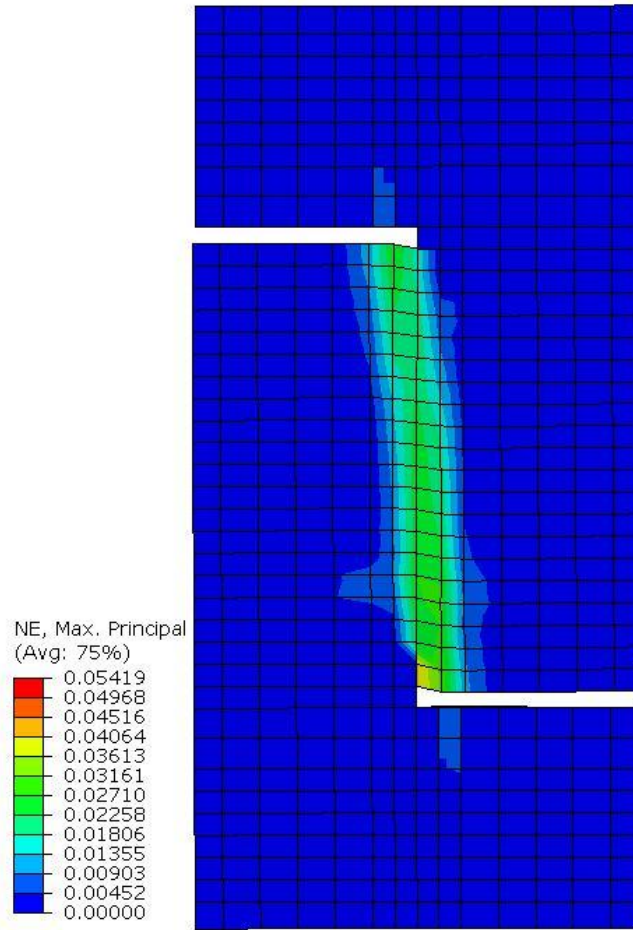


Figure 4-11. Maximum principal strains at integration points at failure

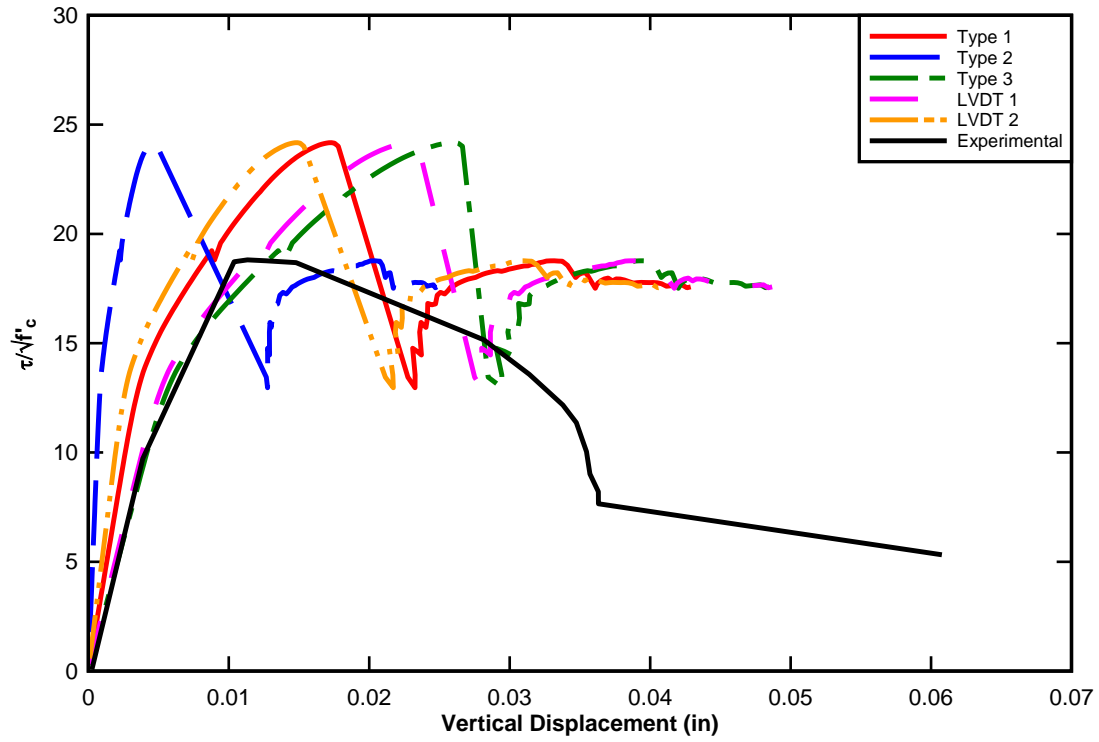


Figure 4-12. NCS with load case 1

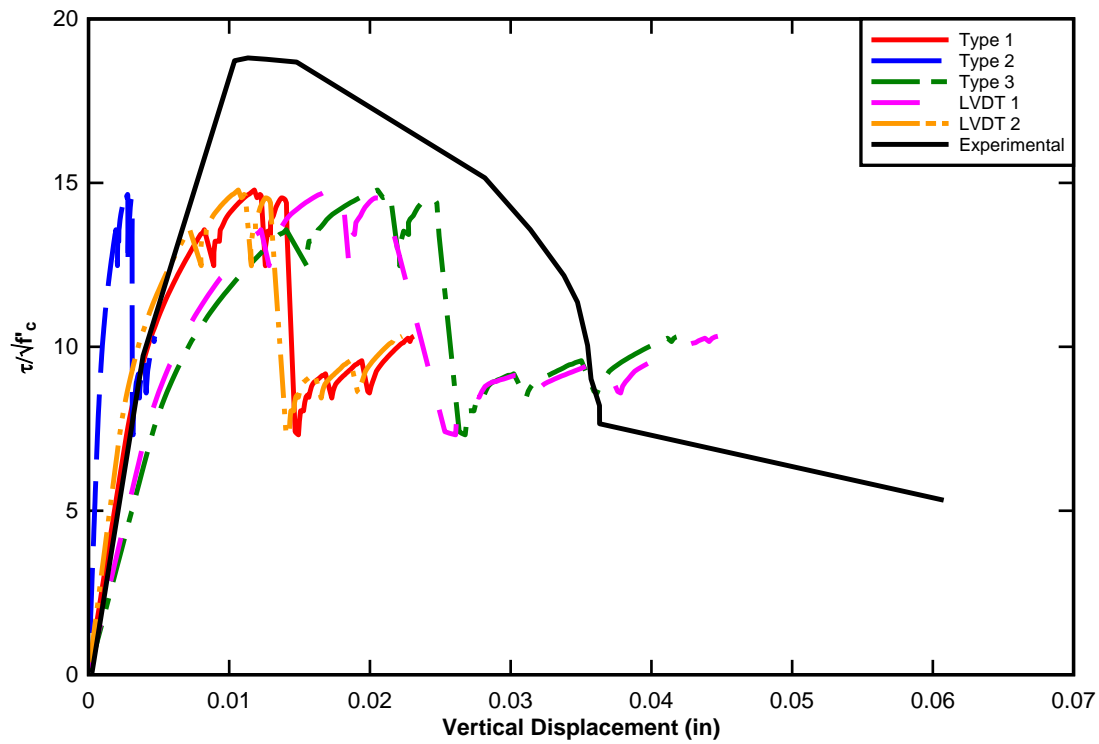


Figure 4-13. NCS with load case 2

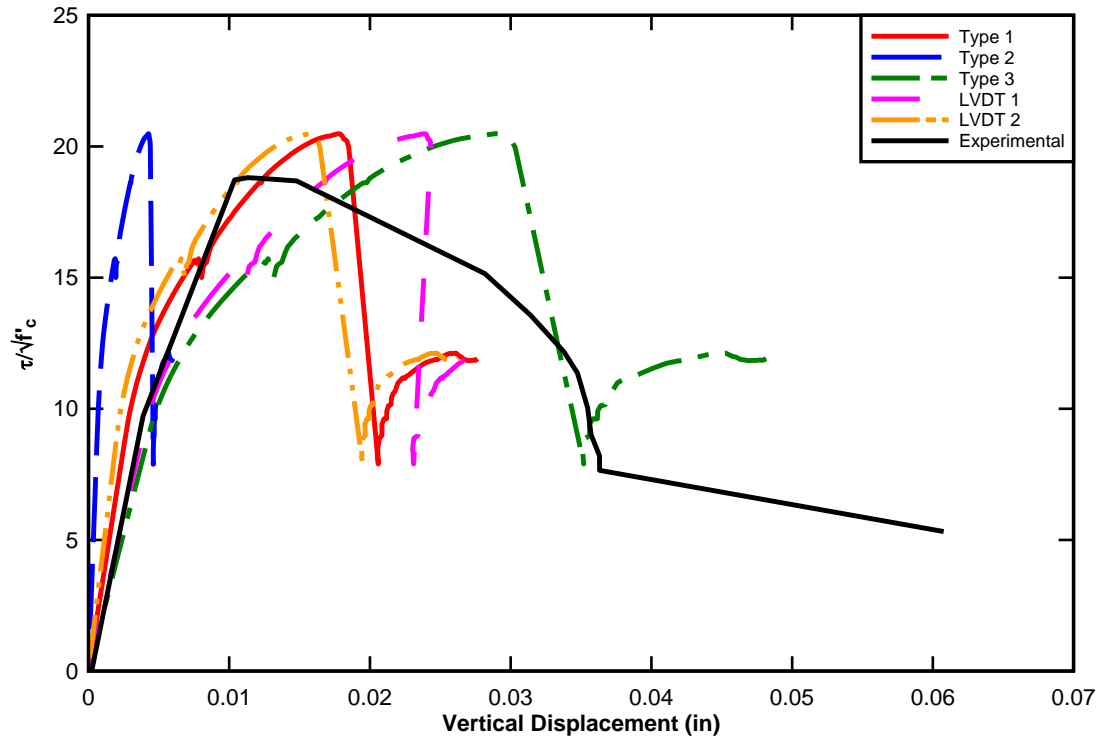


Figure 4-14. NCS with load case 3

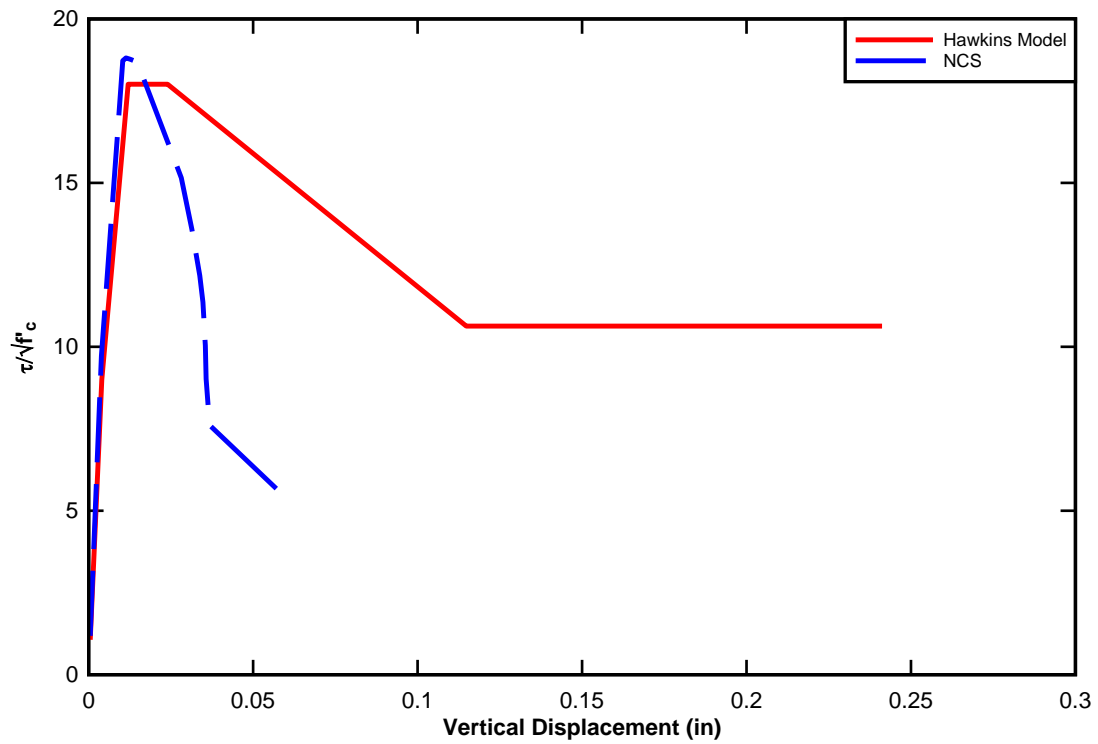


Figure 4-15. Normalized shear stress vs. vertical displacement

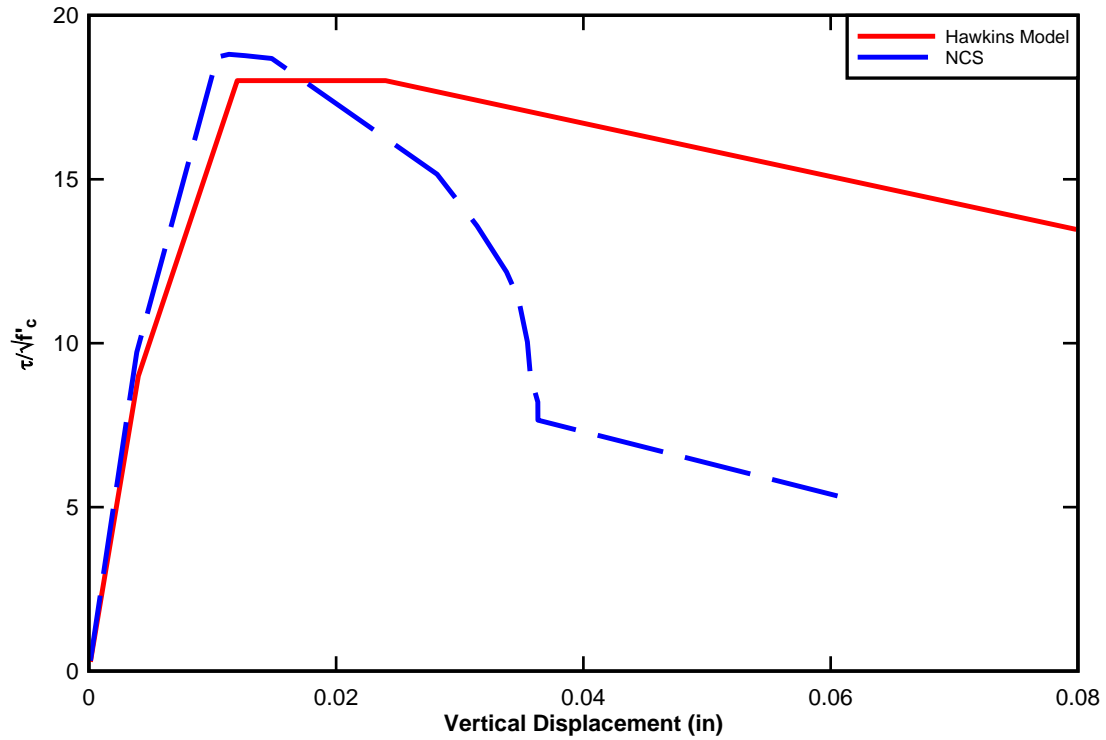


Figure 4-16. Normalized shear stress vs. vertical displacement

Table 4-1. Comparison of results for NC specimens

Displacement Type	$P_{max}$ (lbf)	$T_{max}$ (psi)	$\frac{\tau_{max}}{\sqrt{f'_c}}$	$\frac{\tau_{max}}{\sqrt{f'_c}}$ (% difference)	Vertical Displacement at $P_{max}$ (in.)	Vertical displacement % difference
Type 1					0.007814	48.8%
Type 2					0.002166	-84.7%
Type 3	25,916.2	863.9	12.28	7.82%	0.012257	67.4%
LVDT 1					0.010947	63.5%
LVDT 2					0.006514	38.6%
Experiment	22,787.9	759.6	11.32	--	0.004000	--

Table 4-2. Comparison of results for NCS specimen

Displacement Type	$P_{max}$ (lbf)	$T_{max}$ (psi)	$\frac{\tau_{max}}{\sqrt{f'_c}}$	$\frac{\tau_{max}}{\sqrt{f'_c}}$ (% difference)	Vertical Displacement at $P_{max}$ (in.)	Vertical displacement % difference
Type 1					0.017779	34.6%
Type 2					0.004263	-172.7%
Type 3	43,244.1	1,441.5	20.49	10.49%	0.028963	59.9%
LVDT 1					0.023879	51.3%
LVDT 2					0.015695	25.9%
Experiment	38,731.2	1,291.0	18.34	--	0.011624	--

## CHAPTER 5 CONCLUSIONS AND RECOMMENDATIONS

### **Conclusions**

Continuum based FE models of push-off specimens are extremely sensitive to both the area of the top and bottom surface for the boundary conditions and prescribed displacement and the method of recording the relative vertical displacement. The reinforced push-off specimen resistance curve follows reasonably well up to ultimate strength but differs in post-peak behavior.

The CDP model in Abaqus may not be appropriate for this type of behavior. Investigation of using a different material model in a different FE code should be pursued to see if any differences in behavior can be seen.

The Hawkins model fairly accurately predicts the peak and cracking shear stress but is unreliable after that. This could be due to the NSC specimens not actually completely failing, leaving a permanent deformation. All NSC push-off specimens, with initially uncracked shear planes, fail by the compression struts failing, not by the yielding of the stirrups. The Hawkins model was is intended for use on slabs and assumes total failure of the section. This could be one reason why it does not capture the post-peak behavior for initially uncracked NSC push-off specimens.

### **Recommendations for Future Research**

Investigation into using a different finite element code as well as material model formulation for the concrete should be completed to see if any improvements can be made in the behavior of the reinforced push-off specimens. Introducing UHPC material properties into the CDP material model should also be investigated and results confirmed with test data do see if good results can be accomplished.

Pre-test predications of the behavior of both NSC and UHPC push-off specimens should be conducted as well as experimental testing of direct shear push-off specimens, both NSC and UHPC. The pre-test predications can then be compared to the experimental test data and modifications of the numerical simulations can take place as needed.

The Hawkins shear model should be modified to predict the post-peak behavior of reinforced concrete push-off specimens. Once experimental testing is done, on both NSC and UHPC specimens, this task can be accomplished.

These recommendations, if implemented, can provide much more information as well as tools to accurately predict the direct shear response of push-off specimens and provide a base of knowledge for studying the direct shear behavior of UHPC.

## LIST OF REFERENCES

- Acker, P., and Behloul, M. (2004). "Ductal Technology: a Large Spectrum of Properties, a wide range of applications." *Proceedings of the International Symposium on Ultra High Performance Concrete*, Kassel University Press, Kassel, Germany, 11–24.
- Association Française de Génie Civil. (2002). *Ultra High Performance Fibre-Reinforced Concrete - Interim recommendations (Annexes)*. France, 98.
- Astarlioglu, S., Krauthammer, Theodor, and Felice, C. (2010). *State-of-the-Art Report on Fiber Reinforced Ultra-High Performance Concrete*. University of Florida, Gainesville, Fla.
- Birkeland, P., and Birkeland, H. (1966). "Connections in Precast Concrete Construction." *Journal of American Concrete Institute*, 63(3), 345–368.
- Brandt, A. M. (2008). "Fibre Reinforced Cement-Based (FRC) Composites after over 40 Years of Development in Building and Civil Engineering." *Composite Structures*, 86(1-3), 3–9.
- Colleparidi, M. (1998). "Admixtures used to enhance placing characteristics of concrete." *Cement and Concrete Composites*, 20(2–3), 103–112.
- Collins, M. P., and Mitchell, D. (1991). *Prestressed Concrete Structures*. Prentice-Hall, Inc.
- Fehling, E., Schmidt, M., Teichmann, T., Bunje, K., Bornemann, R., and Middendorf, B. (2004). *Entwicklung, Dauerhaftigkeit und Berechnung Ultrahochfester Betone (UHPC): Forschungsbericht DFG FE 497/1-1*. Kassel University Press.
- Fish, J., and Belytschko, T. (2007). *A First Course in Finite Elements*. John Wiley & Sons, Ltd.
- Graybeal, B. A. (2005). "Characterization of the behavior of ultra-high performance concrete." University of Maryland, College Park.
- Habel, K. (2004). "Structural Response of Elements Combining Ultrahigh-Performance Fiber-Reinforced Concretes and Reinforced Concrete." PhD Thesis, Swiss Federal Institute of Technology, Lausanne, Switzerland.
- Hirschi, T., and Wombacher, F. (2008). "Influence of Different Superplasticizers on UHPC." *Proceedings of the Second International Symposium on Ultra High Performance Concrete*, Kassel, Germany, 77–84.
- Hofbeck, J. A., Ibrahim, I. O., and Mattock, A. H. (1969). "Shear Transfer in Reinforced Concrete." *ACI Journal Proceedings*, 66(2), 119–128.

- Hsu, T. T. C. (1993). *Unified Theory of Reinforced Concrete*. CRC Press.
- Hsu, T. T. C., Mau, S. T., and Chen, B. (1987). "Theory on Shear Transfer Strength of Reinforced Concrete." *ACI Structural Journal*, 84(2), 149–160.
- Kiger, S. A., and Getchell, J. V. (1980). *Vulnerability of Shallow-Buried Flat-Roof Structures*. U.S. Army Engineer Waterways Experiment Station.
- Koh, Y. H. (2011). "Characterizing a Reinforced Concrete Beam-Column-Slab Subassemblage Connection for Progressive Collapse Assessment." MS Thesis, University of Florida, Gainesville, Fla.
- Krauthammer, T., Bazeos, N., and Holmquist, T. J. (1986). "Modified SDOF Analysis of RC Box-Type Structures." *Journal of Structural Engineering*, 112(4), 726–744.
- Lafarge. (n.d.). "Ductal." <<http://www.lafarge-na.com/wps/portal/lna/products/ductal>>.
- Lallemant-Gamboa, I., Chanut, S., Lambard, J.-P., Chaignon, J., and Thibaux, T. (2005). "Formulations, Characterizations and Applications of Ultra High-Performance Concrete." *ACI Special Publication*, 228, 1221–1236.
- Ma, J., Orgass, M., Dehn, F., Schmidt, D., and Tue, N. V. (2004). "Comparative Investigations on Ultra-High Performance Concrete with or without Coarse Aggregates." *Proceedings of the International Symposium on Ultra High Performance Concrete*, Kassel, Germany, 205–212.
- Malm, R. (2009). "Predicting shear type crack initiation and growth in concrete with non-linear finite element method." PhD Thesis, Royal Institute of Technology, Stockholm, Sweden.
- Mast, R. F. (1968). "AUXILIARY REINFORCEMENT IN CONCRETE CONNECTIONS." *Journal of the Structural Division*, 94(ST 6), 1485–1504.
- Mattock, A. H., and Hawkins, N. M. (1972). "Shear Transfer in Reinforced Concrete - Recent Research." *Journal of the Prestressed Concrete Institute*, 17(2), 55–75.
- Meley, J. L., and Krauthammer, Theodor. (2003). *Finite element code validation using precision impact test data on reinforced concrete beams*. Final Report, The Pennsylvania State University, Protective Technology Center, 120.
- Millard, S. G., Molyneaux, T. C. K., Barnett, S. J., and Gao, X. (2010). "Dynamic enhancement of blast-resistant ultra high performance fibre-reinforced concrete under flexural and shear loading." *International Journal of Impact Engineering*, 37(4), 405–413.

- Murtha, R. N., and Holland, T. J. (1982). *Analysis of WES FY82 Dynamic Shear Test Structures*. Technical Memorandum, Naval Civil Engineering Laboratory.
- Park, J. J., Kang, S. T., Koh, K. T., and Kim, S. W. (2008). "Influence on the Ingredients of the Compressive Strength of UHPC as a Fundamental Study to Optimize the Mixing Proportion." Kassel University Press, Kassel, Germany, 105–112.
- Park, R., and Paulay, T. (1975). *Reinforced Concrete Structures*. Wiley-Interscience.
- Richard, P., and Cheyrezy, M. (1995). "Composition of reactive powder concretes." *Cement and Concrete Research*, 25(7), 1501–1511.
- Rong, Z., Sun, W., and Zhang, Y. (2010). "Dynamic compression behavior of ultra-high performance cement based composites." *International Journal of Impact Engineering*, 37(5), 515–520.
- Rossi, P., Arca, A., Parant, E., and Fakhri, P. (2005). "Bending and compressive behaviours of a new cement composite." *Cement and Concrete Research*, 35(1), 27–33.
- Roth, M. J., Boone, N. R., Kinnebrew, P. G., Davis, J. L., and Rushing, T. S. (2008). *Development of New Protective Solutions to Counter Emerging and Adaptive Threats*.
- Sayed, S. S. (2004). "Behavioral Study of Ultra High Performance Concrete Girders." MS Thesis, .
- Shah, S. P., and Weiss, W. J. (1998). "Ultra High Performance Concrete: A Look into the Future." *ACI Special Proceedings*, Houston, Texas.
- Simulia. (2011). *Abaqus Version 6.11 Documentation*. Dassault Systemes Simulia Corp.
- Slawson, T. R. (1984). *Dynamic Shear Failure of Shallow-Buried Flat-Roofed Reinforced Concrete Structures Subjected to Blast Loading*. Technical Report, USAE Waterways Experiment Station, Vicksburg, MS.
- Valle, M., and Buyukozturk, O. (1993). "Behavior of Fiber Reinforced High-Strength Concrete Under Direct Shear." *ACI Materials Journal*, 90(2), 122–133.
- Vecchio, F., and Collins, M. P. (1981). "Stress-strain characteristic of reinforced concrete in pure shear." *International Association of Bridge and Structural Engineering*, 34, 211–225.
- Walraven, J. C., and Reinhardt, H. W. (1981). "Theory and Experiments on the Mechanical Behaviour of Cracks in Plain and Reinforced Concrete Subjected to Shear Loading." *Heron*, 26(1A), 68.

- Wight, J. K., and MacGregor, J. G. (2008). *Reinforced Concrete: Mechanics and Design*. Prentice Hall.
- Williams, E. M., Reed, P. A., Graham, S. S., and Rushing, T. S. (2009). *Laboratory Characterization of Cor-Tuf Concrete With and Without Steel Fibers*. U. S. Army Engineer Waterways Experiment Station, Vicksburg, MS, 83.
- Wu, C., Oehlers, D. J., Rebentrost, M., Leach, J., and Whittaker, A. S. (2009). "Blast testing of ultra-high performance fibre and FRP-retrofitted concrete slabs." *Engineering Structures*, 31(9), 2060–2069.

## BIOGRAPHICAL SKETCH

David Michael Lavenhagen was born in Berwyn, Illinois in 1979. He attended primary and secondary school in Illinois. He worked in the construction industry from 1997, when he graduated high school, until 2005 when he began college.

He began his undergraduate studies at Palm Beach Community College, located in Boca Raton, FL, in August 2005, where he received his Associate in Arts degree with honors and was selected as the commencement speaker.

David continued his undergraduate studies in January 2008 at the University of Florida, where he graduated cum laude with a civil engineering degree concentrating in structural engineering, in December 2010. In January 2011, he continued at the University of Florida to pursue a master's degree in civil engineering concentrating in structural engineering and protective structure design. David graduated with his master of engineering degree in August 2012.

David was awarded a SMART Scholarship through the Department of Defense (DoD) to pursue a PhD in civil engineering at the University of Florida starting in August 2012.